Aus dem

Helmholtz Diabetes Zentrum, München

Investigating the role of adipocyte expressed A disintegrin and metalloprotease 17 (ADAM17) in energy expenditure and metabolic health

Dissertation

zum Erwerb des Doktorgrades der Humanbiologie

an der Medizinischen Fakultät der

Ludwig-Maximilians-Universität München

vorgelegt von

Rhoda Anane Karikari

aus

Kumasi-Ghana

Jahr

2025

Mit Genehmigung der Medizinischen Fakultät der

Ludwig-Maximilians-Universität München

Erstes Gutachten:	Prof. Dr. med. Susanna Hofmann
Zweites Gutachten:	Prof. Dr. Basil Hubbard
Drittes Gutachten:	Prof. Dr. Stefan Brunner
Mitbetreuung durch promovierte Mitarbeiterin:	Dr. Anastasia Georgiadi
Dekan:	Prof. Dr. med. Thomas Gudermann
Tag der mündlichen Prüfung:	12.03.2025

Table of content

Zusammenfassung (Deutsch):

Hintergrund: ADAM17(a disintegrin und metalloprotease 17), auch bekannt als Tumor-Nekrose-Faktor-alpha konvertierendes Enzym (TACE), spielt eine entscheidende Rolle bei der Verarbeitung und Freisetzung verschiedener Zelloberflächenproteine, darunter Zytokine, Wachstumsfaktoren und Rezeptoren. Diese Aktivität hat tiefgreifende Auswirkungen von ADAM17 auf entzündungsbedingte Stoffwechselkomplikationen wie Leber- und Nierenfibrose und Gefäßentzündungen gezeigt. Die Rolle von ADAM17 im Energiehaushalt ist nicht klar. ADAM17 wird in Adipozyten, dem primären Zelltyp, der für die Fettspeicherung zuständig ist, exprimiert, aber bis heute gibt es keine umfassende Studie, die die Rolle von ADAM17 im Adipozyten-Stoffwechsel, seine molekularen Ziele und die systemischen metabolischen Auswirkungen untersucht.

Methoden: Wir generierten Mäuse mit adipozytenspezifischer ADAM17-Defizienz unter der Kontrolle des Adi-PonectinCre-Promotors (AdipCre+Adam17KO) auf einem reinen C57BL6J-Genshintergrund und verwendeten Wildtyp-Mäuse (AdipCre-WT) als Kontrollen.. Mithilfe von transkriptomischen Bulk-RNA- und ungezielten proteomischen Analysen untersuchten wir die molekularen Auswirkungen der ADAM17-Defizienz auf weiße und braune Fettzellen sowie auf braunes und weißes Fettgewebe. Darüber hinaus führten wir eine tiefgreifende Phänotypisierung des Mausmodells AdipCre+Adam17KO durch, indem wir Studien zur Kälteexposition und Kälteimitation, Studien zu fettreicher Ernährung (HFD), Fastenstudien, Phänotypisierung im Stoffwechselkäfig, Studien zu fettreicher Ernährung und die Untersuchung von Stoffwechselparametern wie Energieverbrauch, Nahrungsaufnahme, Aktivität, Glukose- und Insulintoleranztests durchführten.

Ergebnisse: Unsere Untersuchungen haben ergeben, dass der adrenerge Beta-3-Rezeptor (Adrb3) ein potenzieller neuer Interaktionspunkt von ADAM17 in braunen und weißen Fettzellen ist. Wir fanden heraus, dass die Eliminierung von ADAM17 in Adipozyten zu einer Anhäufung von Adrb3-Proteinen in den braunen und weißen Adipozyten führt. Trotz der höheren Mengen an Adrb3-Protein fanden wir keine Unterschiede in der basalen und stimulierten Lipolyse zwischen AdipCre+Adam17KO- und WT-Adipozyten und keinen Unterschied in den Thermogenese-Zielgenen von Adrb3, wie beispielsweise uncoupling protein 1 (UCP1). Allerdings zeigten AdipCre+Adam17KO-Fettzellen sowie braunes und weißes Fettgewebe niedrigere Werte der mitochondrialen Elektronentransferkette (ETC), insbesondere Komplex I und ATPsynthase, und eine erhöhte Expression von Genmarkern des Glykolyse-Wegs. Mäuse mit einer konditionalen Eliminierung von ADAM17 in den Adipozyten (AdipCre+Adam17KO) wiesen im Vergleich zur AdipCre-WT-Kontrolle eine verminderte Kälteadaptation auf, obwohl sich die kälteinduzierten UCP1-Spiegel nicht unterschieden. AdipCre+Adam17KO zeigten hohe creatine kinase, M-type (CKM)-Proteinspiegel und mitochondrial creatine kinase 2 (CKMT2) in BAT, wasauf den Einsatz von Ucp1-unabhängigen substrate Zyklen hindeutet. Außerdem nahmen AdipCre+Adam17KO- im Vergleich zu AdipCre-WT-Kontrollmäusen bei HFD mehr Gewicht zu. High-fat diet (HFD) und Katecholamin-Injektionen beeinflussten beide den zirkulierenden Cholesterinspiegel. Schließlich stellten wir fest, dass AdipCre+Adam17KO Mäuse bei der Fütterung mehr Leberglykogen speicherten als AdipCre-WT-Kontrollmäuse und eine hohe Glykogenverwertung während des 16-stündigen Fastens aufrechterhielten, wobei sie im Vergleich zu AdipCre-WT-Kontrollmäusen immer noch 2-fach höhere Leberglykogenwerte aufwiesen.

Schlussfolgerungen: Die Eliminierung von ADAM17 in Adipozyten beeinträchtigte die Energiehomöostase des gesamten Körpers bei Kälteexposition und HFD und führte zu einer höheren Glykogenanreicherung in der Leber nach der Fütterung. Dieses phänotypische Merkmal ist mit einer erhöhten Expression von UCP1-unabhängigen vergeblichen Zyklen in BAT und iWAT und

erhöhten Proteinkonzentrationen von Adrb3 auf zellulärer Ebene verbunden. Weiterführende Studien müssen sich mit den direkten zellulären Interaktionspunkt von ADAM17 befassen, die die zelluläre Energetik beeinflussen können.

Abstract (English):

Background: ADAM17 (a disintegrin and metalloprotease 17), also known as tumor necrosis factor-alpha converting enzyme (TACE), plays a crucial role in the processing and shedding of various cell surface proteins, including cytokines, growth factors, and receptors. This activity has demonstrated profound implications of ADAM17 inflammation related metabolic complications, such as liver, kidney fibrosis and vascular inflammation. The role of ADAM17 in energy balance is not clear. ADAM17 is expressed in adipocytes, the primary cell type governing fat storage, but up to this date, there is no comprehensive study examining the role of ADAM17 in adipocyte metabolism, its molecular targets, and systemic metabolic effects.

Methods: We generated mice with adipocyte-specific ADAM17 deficiency, under the control of AdiponectinCre promoter ($Adip^{Cre+}$Adam17KO) and employed wild-type mice ($Adip^{Cre-}$WT) as controls, on a clean C57BL6J genetic background. Utilizing bulk RNA transcriptomic and untargeted proteomic analyses, we explored the molecular consequences of ADAM17 deficiency on white and brown adipocytes and adipose tissues. Additionally, we conducted deep phenotyping of the mouse model, $Adip^{Cre+}$Adam17KO, by performing cold exposure and cold mimicking studies, high-fat diet (HFD) studies, fasting studies, metabolic cage phenotyping, and examining metabolic parameters such as, energy expenditure, food intake, activity, glucose, and insulin tolerance tests.

Results: Our investigation unveiled the beta 3 adrenergic receptor (Adrb3) as a potential novel target of ADAM17 in brown and white adipocytes. We found that ADAM17 deletion in adipocytes, specifically led to the accumulation of Adrb3 protein levels in the brown and white adipocytes**.** Despite the higher levels of Adrb3 protein, we found no differences in basal and stimulated lipolysis between $Adip^{Cre+}$Adam17KO and WT adipocytes and no difference in thermogenesis target genes of Adrb3, such as UCP1. However, $Adip^{Cre+}$Adam17KO adipocytes as well as brown and white adipose tissues showed lower levels of mitochondrial electron transfer chain (ETC) specifically complex I and ATP-synthase and increased expression of gene markers of the glycolysis pathway. Mice with adipocyte conditional deletion of ADAM17 ($Adip^{Cre+}$Adam17KO) showed impaired adaptation of cold temperature compared to $Adip^{Cre-}$WT control mice, despite no difference in cold induced levels of uncoupling protein 1 (UCP1). $Adip^{Cre+}$Adam17KO mice showed high protein levels of creatine kinase, M-type (CKM) and mitochondrial creatine kinase 2 (CKMT2) in BAT suggested the employment of UCP1 independent futile cycles. Moreover, $Adip^{Cre+}$Adam17KO mice gained more weight upon HFD compared to $Adip^{Cre-}$WT control mice. High-fat diet (HFD), catecholamine injections both affected circulating cholesterol levels. Finally, we found that upon feeding $Adip^{Cre+}$Adam17KO mice stored more liver glycogen compared to $Adip^{Cre-}$WT control mice and maintained high glycogen utilisation throughout 16hour fasting, when they still had 2-fold higher liver glycogen levels compared to $Adip^{Cre-}$WT control mice.

Conclusions: Deletion of ADAM17 in adipocytes affected whole body energy homeostasis upon cold exposure and HFD feeding, as well as higher liver glycogen accumulation upon feeding. This phenotypic characteristic associated with increased expression of UCP1 independent futile cycles

in BAT and iWAT and increased protein levels of Adrb3 at the cellular levels. More focused studies need to address the direct cellular targets of ADAM17, which may affect cellular energetics.

List of figures

List of tables

List of abbreviations

ACE 2	Angiotensin- converting enzyme 2
ADAM	A Disintegrin And Metalloproteinases
ADAMTS	A Disintegrin And Metalloproteinase with Thrombospondin repeats
Adrb3	Beta 3 Adrenergic Receptor
AT	Adipose Tissue
B1AR	Beta-1 Adrenergic Receptor
BAT	Brown Adipose Tissue
BCA	Bicinichoninic acid
BSA	bovine serum albumin
cAMP	Cyclic Adenosine Monophosphate
CD	Cysteine Domain
cDNA	Complementary Deoxyribonucleic acid
DD	Disintegrin Domain
DMEM	Dulbecco's Modified Eagle Medium
DPBS	Dulbecco’s Phosphate Buffered Saline
ECM	Extracellular Matrix
EDTA	Ethylenediaminetetraacetic acid
EGF	Epidermal Growth Factor-like domain
ELISA	Enzyme-linked immunoassay
ER	Endoplasmic Recticulum
FBS	Fetal Bovine Serum
FFAs	Free fatty acids
GLP-1	Glucagon-like peptide-1
GPCR	G protein- coupled receptor
gWAT	gonadal white Adipose tissue
HFD	High Fat Diet
hMADS	Human Multipotent Adipose-Derived Stem
HSL	Hormone Sensitive Lipase
IBMX	3-isobutyl-1-methylxanthine
IL-1β	Interleukin 1 beta
IPGTT	Intraperitoneal glucose tolerance test
ITT	Insulin tolerance test
iWAT	Inguinal White Adipose Tissue
KO	Knockout
LDLR	Low Density Lipoprotein Receptor
LPS	Lipopolysaccharide
MgCl	Magnesium Chloride
miRNA	Micro Ribonucleic acid
MMP	Matrix Metalloproteinases
MPD	Metalloprotease Domain
mRNA	Messenger Ribonucleic acid
NaCL	Sodium Chloride
NAFLD	Non-Alcoholic Fatty Liver diseases
NEFAs	Non-Esterified Fatty acids

NST	Non-Shivering Thermogenesis
PACSIN3	Protein Kinase C And Casein Kinase Substrate In Neurons 3
pATF-1	Phosphorylated activating transcription factor-1
pCreb	Phosphorylated cAMP responsive element bindingprotein
PD	Pro-Domain
PDI	Disulphide Isomerase
pHSL	Phosphorylated Hormone-sensitive lipase
PKC	Protein Kinase C
P-S	Penicillin-Streptomycin
PVDF	Polyvinylidene fluoride
qPCR	Quantitative Polymerase Chain Reaction
RBC	Red Blood Cell
RIPA	Radioimmunoprecipitation assay buffer
RT	Room Temperature
scRNA-seq	small conditional RNA Sequence
SIRT1	Silent Information Regulator Sirtuin 1 protein
SNS	Sympathetic Nervous System
SP	Sequences Peptide
SVF	Stromal Vascular Fraction
T2D	Type 2 Diabetes
TE Buffer	Tris-Ethylenediaminetetraacetic acid buffer
TH	Tyrosine Hydroxylase
TIMPs	Tissue Inhibitors of Metalloproteases
TLR4	Toll-like Receptor 4
TMB	3,3',5,5'-Tetramethylbenzidine
TMD	Transmembrane Domain
TNF-alpha	Tumour Necrosis Factor alpha
UCP1	Uncoupling Protein-1
VLDLR	Very Low-Density Lipoprotein Receptor
WAT	White adipose tissue
WT	Wildtype
β3AR	Beta-3 Adrenergic Receptor

1. Introduction

Adipose tissue is a central organ in the regulation of energy homeostasis and metabolic health. The ability of adipose tissue to remodel in size and to adapt its metabolism to the availability of lipids and sugars determines not only the health status of the adipose tissue itself, but also of other organs such as the liver and the muscle.

This thesis investigates the role of the metalloprotease ADAM17 in reshaping the energetic profile and plasticity of the adipose tissue. This introduction provides an overview on basic concepts of energetic flexibility of adipocytes and of our current knowledge on how metalloproteases and specifically ADAM17 can alter adipose tissue plasticity, utilization of energy substrates in the adipocytes and affect whole body energy expenditure.

1.1 Basic concepts on the role of different types of adipocytes on the control of energy balance

For a long time, the adipose tissue was only considered as a homogeneous, energy storage organ, composed mainly of adipocyte cells, which can adapt their size depending on the energy excess or its scarcity. Almost 20 years ago the existence of a highly energy consuming type of adipose tissue, the brown adipose tissue (BAT), came into light creating a paradigm shift in the belief that adipose tissue was only there to store fat (Heaton, 1972). The main role of BAT is to produce heat and maintain core body temperature (Hull & Segall, 1965). Today, data collected via single cell analysis of white adipose tissue have revealed a much higher complexity of adipose tissue, with many potentially functional subclusters of adipocytes and others´ cell types (Liu *et al*., 2023). Here we will outline the main differences of white, brown and beige adipocytes.

The white adipose tissue (WAT) is covering the biggest part of the fat depots in the body (in mouse and human) and in general, it can be divided into two major anatomical regions, the subcutaneous and visceral fat. Subcutaneous fat is located under the skin, whereas the visceral fat within the central body cavity. *Types of WAT depending of their location in humans are*: Visceral adipose tissue (AT): epicardial and pericardial, mesenteric, omental, gonadal. Subcutaneous, abdominal: gluteal, femoral and abdominal (under the skin)(Audano *et al*., 2022).

In mice main and most studied WAT depots are: Visceral AT: perigonadal, mesenteric fat, omental and pericardial (only evident in high fat diet mice) and Subcutaneous AT: inguinal AT. Inguinal AT (iWAT) in mice and abdominal AT (abAT) in humans are considered rather similar (Chusyd *et al*., 2016) and are the major storage location for energy after meals. Thus, on high caloric diets first the iWAT, abAT expands and when the storage capacity of these fat depots is exceeded, excess energy storage is directed towards visceral depots (Schirinzi *et al*., 2023).

Brown adipose tissue (BAT) localization is distinct to that of the WAT. In humans BAT is divided in cervical, supraclavicular, mediastinal, paravertebral, perirenal (Jalloul *et al*., 2023). In mice, the biggest BAT depots are at the intrascapular region and smaller BAT is found in the cervical, supraclavicular, axillary, periaortic, paravertebral and perirenal regions (Smith *et al*., 2013)

The function of most WAT and BAT depots and their relative differences are up to date mostly unclear and understudied. More in depth information on the classification of different fat depots can be found in the recent reviews (Börgeson *et al*., 2022),(Chun, 2021).

Brown, beige and white adipocytes: Most studied differences on the energetic profile on WAT and BAT have been based on the comparison of the macroscopic features, function and origin of white and brown adipocytes (summarize in Table 1). While white adipocytes are cells filled with a single big, unilocular fat droplet, brown adipocytes have multiple compartmentalized lipid droplets. Brown adipocytes are filled with mitochondria, whereas white adipocytes have few of them. Brown adipocytes are taking up and consuming lipids and carbohydrates in much higher levels compared to white adipocytes, and they dissipate ATP to heat (Townsend & Tseng, 2014). Thus, brown adipocytes are dedicated to thermogenesis, whereas white adipocytes are dedicated to energy storage for energy source (fatty acids) in periods of energy scarcity (eg. starvation) (Avram *et al*., 2005). Brown adipocytes derive from Myf5+ progenitors, thus they stem from muscle tissue progenitor cells rather than white adipose tissue progenitors (Ziqubu *et al*., 2023).

The era of single cells has presented a new picture of high complexity in both brown and white adipose tissues and multiple types of adipocytes, most of them yet need to be further functionally characterized. In accordance with these observations, with the WAT depots, upon certain hormonal and environmental challenges, brown like adipocytes make their appearance (Carobbio *et al*., 2019). Those cells have been called beige adipocytes. Beige adipocytes emerge either from de novo differentiation of progenitor's cells or trans differentiation of white

adipocytes to beige adipocytes (Wang & Scherer, 2014). Beige adipocytes have brown like characteristics; however, the purpose of their emergence is not clear. Nevertheless, due to their high-energy consuming properties, both brown and beige adipocytes have gained great interest for the development of new anti-obesity and anti-diabetic strategies.

Table 1: Differences between the different types of adipose tissue

	BAT	**WAT**	**BEIGE**
Anatomical location	Interscapular fat pad, cervical, supraclavicular(adults), paravertebral, perirenal (neonate)	(Heterogenous) Subcutaneous, gonadal, omental, epicardial	Recruited from subcutaneous (anterior and inguinal)
Lineage Embryonic origin	Derived from mfy5+ precursors.	Derived from myf5- precursor.	Derived from myf5- cited1+ cd137+ precursor.
Adult origin	BAT precursor, muscle satellite cells and endothelial precursor.	White adipocyte precursor, endothelial precursor	White adipocyte precursor, mature white adipocytes
Histological appearances	1.multilocular 2.complex and many mitochondria 3. Centrally placed single lipid droplet	1.Unilocular 2.Low mitochondria number 3.Multiple small lipid droplets	1.multilocular 2.Abundant mitochondria after stimulation. 3.Small lipid droplets
Endocrine role (Primary functions)	Energy expenditure (Thermogenesis)	Energy storage	Energy expenditure (Adaptive Thermogenesis)
UCP1	positive	negative	positive
Endocrine role (secretome)	Release and secrete Batokines (e.g., Fgf21)	Release and secrete Adipokines (e.g., Leptin)	Release and secrete Batokines (fgf21)

1.2 Energy consuming futile cycles in brown and beige adipocytes

Mammals have two different ways to protect their body temperature. One is shive-Fring thermogenesis (ST) and the other non-shivering thermogenesis (NST). During ST, muscle fibers contract and produce repetitively ATP. As part of this process some energy is dissipated in the form of heat (Rosenwald & Wolfrum, 2014). During NST, classically known to be taking place in the BAT and beige adipocytes, in response to low environmental temperature occurs a mitochondrial short-circuit which uncouples the proton gradient generated by the mitochondrial respiratory chain from ATP production, leading to the continuous consumption of substate to the release of heat (Schirinzi *et al*., 2023). Consumption of substrate to produce heat has been described with the term '**energy dissipation', it occurs in an ATP uncoupled, and ATP coupled mechanisms**. Below we described these two many molecular processes of energy dissipation in brown and beige adipocytes.

Oxidative phosphorylation: The oxidative phosphorylation utilizes oxygen to generate high-energy phosphate bonds in the form of adenosine triphosphate (ATP). It takes place in the mitochondrion and involves the transfer of electrons from NADH and FADH2 to oxygen across several protein, metal and lipid complexes, known as the electron transfer chain (ETC). At the molecular level, the ETC is composed of five protein complexes, Complex I, II, III, IV, and Complex V (ATP synthase). Complex I-IV facilitate the transfer of electrons from one to another and during this transfer, they pump protons (H+) into the mitochondrial intermembrane space. The difference in concentration of H^+ ion between the intermembrane space and mitochondrial matrix is known as the '**proton motive force'**. ATP synthase (Complex V) is using the proton motive force to convert ADP plus active phosphate (Pi) to ATP (Brownstein *et al*., 2022; Chouchani *et al*., 2019).

UCP11 mediated uncoupling: Uncoupling protein 1 (UCP11) (Slc25a7) is a protein highly expressed in brown and beige adipocytes. It stands between the ETC and ATP synthase and upon sympathetic, adrenergic activation mainly in response to cold and more under debate postprandially, it releases protons present in the intermediate space disrupting their usage for ATP production. This process generates heat (Brownstein *et al*., 2022; Chouchani *et al*., 2019; Ikeda & Yamada, 2020).

The mitochondrial ADP/ATP carrier, (AAC): AAC is a solute carrier family 25

(SLC25) protein. Those are mitochondrial transporters, which typically facilitate the flux of very large metabolites from the cytosol to the inner mitochondrial membrane (Palmieri, 2004). AAC exchanges cytosolic and mitochondrial adenine nucleotides across the inner mitochondrial membrane (IMM), to provide ADP for ATP synthesis and to deliver ATP to the cytosol (Klingenberg, 2008). AAC was found to promote proton leak through the ETC, after activation by fatty acids (Bertholet *et al*., 2019). AAC, like UCP1 is causing uncoupling of the protein motive force from ATP synthesis. This process generates heat.

Calcium futile cycle: Upon cold exposure, Norepinephrine activates beta-adrenergic signaling which triggers increase in intracellular calcium by activating ryanodine receptor 2 (RyR2) and promoting extrusion of ER localized calcium to the cytosol. Cytosolic calcium binds and increases the activity of the sarco (endo) plasmic reticulum Ca2 (SERC2b), which consumes ATP to bring the calcium back to the ER. This futile cycle was found in beige adipocytes, but it was shown to be dispensable in brown adipocytes where UCP1 activity is high (Mottillo *et al*., 2018).

Creatine - phosphocreatine futile cycle: The creatine, phosphocreatine futile cycle preserves ATP in situation of ADP scarcity. It has been shown to promote ATP dependent thermogenesis in beige adipocytes and brown adipocytes lacking UCP1 (Kazak *et al*., 2015).

Lipolysis and re-esterification futile cycle: In both brown and beige adipocytes, lipid catabolism and triglyceride synthesis have been observed to be happening in a cycling manner. The catabolism of lipids involves the actions of adipose triglyceride lipase (ATGL), hormone sensitive lipase (HSL) and monoglycerol lipase (MGL). Those enzymes hydrolyze the triglycerides stored in lipid droplet and release free glycerol. Free glycerol can be re-esterified back into triglycerides, via an anabolic reaction mediated by glycerol kinase, consuming ATP (Reshef *et al*., 2003). When glycerol kinase is not present in the cells or not expressed at high levels, then the generation of triglycerides can be done de novo by glucose conversion into glycerol, via glyceroneogenesis mediated by the action of phosphoenolpyruvate carboxykinase (PEPCK-C) (Reshef *et al*., 2003). Lipid cycling in the adipose tissue can occur in coordination with lipid cycling in the liver and this liver-adipose tissue axis is important in liver disease and systemic glucose homeostasis (Prentki & Madiraju, 2008), (Larter *et al*., 2010). In humans and in cultured adipocyte a substantial amount of fatty acids are found to be recycled (Wolfe *et al*., 1990),(Hammond & Johnston, 1987).

1.3 Beta adrenergic receptors canonical thermogenic signals and non-canonical signaling in adipocytes.

Cold, prolonged fasting and exercise increase the adrenergic tone and lead to the release of norepinephrine from nerve endings within the adipose tissue (Peres Valgas da Silva *et al*., 2019). Beta adrenergic receptors (Adrbs) are mediating the lipolytic effects on norepinephrine in brown and white adipose tissue (Carpentier *et al*., 2023; Evans *et al*., 2019). There are 3 beta adrenergic receptors, Adrb1, Adrb2 and Adrb3. In mice most abundant beta-adrenergic receptor the brown and white adipose tissue is Adrb3, whereas humans have higher levels of Adbr2 as well as Adrb3 in brown and white fat (Blondin *et al*., 2020; Straat *et al*., 2023).

Norepinephrine is known to interact with all three beta adrenergic receptors and this influences triglyceride hydrolysis, mitochondria oxidation and cAMP activation, leading to BAT thermogenesis (Peirce *et al*., 2014) . Physiologically, in adipocytes (brown and white), Adrb3 is coupled to Gs and adenylyl cyclase III, which leads to the generation of cAMP that phosphorylates the hormone sensitive lipoprotein lipase (HSL) resulting in the lipolysis of triglycerides (Li *et al*., 2022). Ligand activation leads to rapid beta arrestin desensitization and clathrin mediated internalization of Adrb1 and Adrb2, however this mechanism does not apply for Adrb3, which remains longer active after ligand activation compared to other two Adrbs (Nantel *et al*., 1993). For that reason, Adrb3 is a target of anti-obesity research.

Chronic exposure to catecholamines, which occur for example during obesity development results in the decrease of mRNA and protein of Adrb3 and reduced lipolytic response in adipocytes (Mowers *et al*., 2013). Transgenic mouse models of Abrb3 deletion showed compensatory increase of Adrb1 and no phenotype in male mice, whereas Adrb3KO female mice showed increased fat storage (Susulic *et al*., 1995). Beta1, 2 and 3 triple knockout mice are prone to obesity (Jimenez *et al*., 2002), with decreased thermogenesis. Also, studies done in beta 1, and beta 3 receptors mice have shown their involvement in the regulation of lipolysis and thermogenesis though beta 2 receptor knockout mice are not susceptible to diet induced obesity (Diering *et al*., 2017).

Pharmacological activation of Adrb3 has been explored using the specific agonist Cl316243 in mice and commercial drug Mirabegron in humans. Mouse studies with Cl316,243 injections have shown increased lipolysis, weight loss, increased energy expenditure and increased expression of thermogenic markers, including Ucp1 in the white adipose tissues (Cero *et al*., 2021). In non-obese humans Mirabegron in high doses (more than 50mg) acutely increased energy expenditure, but it also increased systolic blood pressure, which is a counter indication for its long-term usage in humans (Cero *et al*., 2021). In obese humans Cl316, 243 showed poor bioavailability no effects on insulin sensitivity and a small loss of weight (Schena & Caplan, 2019). In other human studies, BRL 26830 (B3 agonist) showed an overall improvement in insulin and glucose tolerance and a reduction in weight but not a reduction in fasting blood glucose level. It is worth mentioning that B3 agonist reduce leptin levels at the transcriptional level and when leptin is increased, B3AR activity is reduced and vice versa (Cero *et al*., 2021).

The canonical signaling pathway of Adrb3 ligand activation leads to coupling with the Gas protein, increase in cAMP levels and PKA signaling, along with increase of lipolysis via pHSL activation. Released fatty acids activate UCP11 in mitochondria and increase thermogenesis (Fedorenko *et al*., 2012). In adipocytes, coupling of Adrb3 to Gi and subsequent initiation of MAP kinase cascade results in the release of FFAs obtained from triglycerides hydrolysis (Cero *et al*., 2021). The signaling pathways specifically linked with Adrb3 activation and maintenance of futile cycles are not clear.

Activation of Adrb3 has been linked with inflammation via the established activation that Adrb3 agonists have on IL-6. This seems to follow a non-canonical signaling of Adrb3, which involves the activation of p38 and PKC-dependent signaling in white adipocytes (Tchivileva *et al*., 2009). Related to this aspect of Adrb3 signaling, convectional and novel PKCs have been reported to be stimulated by Adrb3 agonists (Tchivileva *et al*., 2009). Overall Adrb3 signaling is diverse and the molecular players modulating the differential signaling response and functional outcomes of Adrb3 agonists are not really understood.

1.4 A disintegrin and metalloproteinase's (ADAM) role on adipose tissue remodeling and metabolism in the context of thermogenesis and EE.

Zinc dependent endopeptidases, matrix metalloproteinases (MMPs), A Disintegrins and Metalloproteinases (ADAM) play a critical role in degradation of extracellular matrix (ECM) proteins, such as collagen, laminin, and the shedding of various membrane receptors (Lu *et al*., 2011).

ADAM proteins differ from MMPs in several key points, which are the substrate specificity, biological function, and cellular localization. While MMPs are mostly degrading components of the ECM, ADAM proteins are cleaving and shedding cell membrane-bound proteins, including growth factors, cytokines, adhesion molecules and receptors (Seals & Courtneidge, 2003). The biological function of ADAM proteins is then related to the function of their target proteins, whereas MMPs have more general roles in ECM turnover and tissue remodeling. ADAM proteins are multidomain proteins that typically consist of metalloproteinase domain, a disintegrin domain, a cysteine-rich, an epidermal growth factor (EGF)-like domain, a transmembrane domain, and cytoplasmic tail. MMPs typically include a signal peptide, a pro-peptide, a catalytic domain, a hinge region, and a hemopexin- like domain. ADAM proteins typically are cell membrane bound, but some ADAM protein can be shed into the ECM. MMPs are either shed to the ECM or bound to the cell membrane (Black *et al*., 1997; Reddy *et al*., 2000)

Here we will focus on the known function of different ADAM proteins on adipose tissue and specifically on the adipocyte. There is a list of 21 ADAM protein numbered from ADAM1 to ADAM33. From publicly available data, (Emont *et al*., 2022) we were able to find that ADAM10, ADAM12, ADAM17 are well expressed in human white adipocytes , and, ADAM9, ADAM10, ADAM12, ADAM17 in mouse adipocytes. ADAM9 and ADAM12 are more specifically and highly expressed in adipocytes as opposed to adipose stem and progenitor cells (ASPCs), vascular, and immune cells in both mouse and human. Adam10 and ADAM17 are expressed in adipocytes, but to a lower degree compared to adipose monocytes and endothelial cells.

Concerning their role in adipose tissue remodeling and energetics, the following is known:

ADAM12 protein is found to impact proliferation of preadipocytes, delayed differentiation of preadipocytes to adipocytes and increased lipid accumulation in mature adipocytes (Coles *et al*., 2018). There are two splice variants of Adam12

mRNA, Adam12-L (long transmembrane form) and Adam12-S (short soluble, secreted form) (Kawaguchi *et al*., 2002). Overexpression of Adam12-S and Adam12-L in mice was found to increase fat storage within the skeletal muscle (Kawaguchi *et al*., 2002), however mice overexpressing only Adam12-L did not show that phenotype. Thus, the soluble Adam12-S is responsible for increased adipogenesis and studies on Adam12-S mice lacking the pro- and metalloprotease domain of Adam12-S showed that the catalytic domain is crucial for the pro adipogenesis effects of Adam12-S(Kawaguchi *et al*., 2002). In addition, Kawaguchi *et al*. found that PPAR gamma, a master regulator of adipogenesis was upregulated in adipocytes found within connective of skeletal muscle in close proximity to blood vessels, in mice overexpressing Adam12 (Kawaguchi *et al*., 2002). Therefore, it is possible that Adam12 is involved in the development of adipocytes that originate from mesenchymal progenitor or preadipocytes within the perivascular space of connective tissue. Deletion of Adam12 in mice decrease BAT mass (Kurisaki *et al*., 2003). Furthermore, Adam12 knockout (KO) mice were resistant to diet induced obesity, because the proliferation of pre-adipogenic progenitor cells was low and adipogenesis was decreased (Masaki *et al*., 2005). IGFBP-3 was found to be involved in this phenotype. IGFBP-3 is cleaved by Adam12 to give rise to IGF-I, which activates IGF-I receptor to induce proliferation of pro-adipogenic progenitor cells (Masaki *et al*., 2005),(Shi *et al*., 2000).

ADAM9 protein is highly expressed in adipocytes (Josson *et al*., 2011), but up to date there is no established connection between Adam9 and adipose tissue function.

ADAM17 can indirectly affect adipocytes adipogenesis via its substrate Pref-1 (Hudak & Sul, 2013). Mice with partial deletion of ADAM17 showed improved glucose tolerance and obesity induced type 2 diabetes (T2D) compared to wildtype mice. This was due to improved plasticity of the adipose tissue and improves inflammatory profile (Kaneko *et al*., 2011). Whole body deletion of ADAM17 has been previously shown not give viable mice, however Gelling and friends generated outbred lines with ADAM17 whole body deletion and acquired a small percentage of viable pups, which were hypermetabolic (Gelling *et al*., 2008). More specific studies of ADAM17 in human mesenchymal stem cell derived adipocytes (hMADS) showed suppression of ADAM17 via miRNA-26, which led to beige cells formation, marked by increased mitochondrial numbers and increased thermogenesis (Karbiener *et al*., 2014). During the time of this thesis, two studies were published on the phenotype of AdiponectinCre mediated dele-

tion of ADAM17. The study by Lownik and colleagues showed no impact of adipocyte deletion of ADAM17 on HFD (60% fat) induced obesity, prediabetes or inflammation (Lownik *et al*., 2020), whereas the study by Amin *et al*. using the same approach reported lower weight gain and increase brown fat temperature in AdiponectinCreADAM17KO mice fed a HFD (60% fat) for 26 weeks (Amin *et al*., 2023b). Of note, mixed genetic backgrounds (C57Bl6, Sv129, Ola/HSD) have been used in both studies (personal communication with the corresponding author) and no backcrossing information exist, that may be the underlying reasons for those contradictory phenotypes.

Adam10 protein´s role in adipose tissue, adipocytes or adipogenesis is not clear and not systematically studied. However, it shares high homology with ADAM17 and many substrates' targets (Table 2).

1.5 ADAM17 maturation pathway and regulation of activity

ADAM17 activation is preceded by the removal of the pro-domain, which involves the action of furin, a pro protein convertase which cleaves ADAM17 in the trans Golgi. The pro-domain acts as the potent inhibitor of the activity of the mature form of the enzyme (Perez *et al*., 1990). The pro-domain functions as a chaperone that prevents the degradation of enzymes as it passes through the secretory system (Prins, 2008).

In addition to the pro-domain removal, the co-ordination between all the other ADAM17 domains greatly influence it´s activation and functions. The membrane domain for example, regulates conformational changes of the enzymes, through interactions with protein Disulphide isomerase (PDI), which catalyses isomerization of 2 disulphide bonds leading to ADAM17 activation.

The shedding activity of ADAM17 can be rapidly stimulated by intracellular events, such as calcium flux, activation of extracellular signal-regulated kinase,(Horiuchi *et al*., 2007), protein kinase C (PKC),(Kveiborg *et al*., 2011),tyrosine kinases (Fan & Derynck, 1999) and GPCR receptors signaling (Prenzel *et al*., 1999).

iRhoms

Mammals have two types of iRhom´s, iRhom1 and iRhom2. IRhom´s are generally pseudo proteases lacking catalytic residues and they contain seven (7) transmembrane domains (TMD). In their active site, rhomboid GPx replaces the rhomboid catalytic motif GxS. In many studies, iRhom´s have been shown to be involved in induction of proteasomal degradation pathway, EGFR signaling pathway and inflammation control (Zettl *et al*., 2011).

The release of TNF-α in response to LPS stimulation is abrogated upon loss of iRhom2, due to the failure of ADAM17 to migrate from ER to Golgi where it is cleaved by pro-protein convertase furin. This prevents the trafficking of ADAM17 to the cell surface. iRhom2 deficient (iRhom-\-) mice, stimulated with TLR4 ligand for LPS, resulted in significantly less soluble secretion due to the blockage of the cleavage of membrane bound TNF alpha into its soluble form and this correlated positively with less Adam 17 maturation and trafficking two the cell surface. IRhom1 is also known to regulate the activity of Adam 17 similarly to iRhom2.

Soluble ADAM17

Most research has focused on the membrane anchored ADAM17. However, ADAM17 in found in a soluble form and its shedding is specifically mediated by Adam8 (Scharfenberg *et al*., 2020). Soluble ADAM17 has proteolytic activity and can act in an endocrine or paracrine manner.

Table 2: LIST OF KNOWN ADAM17 TARGETS

Cytokines	Growth factors	Receptors	Adhesion molecules	enzymes	Cellular transport	Others
CD44	Amphiregulin	ACE-2	ALCAM	NPR1	SCRB1	APP
CX3CL1	CSF-1	APOER	CD44	Carbonic	SORCS-1	CD163
FLT-3L	Epigen	CD30	CD62L	Hydrolase 9	SORCS-3	KIM-1
Jagged 1	Epiregulin	CD40	collagen XVII	ACE-2	SORL-1	MerTK
Kit-ligand 1 and 2	HB-EGF	CD89	desmoglein-2	Klotho	SORT-1	PMEL17
LAG-3	IGFR1	EMMPRIN	EpCAM		TREM-2	PrPc
MICA	Neuregulin-1	EPCR	ICAM-1		IGF-2R	Tim-3
MICB	Pref-1	Ephrin B4	JAM-A		LRP-1	VASN
RANKL	SEMA4D	ErbB4	L-selectin		LDL-R	Ebola virus Glycoprotein
TNF-α	TGF alpha	GHR	L1-CAM			
TNF beta	Tomoegulin-2	GPIba	PTP-LAR			
TRANCE		GPV	NCAM			
Lymphotoxin α		GPVI	nectin-4			
IL-8		IL-1R II	PECAM-1			
		IL6R	VCAM-1			
		Integrin beta-1				
		Leptin receptor				
		LOX-1				
		M6P/IGF2R				
		Notch1				
		NPR				
		p55 TNF alpha RI				
		P75 TNF receptor				
		p75NTR				
		Ptprz				
		syndecan 1 and 4				
		Toll-like receptor 4				
		TrkA				
		VEGFR				
		VPS10p				

1.6 Aim of the study

The aim of this doctoral project was to elucidate the role of ADAM17 in adipocyte metabolism. When this project was initiated, there were no mouse models of ADAM17 deletion in adipocytes, so we embarked to generate and phenotype the mouse model with adipocyte specific deletion of ADAM17 mouse model (Adip^{Cre+}Adam17KO). We aimed to understand the impact of ADAM17 in adipocyte metabolism and identify potential substate targets of ADAM17 in adipocytes that mediate its local functional effects. Finally, we fully phenotypically characterized the Adip^{Cre+}Adam17KO mouse model, under cold exposure conditions, fasting and high fat diet induced obesity.

2. Material and Methods

2.1 Ethical approval

The animal ethics committee of Helmholtz research center in Munich approved all experimental protocols for the animal study, and they were performed in accordance with the German Code of Practice for the Care and Use of Animals for Scientific Purposes.

2.2 Mice

2.2.1 Generation of Adipoq Cre ADAM17-floxed mice (Adip^{Cre+}Adam17KO)

To generate Adipoq Cre driven deletion of ADAM17 in the adipose tissue of mice, ADAM17-floxed mice (stock no. 009597) on a mixed genetic background C57BL/6J;129P2/Ola Hsd, were purchased from the Jackson Laboratory and this was backcrossed for 6 generations to a wild type C57BL/6J obtained from the Charles River Laboratories. The ADAM17-floxed mice (backcrossed 6 times, with clean background) were bred to Adipoq-Cre mice (stock no. 028020). Mice were genotyped according to protocol from the Jackson Laboratory (JAX) (stock no. 009597).

2.3 Stromal vascular fraction (SVF) isolation and differentiation to mature adipocytes.

For isolation of the stromal vascular fraction (SVF), wild type or ADAM17 AdKO mice were sacrificed by cervical dislocation and brown adipose tissue (BAT) as well as inguinal white adipose tissue (iWAT) were isolated. After Lymph nodes removal from iWAT, all tissues were washed with Dulbecco's Phosphate Buffered Saline (DPBS) to remove the blood and were kept on ice until further processing. The tissues were minced with curved scalpels, transferred to a 50 mL tube, and

resuspended with 5 mL of digestion buffer. After incubation at 37 °C for 7-10 minutes (mins) on a shaking device, the tissue digestion was stopped by adding 45 mL of ice chilled isolation buffer and passed through with a 100 µM cell strainer to remove debris and undigested tissue pieces. This is followed by centrifugation at 500 x g for 15 mins at 20 °C and the supernatant was discarded. After RBC lysis using 2 mL AKT lysis buffer for 5 mins at RT, the cell pellet was re-suspended in 50 mL of isolation buffer and again passed through a 70 µM strainer. Centrifugation was repeated and the final pellet was re-suspended in complete media and were plated onto a 10 cm petri dish and incubated at 37 °C, 5% CO2 to allow the cells to adhere to the plate. The next day, cells were washed with warm DPBS, and media was exchanged. Two days after plating, the media was changed again, and the confluency of the cells was assessed.

2.3.1 Differentiation of mouse primary Stromal Vascular Fraction (SVF)

When SVF preadipocytes were grown until confluence in DMEM high glucose, 10% FBS + 1% P/S, differentiation was initiated with the addition of induction media for 2 days. On day 3, media was changed to second media containing 0.865 ng/ml insulin for 2 days and on day 5, the media was changed in maintenance media containing 0.4325 ng/ml insulin. Experiments were performed between day 6 and day 8 post differentiation.

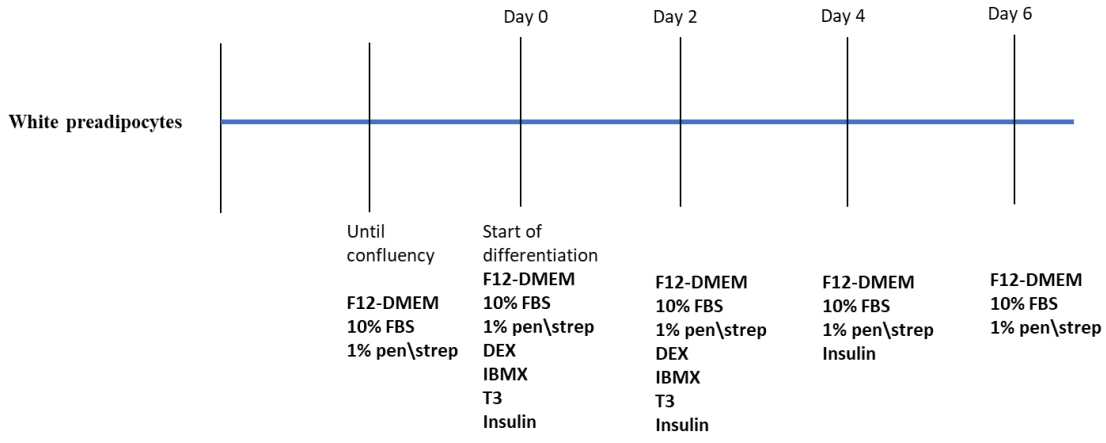

Methods Figure 1: Summary of white preadipocyte differentiation protocol

2.4 Tissue homogenization and RNA isolation

Snap-frozen tissue pieces (5-20 mg) were kept on dry ice and transferred one at a time to 2 ml tubes containing 1 ml TRIzol with ice chilled steel bead. The tissue pieces were homogenized using Tissue lyser (2 x 30s, 30Hz) for 2-5 sec until no visible large particles remain and then immediately put on ice.

2.5 RNA isolation from frozen tissues

0.2ml chloroform was added to lysed tissue and vortexed vigorously for 30 sec to mix phases. After 15 mins of incubation at RT and centrifugation was carried out at 10.000 g for 10 mins at 4 °C. The upper phase, (approx. 400 µl) was transferred to a 1.5 mL tube and place on ice. 0.6 volume (e.g., 240 µl) 96-100% seq-grade EtOH was then added and briefly, vortexed and spin down, this was then loaded into an EcoSpin column (blue), centrifuged for 13.000 g for 30 sec at RT and the flow through was discarded. The column was washed 1x with 500 µl seq-grade RPE buffer at RT, then spinned at 13.000 g for 30 sec between the washes and the flow through was discarded. 80 ul DNase mixture was added directly on top of the column membrane and placed at 37 °C for 30 mins. The column is then washed 2x with 500 µl seq-grade RPE buffer at RT, spinned 13.000 g for 30 sec between the washes and the flow through was discarded. After the last wash the column was placed back in the collection tube and the column was spinned dry at 13.000 g for 2 mins at RT. Columns are then transferred to a new 1.5 mL tube and incubated with lid open for 10 mins at RT to completely evaporate ethanol. RNA was eluted in 100 µl RNAse -free H2O added to the center of the column, incubated for 2 mins at RT, and centrifuged at 9000 g for 2 mins at RT. The eluted RNA was placed immediately on ice and quality test was performed. The RNA concentration and quality was measured in 1 ul of sample by the Nanodrop (A260/A280 and A260/A230 ≥ 1.8 or better ≥ 2), and also the RIN score was measured with the Bio-analyzer according to manufacturer’s protocol.

2.6 Transcriptomics

For identifying differentially expressed genes between ADAM17 knockout and wildtype control, bulk tissue RNA sequencing was done using RNA isolated from liver, inguinal, epididymal and brown adipose tissue, collected from overnight fasted ADAM17 knockout and WT mice. Differentially expressed genes were selected based on a p value < 0.05, calculated using Student's t test and false discovery rate analysis. Transciptomic analysis was performed by the genomic core facility at a Helmholtz center, Munich, Germany. The QIAGEN Ingenuity Pathway Analysis (QIAGEN IPA) was used for the differential gene expression analysis.

2.7 Quantitative real-time polymerase chain reaction (RT-qPCR)

500 ng -1 ug of mRNA was used for cDNA synthesis using the Revert Aid First Strand cDNA Synthesis Kit (Cat. # K1622kit) according to the manufacturer's instructions. The cDNA was PCR amplified using the PowerUp SYBR Green Master Mix 5x, Cat. # A25777. qPCR primers were designed to span exon–exon sequences to generate a product of 100–200 bp (find sequence table below). qPCR was done using Applied Biosystems Quant Studio 6 and 7 Flex Real-Time PCR (ThermoFisher). The mRNA levels of each gene were calculated with the 2^ddCt method and normalized for the expression mRNA of the housekeeping gene.

Component	**Volume per reaction**
PowerUp SYBR® Green Master Mix	5 µL
cDNA template	0.25 µL (2-10 ng)
Forward and reverse primers	5 µL (final concentration 1 µM)
Total volume	10 µL

2.8 Total Protein isolation from cells

Cells were lysed with lysis buffer composed of 20 mM Tris with pH 7.5, 150 mM NaCL, 20 mM ß-glycerophosphate, 5 mM MgCl, 5% glycerol, 0.2% NP40, 0.2% Triton-X, supplemented with protease and phosphatase inhibitors. Cells were scraped with the end of a pipette tip and transferred to clean tubes. The cell suspension was incubated for 30 mins on ice, and vortexed every 10 mins. Soluble proteins were collected after centrifugation for 15 mins at 10000 x g at 4 °C. Soluble proteins were boiled for 7 mins in Laemmli buffer and then loaded to a TRIS-glycine gel.

2.9 Extraction of membrane proteins for ADAM17 protein detection.

Briefly, cells (3 wells of a 12-well plate) were placed on ice, washed with distilled water (4 °C) and incubated with TE buffer (10 mM Tris ph8,1 mM EDTA, 1X Pic,100 ul/well for 10 mins on ice). Cells were then scraped, pooled, transferred into Eppendorf tubes, and then disrupted by repeated aspiration and ejection with a 27G needle. After centrifugation (800 g / 10 mins / 4 °C), the supernatant was pipetted into fresh tubes and again centrifuged (90000 g / 30 mins / 4 °C). The resulting pellet was resuspended in 50 µl TE buffer / 1% SDS / 1x PIC, solubilized by incubation at 95 °C for 5 mins, then centrifuged at 15000 g for 15 mins. Supernatants are aliquoted and stored at -20 °C or used for determination of protein concentration by BCA assay.

2.10 Western blot

10 to 25 µg of soluble protein were boiled at 90 °C for 7 mins in Laemmli buffer and then loaded to a TRIS-glycine gel (Invitrogen). Proteins were transferred to a PVDF membrane with semi-dry transfer for 14 mins at constant 1.4 mA using the Trans-Blot Turbo transfer system from BIO-RAD. Membranes were blocked with 5% milk for 30 mins and incubated overnight with the primary antibody (1:1000) in 5% milk. Washes were done with 0.1% and 0.05% TBS-Tween buffer

and secondary antibody was used 1:1000 for 1 h at RT. Antibodies used in this study are listed below.

2.11 Flow cytometry and staining

After SVF isolation, cells were seeded into 10 cm dish and put in incubator at 37 °C for cells to recover. After 48 hours post incubation, cells were washed 2 times with warm 1x DPBS. After trypsinization, cells were centrifuged at 600 g for 10 mins (use 15ml falcon tube). Cell pellet was washed with ice chilled FACS buffer (1x DPBS + 3% FBS) and centrifuged 600 g for 10 mins at 4 °C. Cells were resuspended in approximately 2-3 ml of blocking buffer (anti-mouse CD16/32 antibody at dilution 1:100) and cells were counted using automated cell counter. Seed 300,000 cells per well of a 96 round bottom plate-if volume per well is less than 200 ul top up with FACS buffer. Incubate plate at 4 °C for 10 mins.

Staining: cocktail

ADAM17 (Prodomain) antibody dilution- (1.5 µl in 100 µl blocking buffer)

CD31 dilution-- (1 µl in 100 µl blocking buffer)

CD45 dilution –- (1 µl in 100 µl blocking buffer)

An antibody cocktail was prepared with the dilutions above. After 10 mins of blocking, plate was centrifuged at 600 g for 2 mins at 4 °C. Cells were then incubated with antibody cocktail, 200 µl per well or each antibody alone and unstimulated cells as control, for 30 mins at 4 °C. (NB: during incubation plate was pulse vortexed every 5 mins). Cells were washed 2 times with FACS buffer, 200 µl per well. Secondary staining was performed with a dilution of 1.5 µl of antibody in 100 ul of FACS buffer. Cells were incubated for 30 mins, at 4 °C and then washed 3 times with FACS buffer. Cells were harvested into FACS tube and sorted using BD FACS Ariel sorter.

2.12 Measurement of body composition and metabolic phenotyping (TSE phenotyping).

Mice were put in PhenoMaster (TSE Systems, Bad Homburg vor der Höhe, Germany), and using combined indirect calorimetry EE, RER, locomotive activity,

and food intake were measured. After the measurement, exported data was analyzed using an online web-based tool at https://CalRapp.org/. In addition, body composition assessment was performed in mice using an EchoMRI™-100 H Body Composition Analyser (Echo Medical Systems, LLC).

2.12.1 Single-dose injection of CL 316,243

We put 12–16 weeks old mice, fed on chow diet in the PhenoMaster for 7 days to acclimatize. A single low dose of CL 316,243 (0.5 mg/kg) was injected i.p. into the mice. Measurement of EE, RER, and locomotor activity were collected for 24 h post injection.

2.12.2 Five days CL 316,243 injection and cold exposure

We put 12–16 weeks old mice, fed on chow diet in the PhenoMaster for 7 days to acclimatize. Mice were given i.p. injections of low dose of CL 316,243 (0.5 mg/kg) every second day for 5 days.

Cold temperature exposure: We put 12–16 weeks old mice, fed on chow diet in the PhenoMaster for 7 days to acclimatize by gradual drop in temperature for 1 week. For 2 weeks, we exposed mice to cold air environment (8 °C). Measurement of EE, RER, and locomotor activity were collected for the 2 weeks when mice were exposed to cold air.

2.13 Intraperitoneal glucose tolerance test (IPGTT).

Before the IPGTT, mice were fasted for 5 or 16 hours and then challenged with 25% of glucose (2 g/kg body weight) intraperitoneally. Glucose was assessed at 0, 7, 15, 30, 60, 90, and 120 minutes via tail vein bleeding using a glucometer (AccuChek Performa Monitor). Tail blood was collected at time different time points for measurement of glucose induced insulin and c-peptide as described by (Georgiadi *et al*., 2021).

2.14 Insulin tolerance test

Before the IPGTT, mice were fasted for 6 hours and then challenged with insulin intraperitoneally (0.8 U/kg body weight). Insulin induced glucose levels were assessed at 0, 20, 40, 60, and 120 minutes via tail vein bleeding by a glucometer (Performa Monitor).

2.15 Pyruvate and glycerol tolerance test

Mice were fasted for 16 hours overnight, and this was followed with an intraperitoneal Sodium pyruvate or glycerol injection (2 g/kg body weight). Glucose was assessed at 0, 7, 15, 30, 45, 60, 90, and 120 minutes via tail vein bleeding using a glucometer (AccuChek Performa Monitor).

2.16 Enzyme-linked immunoassay (ELISA)

2.16.1 Insulin and c-peptide measurements

Plasma or serum insulin and c-peptide levels were measured using kit from Alpco (cat. #80-INSMS-E01) and CrystalChem (cat. # 90050) respectively. All measurements were done following the manufacturer's instruction.

2.16.2 Corticosterone ELISA

Plasma corticosterone levels were measured using DetectX® Corticosterone ELISA Kit (K014-H5) from ARBOR assays according to manufacturer's protocol. Briefly, plasma samples were dissociated in dissociation buffer as stated by the manufacturer. Samples were pipetted into each well and after addition of corticosterone conjugate and antibody; plate was incubated at RT shaking at 800 rpm for 1 hr. Following 1-hour incubation at RT, wells were washed 4 times and 100 ul of TMB-substrate solution was added into each well. After 30 minutes incubation in dark, at RT, the reaction was stopped with stop solution and absorbance

was measured immediately at wavelength 450 nm. Results were analyzed as stated by manufacturer.

2.16.3 Glucagon Elisa

Serum and plasma glucagon levels were measured using mouse glucagon Elisa kit from Mercodia (cat. # 10-1281-01) following the manufacturers instruction. Briefly, 10 ul of each calibrator, controls and samples were pipetted into appropriate wells. 50 µl of enzyme conjugate 1x was added to each well and plate was incubated on a plate shaker shaking at 800 rpm overnight at 4 °C. After 6 times washing with wash buffer, 200 ul of TMB substrate was added to each well. Following 30 minutes incubation at RT, shaking as stated above, the reaction was stopped, and plate was read at optical density of 450 nm. Results were analyzed as stated by manufacturer.

2.17 Glycogen Assay

Glycogen assay was done from liver extract using the Abcam glycogen colorimetric assay kit II (cat # ab169558) according to manufacturer's instruction. Briefly about 20 mg of pulverized liver tissue was weighed and homogenized in hydrolysis buffer provide with the kit in tissue lyzer. After 10 minutes incubation on ice, homogenates were boiled at 90 °C to inactivate the enzyme for 10 mins. After centrifugation at 14300 rpm, supernatant was collected and used for the glycogen assay as stated by manufacturer at 1 to 40 dilutions.

2.18 Tissue lipid extraction and TG measurement

30-50 mg of Powdered frozen liver tissue was accurately weighed and weights recorded. Tissue is then put in a 2 mL safe lock tube with ice chilled steel bead. 1.5 mL of chloroform: methanol (2:1) mixture (maintained at -80 °C; final volume is about 1.6 mL) is then added using a combi tip. The tissue was then lysed with Qiagen Tissue Lyzer (2 x 30s, 30 Hz) until no visible large particles remain. The

lysed tissue was spanned down briefly and mix for 20 mins on Thermomixer at 1400 rpm, RT. This was followed by 30 mins centrifugation at 13000 rpm at 20 °C. 1 mL of supernatant (i.e., liquid phase) was transferred to a new 2 mL tube and 200 µL of 150 mM (0.9%) NaCl was added. The mixture was then mixed by shaking vigorously and then centrifuged for 5 mins at 2000 rpm. During this time, 40 µL of chloroform: Triton-X (1:1) solution was pipetted into fresh 1.5 mL tubes using a combi tip. The upper phase was carefully removed, after which 200 µL of the lower organic phase was taken, taking care not to contaminate tip with the remaining upper phase and transfer into new tube containing the chloroform: Triton-X. The organic phase is dried with speed vac overnight (or until no change in tube weight). 200 µL of double distilled water was added to the remaining triton-lipid solution and was then mixed well on rotation for 1 h at RT and store at -80 °C until required (final volume 225 µL, 1:125 dilution factor). TGs were measured by the Sigma Triglyceride determination Kit (Cat. # TR0100).

2.19 Lipolysis Assay

The non-esterified fatty acids (NEFAs) released by the cells and in plasma or the NEFA HR (2) Kit (WAKO) measured serum. Briefly, 2 to 10 µL of samples and standard in duplicates were measured on 96-well microplates by first adding 100 µL of R1 buffer and incubating at 37 °C for 10 mins followed by adding 50 µL R2 buffer and followed by a similar incubation. The measurement was carried out at 550 nm and the NEFA amounts were calculated using the following formula:

NEFA (mg/dl) = (Esx28.2)/Estd

Es- Absorbance of the sample (= Raw absorbance of sample – absorbance of reagent blank i.e., water)

Estd- Absorbance of standard (= Raw absorbance of standard – absorbance of reagent blank i.e., water)

2.20 Fasting and refeeding challenges

2.20.1 In vivo

To study the fasting-refeeding effect on Adipose Tissue ADAM17, wild type C57BL/6 mice were used and either fed for 18 h (ad libitum mice) with chow diet, fasted for 18 h (fasting mice) or fasted for 16 h and refed for 4 h (refeeding mice). A minimum of 4 biological replicates were used in each experiment. The fasting refeeding was performed according to the circadian rhythm of the mice. All animals were sacrificed at the same time point by cervical dislocation. Liver, epididymal, inguinal, brown adipose tissues from these animals were isolated, weighed, snap frozen and analyzed via qPCR after RNA isolation. See fasting timeline below.

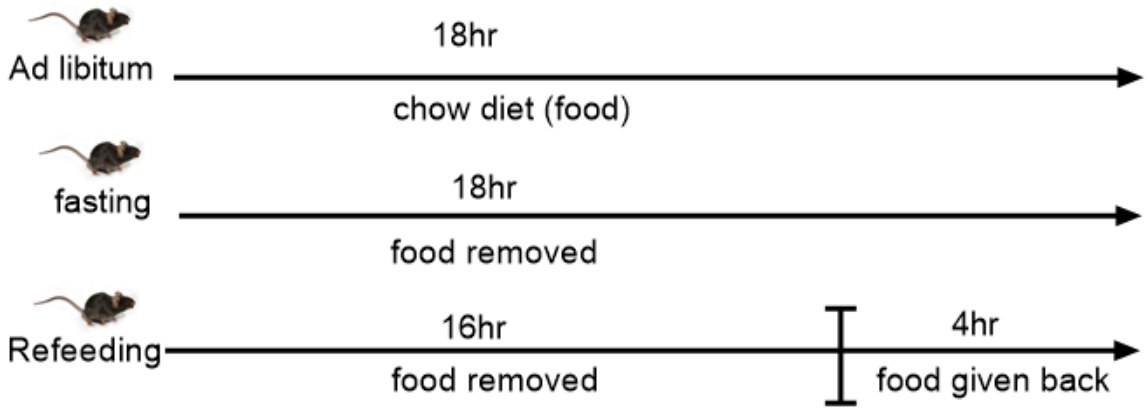

Methods Figure 2: Fasting-refeeding conditions in vivo in wildtype mice.
Mice were fasted for 18 h and refed for 4 h. The ad libitum fed mice were not fasted. All mice were killed at the same period.

2.20.2 In vitro

For the in vitro fasting experiments, all experimental wells of differentiated primary adipocytes were treated with Starvation media for 3 hours for initial priming to avoid influence of previous media. To mimic feeding conditions in vitro, differentiated cells were cultured with complete media (DMEM high glucose (4 g D-Glucose/liter), 5% FBS and 1% P/S) with and without 100 nm insulin, and to mimic

fasting in vitro cells were cultured with either starvation media only (4 g D-Glucose/liter), no FBS and 1% P/S) , or forskolin (10 um) and glucagon (100 nm) in starvation media for 6 hours. After treatment, cells from each experimental wells were washed with ice chilled DPBS and subsequent qPCR was performed.

2.21 Invitro CL 316,243 experiments

2.21.1 Incubation of mouse primary adipocytes with CL 316,243

Mouse brown and white adipocytes from Adip^{Cre+}Adam17KO and Adip^{Cre-}WT mice were stimulated with 100 nm CL 316,243 for 2 h. Adrb3 protein levels were detected by immunoblotting.

2.21.2 CL 316,243 treatments with Tapi-2

Mouse primary adipocytes were stimulated 30 mins. with and without Tapi-2, after 2 h of treatment with 100 nm Cl316. Western blot for pHSL, pCreb and pATF-1 was performed using beta actin as control.

2.21.3 In vitro treatment with beta-adrenergic receptor agonists.

Primary mouse adipocytes were stimulated for 4 hours with 100 nm of Forskolin, CL 316,243, Formoterol or Dobutamine. The transcriptional levels of ADAM17, Adrb3 and Adrb2 was measured using RT-qpcr.

2.22 Proteomics analysis in differentiated adipocytes

For primary adipocyte proteomics analysis, on day 6 after differentiation, cells were washed with warm PBS, and 1 ml of starvation media was added to each well of a 12 well plate for 2 hours. After the initial 2 h of starvation called ´´priming´´, the cell culture media was again changed to 600 µl of starvation media for

16 hours overnight. After overnight starvation, 400 µl of culture supernatant was collected from each well. All collected supernatant and their respective cells, from each experimental group was pooled together, forming a 4 pool per treatments and these represent the 4-replica used for the media and cell proteomic analysis.

2.22.1 Media proteomics

Harvested cultured supernatant was centrifuged at 3500 g, for 10 mins at RT. 300 µl of supernatant was collected after centrifugation and 1x halt protease inhibitor cocktail was added per each aliquot. Samples were snap frozen immediately in liquid nitrogen.

2.22.2 Cells (Adipocyte) proteomics

At the end of the overnight starvation, cells were washed with 2 ml cold 1x PBS per well of a 12 well plate. Cells were lysed with 80 µl of RIPA buffer per well, cells were then scraped and 3 wells from each group were harvested and pooled together to form 4 experimental replicates.

2.22.3 Proteomic analysis in differentiated adipocytes

Total tissue proteomics was performed using tissues (liver, BAT, iWAT and gWAT) collected from WT and ADAM17KO mice after overnight starvation in mice and in some experiments in tissues (liver, BAT, iWAT and gWAT) collected from WT and ADAM17 knockout mice following intraperitoneal glucose or saline injection. Proteomic analysis was performed by the proteomic core facility at Helmholtz center, Munich, Germany. The QIAGEN Ingenuity Pathway Analysis (QI-AGEN IPA) was used for the differential gene expression analysis.

2.23 Online Single cell data

Publicly available single cell data set of (Sárvári *et al*., 2021) was analyzed with focused on the eWAT from chow diet fed male mice. Also, from the online single nuclei dataset from (Emont *et al*., 2022), analysis was done in the visceral and subcutaneous fat from lean and obese mice and human. Lastly, brown adipose tissue online single set data from human and mice that were at room temperature and cold temperature, published by (Sun *et al*., 2020) was analyzed. Visualization of all datasets was done using the Single Cell Portal (singlecell.broadinstitute.org).

2.24 Media

2.24.1 Primary pre-adipocyte differentiation media:

2.24.1.1 Isolation buffer

Dulbecco has modified Eagle's medium (DMEM)/ F12 (1:1) supplemented with 10% fatal bovine serum (FBS), 1% Penicillin/ Streptomycin (P/S).

2.24.1.2 Digestion buffer

Contains 4 mg/ml Collagenase type II, 10 mM Calcium Dichloride (MM: 147 g/mol) diluted in Dulbecco's Phosphate Buffered Saline (PBS) with 0.5% bovine serum albumin (BSA) per two fat pads.

2.24.1.3 Induction media

DMEM high glucose, 10% FBS + 1% penicillin (P/S), dexamethasone (2 ng/ml), IBMX (122 ng/ml), T3 (6.7 ng/ml), insulin (0.865 ng/ml) and Rosiglitazone (5 ng/ml)

2.24.1.4 Maintenance media

DMEM high glucose (4.5 g D-Glucose/liter), 10% FBS + 1% P/S, 0.4325 ng/ml insulin

2.24.1.5 Starvation media (reduced nutrient buffer)

DMEM low glucose (1 g D-Glucose/litre), no glutamine, no phenol red, no pyruvate, no serum and 1% P/S

2.24.1.6 Complete media

DMEM high glucose (4 g D-Glucose/litre), 10% FBS and 1% P/S

2.25 **Instruments**

Automated cell counter (Countess)	Life Technologies (Invitrogen)
Automatic glucose monitor (Accu-Chek Performa)	Roche
Bacterial incubator (Function Line)	Thermo Scientific (Heraeus)
Bacterial shaker	Infors AG
Bacterial shaker / incubator (Multitron Standard)	Infors HT
Benchtop centrifuge (Microfuge Heraeus Pico)	Thermo Scientific (Heraeus)
Benchtop centrifuge, cooling (Microfuge Heraeus Fresco)	Thermo Scientific (Heraeus)
Blot imager (ChemiDoc XRS)	Biorad
Centrifuge (Biofuge Prime) (cell culture)	Thermo Scientific (Heraeus)
Centrifuge (Labofuge 400R)	Thermo Scientific (Heraeus)
Centrifuge (Mikro 22R) (cell culture)	Hettich
Centrifuge (Multifuge X3R)	Thermo Scientific (Heraeus)
Centrifuge (Super T21)	Thermo Scientific (Heraeus)
Freezer -20 °C (comfort / med line)	Liebherr
Freezer -80 °C (Herafreeze)	Thermo Scientific (Heraeus)
Fridge 4 °C (comfort / med line)	Liebherr
Fumehood (Airflow RXC 90.1)	WALDNER Laboreinrichtungen
Freezer -20 °C (comfort / med line)	Liebherr
Freezer -80 °C (Herafreeze)	Thermo Scientific (Heraeus)
Fridge 4 °C (comfort / med line)	Liebherr
Fumehood (Airflow RXC 90.1)	WALDNER Laboreinrichtungen
Hotplate stirrer (Model 375)	VWR
Labcoat	Bierbaum Proenen
Liquid nitrogen cryogenic tank	Thermo Electron
Microplate reader (Mithras LB 940)	Berthold
Microplatereader SPECTROstar Omega	BMG Labtech
Microscope (Axio Imager.M2) (histology)	Zeiss
Microscope (Axiovert 40 CFL) (cell culture)	Zeiss
Microwave	Bosch

Mini Trans-Blot® cell (buffer tank, lid, cassettes, electrodes)	Biorad
Multichannel pipette reference 8- and 12-channel variable	Eppendorf
Multistep pipette (Multipette Plus)	Eppendorf
pH meter (GMH350)	GHM electronics, Greisinger
PhenoMaster cages	TSE Systems
Photometer (NanoDrop ND-1000)	Peqlab Biotechnology
Pipette controller (accu-jet® pro)	Brandtech Scientific
Real-Time PCR system (StepOnePlus)	Life Technologies (Applied Biosystems)
Rocking platform (Duomax 1030)	Heidolph
Rotating wheel	Neolab
Rotating wheel (model 2-1184)	Neolab
Scales (EG 2200-2NM)	Kern & Sohn Gmbh
Sonicator (Bioruptor)	Diagenode
Sterile biosafety cabinet (e3 Class II Type A/B)	SterilGARD
Tabletop centrifuge (Mini Spin Plus)	Eppendorf
Thermomixer comfort Heatblock	Eppendorf
Timer (TR 118)	Oregon Scientific
TissueLyser II	Qiagen
Ultracentrifuge (XL 70)	Beckman
Vacuum pump	Neolab

2.26 Chemicals and reagents

Chemical/ Reagent	**Company**
ADAM17 recombinant protein (2978-AD)	R&D systems
Albumin Bovine Fraction V, Protease and Fatty Acid-Free	Serva
Collagenase type II	Gibco
cOmplete™ Mini EDTA-free Protease Inhibitor Cocktail	Roche Diagnostics
Chloroform	Carl Roth
Dulbecco's Modified Eagle Medium (1x), high glucose + GlutaMAX™, Pyruvate	Gibco
Dulbecco's Modified Eagle Medium (1x), no glucose, no glutamine, no phenol red, no sodium pyruvate	Gibco
Dulbecco's Modified Eagle Medium/ Nutrient Mixture F-12	Gibco
Dulbecco's Phosphate Buffered Saline (1x), no calcium, no magnesium	Gibco
Dexamethasone	Sigma Aldrich
Dimethyl sulfoxide	Sigma Aldrich
Dulbecco's modified Eagle's serum (DMEM) + GlutaMAX™	Gibco
Ethanol absolute (for analysis) 32205	Sigma
Fetal bovine serum, sterile filtered	Sigma Aldrich
Forskolin (F3917)	Sigma

Glycerol 2-phosphate disodium salt hydrate (G2P) G6251	Sigma
HEPES Buffer Solution (1M)	Gibco
Human Glucagon (Y0000191-2EA)	Sigma Aldrich
IBMX	Sigma Aldrich
Immobilon Western Chemiluminescent HRP Substrate	Merck Millipore
Indomethacin	Sigma Aldrich
Insulin solution human, sterile filtered (I9278)	Sigma Aldrich
Isopropanol (190764)	Sigma Aldrich
Penicillin/ Streptomycin	Gibco
Ponceau S solution	Sigma Aldrich
PowerUp SYBR Green Master Mix	Thermo Fisher Scientific
PhosSTOP™	Roche Diagnostics
Precision Plus Protein™ Kaleidoscope™ Prestained Protein Standards	Bio-Rad
Sodium pyruvate	Sigma
Red Blood Cell Lysing Buffer Hybri-Max™	Sigma Aldrich
Restore™ PLUS Western Blot Stripping Buffer	Thermo Fisher Scientific
Rosiglitazone	Sigma Aldrich
SuperSignal™ West Femto Maximum Sensitivity Substrate	Thermo Fisher Scientific
Trans-blot Turbo 5x Transfer Buffer	Bio-Rad
Triiodo-L-thyronine sodium salt	Sigma Aldrich
TRIzol Reagent	Thermo Fisher Scientific
Trypsin, 0,05 % with EDTA	Gibco

2.27 Plastic consumables

Product	**Supplier**	**Catalogue number**
10µl Graduated tips	Starlab	S1111-3800
1000µl Blue graduated tips	Starlab	S1111-2821
10ml Disposable Polystyrene Serological Pipet	Corning (Falcon)	356551
15ml Tube PP, sterile (cellstar)	Greiner Bio One	188271
200µl Yellow tips	Starlab	S1111-0806
250mL Vacuum Filter/Storage Bottle System, 0.22µm Pore	Sigma (Corning)	430756
25ml Disposable Polystyrene Serological Pipet	Corning (Falcon)	356535
300 µM Nylon mesh (Polyamid Monofil)	Neolab	4-1411
50ml Disposable Polystyrene Serological Pipet	Corning (Falcon)	356550
50 ml Syringe	BD Biosciences (Falcon)	1404297
50ml Tube PP, sterile (cellstar)	Greiner Bio One	227261
5ml Disposable Polystyrene Serological Pipet	Corning (Falcon)	356543
70µM Cell strainer nylon	BD Biosciences (Falcon)	352350

96 Well Black with Clear Flat Bottom	Corning (Falcon)	353219
96-Well Microplates, clear, flat bottom (MicroWell)	Thermo Scientific (Nunc)	95029780
Bench liner (Labmat)	VWR	246750000
Cell counting chamber slides (Countess)	Life Technologies (Invitrogen)	C10228
Cell Culture Dishes 100x20 mm	Corning (Falcon)	353003
Cell Culture Dishes 150x25 mm	Corning (Falcon)	353025
Cell Scrapers	Sigma (Corning)	CLS3010
Combitips advanced, 10 mL	Eppendorf	30089464
Combitips advanced, 5 mL	Eppendorf	30089456
Cover Slips	Carl Roth	H878.2
Cryo Cardboard Box, White	Neolab	Feb 01
Cryogenic vials, 1.8ml	Starlab	E3110-6122
Delicate Task Wipes	Kimberley Clark	7216
Dialysis tubing Cellulose Ester	Spectrum Laborato-ries	131270
Disposable Scalpels	Feather	EF7281 (2975-10)
Disposal bags (Sekuroka)	Carl Roth	E706.1
FPLC column (Superose 6, 10/300 GL)	GE Healthcare Life Sciences	17-5172-01
Gas cartridge	Campingaz	Z00059581
Gloves, Powder Free Textured Latex Exam	blossom	BM 11226-PF-AV
Glucose test strips (Acco-Chek Inform II)	Roche	473360
Grid insert for cryoboxes, 10x10	Neolab	Feb 03
Histology Mega-Cassette System (Tissue-Tek)	Sakura	4173
Insulin syringes (Micro-fine 1ml U-40, 0.33 mm x 12.7 mm)	Becton Dickinson	320801
large volume centrifuge tubes	Sigma (Corning)	CLS431123

2.28 **Antibodies**

Name	**Company**	**Catalog number**	**Host**	**Dilution**
Primary antibodies				
Anti-ADAM17 Cytoplasmic Domain Antibody	Kerafast	EHS008	Mouse	1:1000
Anti-ADAM17 Prodomain Antibody	Kerafast	EHS009	Mouse	1:500
Secondary antibodies				
Polyclonal Goat Anti-Mouse Immu-noglobulin HRP	Dako	P0448	Goat	1:5000
Polyclonal Swine Anti-Rabbit Immu-noglobulin HRP	Dako	P0339	Swine	1:5000

2.29 Primers

Gene	Forward primer	Reverse primer
mADAM17 exon1-2	CATCCGCGACTTGAGAA-GCTTGA	GATGTCAAGTATAATTTAAAA TGTCTTTTCAAAGC
mADAM17 exon2-3	GCTTTGAAAAGA-CATTTTAAATTATACTT-GACATC	CCAGAGGTCACGCTG-TACTCG
mADAM17 exon3-4	GTCACGTGGTT-GGTGAGCCTGACT	GACAAAC-CTCCAAAGTGGCTCTACGT
mADAM17 exon4-5	ACGTAGAGCCACTTT-GGAGGTTTGTC	CTCGAC-GAACAAACTCTTCAGATGGCT CT
mADAM17 exon5-6	GCCATCTGAAGAGTTT-GTTCGTC	GTCAATTAGCTC-TATTAAGTAATTTGTAG
mADAM17 exon6-7	CTACAAATTACTTAA-TAGAGCTAATTGA	ATCAAAGCTAAATTGCTCTAA-TAGCATC
mADAM17 exon8-9	GATGCTATTAGAG-CAATTTAGCTTTGAT	CACAGTTGGGTTGTAATAA-GCTTTTGGAC
mADAM17 exon9-11	GTCCAAAA-GCTTATTACAACCCAACTGTG	CCAGGTCAGCTTCCTTT-GTGAGAATAG
mADAM17 exon10-12	CTATTCTCACAAAGGAA-GCTGACCTGG	GCAGTTT-GAAAACATCTTATTATTCTCG TG
mADAM17 exon11-12	CACGAGAATAATAA-GATGTTTTCAAACTGC	GACTGTTCCTATCACTGCAC-TGCAC
mADAM17 exon12-14	GTGCAGTGCAGTGA-TAGGAACAGTC	CTCACTGCTATTCCCTGTG-CAGTAAGAC
mADAM17 exon15-17	TGCGACATGAATGG-CAAATGTGAGAAAC	TGTCCAG-TTTCTTATCCACACAGTG-GACA
mADAM17 exon16-18	TGTCCACTGTGTGGATAA-GAAACTGGACA	GCTGCTCAG-CATCTCAATGTTACTGTGATG
mHRPT	TCAGTCAACGGGG-GACACATAAA	GGGGCTGTACTGCTTAAC-CAG
mTBP	TTCCAAAACTCCGGGTAGGC	AACCGATTCCGCACAGTCTT
mß-actin	GTGACGTTGACATCCG-TAAAGA	GCCGGACTCATCGTACTCC
ADAM17_genotyping primers from Jackson	TCC CCC AGC TAG ATT GTT TG	AGG ACC CAG GTT CAG TTC CT
Cre_detection	GAAC-CTGATGGACATGTTCAGG	AGTGCGTTCGAACGCTA-GAGCCTGT
Myosin	TTACGTCCATCGTGGACAGC	TGGGCTGGGTGTTAGCCTTA

2.30 **Commercially available kits**

Description	**Company**
Mouse Insulin ELISA kit (cat. #80-INSMS-E01)	ALPCO
Pierce™ BCA Protein Assay Kit	Thermo Fisher Scientific
ADAM17 ELISA Kit (Mouse) (OKCD02340)	Aviva Systems Biology
First strand cDNA Synthesis Kit	Life Technologies
Mouse c-peptide ELISA kit (cat. # 90050)	CrystalChem
DetectX Corticosterone ELISA Kit (K014-H5)	ARBOR
Mouse glucagon Elisa kit (cat. # 10-1281-01)	Mercodia
Glycogen colorimetric assay kit II (cat # ab169558)	Abcam
Triglyceride determination Kit (Cat. # TR0100)	Sigma
NEFA HR (2) Kit	WAKO

3. Results

3.1 Deletion of ADAM17 in white adipocytes results in decreased expression levels on mitochondrial complex I, and increased gene makers of lipogenesis and glucose, fat uptake pathways.

To investigate potential metabolic pathways affected by ADAM17 deletion in adipocytes, we performed bulk RNA seq and untargeted proteomics in iWAT-SVF derived white adipocytes from Adip^{Cre+}Adam17KO and Adip^{Cre-}WT mice. Both Adip^{Cre+}Adam17KO and Adip^{Cre-}WT white adipocytes were kept overnight in serum free media, with high glucose to ensure no traces of serum were present for the purpose of performing untargeted proteomics. The same conditions were also used for the Adip^{Cre+}Adam17KO and Adip^{Cre-}WT mice, white adipocytes send for bulk RNAseq. Total RNA transcriptomics revealed that 648 genes were differentially expressed between Adip^{Cre+}Adam17KO compared to Adip^{Cre-}WT white adipocytes. Out of these, 288 were upregulated and 360 genes were downregulated in Adip^{Cre+}Adam17KO vs Adip^{Cre-}WT white adipocytes. Ingenuity Pathway analysis showed the top regulated pathways involved genes of mitochondrial respiratory chain (Table 3). We examined closer the major metabolic pathways with such as glycolysis, lipolysis, fatty acid esterification/lipogenesis, Krebs cycle and oxidative phosphorylation. We observed that Adip^{Cre+}Adam17KO adipocytes had higher expression levels of glucose uptake and fatty acid uptake receptor, such as Slc2a4 (Glut4) and Cd36, Lpl respectively (Fig. 3a, b), higher expression levels of lipogenesis genes such as Gpat4, Dgat1 and Dgat2, Acsl1 (Fig. 3c), higher expression of genes involved in fatty acid oxidation such as, Cpt2, as well as TCA cycle gene Mdh1, Idh3a (Fig. 3d). Several genes encoding of the mitochondrial respiratory chain complex 1 such as mt-Nd3, mt-Nd4, Ndufa1, Ndufa12 (Fig. 3e) along with mitochondria transport proteins, such as Tomm5, Tomm7 were downregulated (Fig. 3f) in the ADAM17KO adipocytes vs WT adipocytes.

Table 3: Differentially expressed Metabolic Pathways calculated based on RNAseq data of Adip^{Cre+}Adam17KO vs Adip^{Cre-}WT iWAT (SVF derived) adipocytes ranked according to -log(p-value). Z-score is a predictor of pathway regulation (+: upregulated, -: downregulated). Generated with Ingenuity Pathway analysis.

Ingenuity Canonical Pathways	-log(p-value)	Ratio	z-score	Molecules
Sirtuin Signaling Pathway	4,36	0,0479	2,714	APEX1,DUSP6,FOXO1,H1-10,MAPK12,MT-ND3,MT-ND4L,NDUFA1,NDUFA12,NDUFS6,RRP9,SLC2A1,Tomm5,TOMM7
Granzyme A Signaling	4,18	0,0933	1,89	APEX1,H1-10,MT-ND3,MT-ND4L,NDUFA1,NDUFA12,NDUFS6
Dopamine Receptor Signaling	4	0,0875	1	ADCY7,DRD1,GCH1,MAOB,PPP1CC,PPP1R3C,PRKAR2B
Mitochondrial Dysfunction	3,6	0,0406	1,069	COX11,GPD2,GSTP1,GSTZ1,HTRA2,MAOB,MAPK12,MT-ND3,MT-ND4L,NDUFA1,NDUFA12,NDUFS6,PRKAR2B,TOMM7
ERK/MAPK Signaling	3,17	0,0465	-0,632	DUSP6,ITGA5,PAK1,PAK4,PPP1CC,PPP1R3C,PRKAR2B,RPS6KA5,SOS2,VRK2
Semaphorin Neuronal Repulsive Signaling Pathway	3,02	0,0533	-0,707	CFL1,DPYSL2,FES,ITGA5,LIMK1,PAK1,PAK4,PRKAR2B
PAK Signaling	2,99	0,0598	-1,633	CFL1,ITGA5,LIMK1,MAPK12,PAK1,PAK4,SOS2
cAMP-mediated signaling	2,86	0,0424	-0,333	ADCY7,AKAP7,APEX1,CAMK1D,DRD1,DUSP6,PDE3B,PKIG,PRKAR2B,PTGIR
Apelin Adipocyte Signaling Pathway	2,85	0,0659	-0,816	ADCY7,GSTP1,GSTZ1,MAPK12,NOX4,PRKAR2B
Protein Kinase A Signaling	2,85	0,0341	1,155	ADCY7,AKAP7,APEX1,DUSP5,DUSP6,H1-10,PDE3B,PPP1CC,PPP1R3C,PRKAR2B,PTPN4,PTPRN,PYGB,VASP
Cachexia Signaling Pathway	2,83	0,0353	-1,387	ADCY7,CLCF1,DDIT4,FBXO21,FOXO1,MAPK12,NOX4,PDE3B,PRKAR2B,PSMB5,PSME2,SLC2A4,STAT2
RAC Signaling	2,6	0,0511	-1,633	ANK1,CFL1,ITGA5,LIMK1,NOX4,PAK1,PAK4
Insulin Receptor Signaling	2,54	0,05	0	FOXO1,PDE3B,PPP1CC,PPP1R3C,PRKAR2B,SLC2A4,SOS2
Cardiac β-adrenergic Signaling	2,52	0,0444	0,378	ADCY7,AKAP7,APEX1,PDE3B,PKIG,PPP1CC,PPP1R3C,PRKAR2B
Neutrophil Extracellular Trap Signaling Pathway	2,52	0,0326	-1,941	COL5A3,MAPK12,MLKL,MT-ND3,MT-ND4L,NDUFA12,NDUFS6,NOX4,PLA2G7,RIPK3,SLC2A1,Tomm5,TOMM7
Signaling by Rho Family GTPases	2,47	0,0375	-1,667	ARHGEF9,CFL1,ITGA5,LIMK1,MAPK12,NOX4,PAK1,PAK4,RHOC,SEPTIN9
IL-7 Signaling Pathway	2,4	0,0641	0	FOXO1,MAPK12,SLC2A1,SOCS1,SOS2
Oxidative Phosphorylation	2,4	0,0536	-2,449	COX11,MT-ND3,MT-ND4L,NDUFA1,NDUFA12,NDUFS6
Role of JAK family kinases in IL-6-type Cytokine Signaling	2,38	0,0633	-1,342	CLCF1,JUNB,MAPK12,SOCS1,TIMP1
CDK5 Signaling	2,34	0,0522	0,816	ADCY7,DRD1,MAPK12,PPP1CC,PPP1R3C,PRKAR2B
Regulation of Actin-based Motility by Rho	2,34	0,0522	-2,236	CFL1,ITGA5,LIMK1,PAK1,PAK4,RHOC
Xenobiotic Metabolism PXR Signaling Pathway	2,31	0,041	1,414	ALDH6A1,CES1,GSTP1,GSTZ1,MAOB,PPP1CC,PPP1R3C,PRKAR2B
Renin-Angiotensin Signaling	2,23	0,0496	-0,447	ADCY7,MAPK12,PAK1,PAK4,PRKAR2B,SOS2
Role of Hypercytokinemia/hyperchemokinemia in the Pathoger	2,22	0,0581	-2,236	CXCL10,IFIT2,IFIT3,RSAD2,STAT2
Inhibition of ARE-Mediated mRNA Degradation Pathway	2,18	0,0429	-1,342	CNOT4,MAPK12,PABPN1,PRKAR2B,PSMB5,PSME2,SEM1
ERBB Signaling	2,08	0,0538	-1,342	FOXO1,MAPK12,PAK1,PAK4,SOS2
Insulin Secretion Signaling Pathway	1,91	0,0327	-1	ADCY7,CCK,MAPK12,PRKAR2B,RPS6KA5,SEC61B,SLC2A1,SLC2A4,STAT2
Macrophage Alternative Activation Signaling Pathway	1,85	0,037	-1,134	CSF1,IL4R,IRF4,MAPK12,RPS6KA5,SOCS1,ZC3H12A
Paxillin Signaling	1,83	0,0467	-1,342	ITGA5,MAPK12,PAK1,PAK4,SOS2
ISGylation Signaling Pathway	1,82	0,0463	-0,447	IRF4,LIPG,MAPK12,STAT2,USP18
Natural Killer Cell Signaling	1,75	0,0354	-0,378	CFL1,COL5A3,LIMK1,MAPK12,PAK1,PAK4,SOS2
GDNF Family Ligand-Receptor Interactions	1,72	0,0526	-1	DOK1,MAPK12,RET,SOS2
Ephrin Receptor Signaling	1,71	0,0347	-1,134	CFL1,DOK1,ITGA5,LIMK1,PAK1,PAK4,SOS2
Estrogen Receptor Signaling	1,64	0,0269	-0,378	ADCY7,CFL1,FOXO1,LIMK1,MT-ND3,MT-ND4L,NDUFA12,NDUFS6,PAK1,PRKAR2B,SOS2
Chemokine Signaling	1,63	0,0494	-1	CAMK1D,CFL1,LIMK1,MAPK12
FLT3 Signaling in Hematopoietic Progenitor Cells	1,61	0,0488	0	MAPK12,RPS6KA5,SOS2,STAT2
Integrin Signaling	1,61	0,033	-1,134	ARHGAP26,ITGA5,PAK1,PAK4,RHOC,SOS2,VASP
Hepatic Fibrosis Signaling Pathway	1,55	0,026	-1,508	COL5A3,FOXO1,ITGA5,MAPK12,NOX4,PRKAR2B,RHOC,SERPINE1,SOS2,SUCNR1,TIMP1
TR/RXR Activation	1,54	0,0391	-1,342	BCL3,ITGA5,PDE3B,SLC2A1,UCP3
RHOGDI Signaling	1,53	0,0318	1,134	ARHGEF9,CFL1,ITGA5,LIMK1,PAK1,PAK4,RHOC
RAR Activation	1,51	0,0256	-0,302	ADCY7,ADH1C,APEX1,CLCF1,CRABP1,MAPK12,PDE3B,PRKAR2B,RET,RHOC,RPS6KA5
D-myo-inositol (1,4,5,6)-Tetrakisphosphate Biosynthesis	1,46	0,0333	-2	DUSP5,DUSP6,PHOSPHO1,PPP1CC,PPP1R3C,PTPRN
D-myo-inositol (3,4,5,6)-tetrakisphosphate Biosynthesis	1,46	0,0333	-2	DUSP5,DUSP6,PHOSPHO1,PPP1CC,PPP1R3C,PTPRN
ABRA Signaling Pathway	1,45	0,0435	-1	CFL1,JUNB,LIMK1,MAPK12
Actin Nucleation by ARP-WASP Complex	1,44	0,043	-1	ITGA5,RHOC,SOS2,VASP
Reelin Signaling in Neurons	1,42	0,0362	-0,447	ARHGEF9,CFL1,ITGA5,LIMK1,MAPK12
White Adipose Tissue Browning Pathway	1,42	0,0362	-0,447	ADCY7,KLB,MAPK12,PRKAR2B,VGF
Death Receptor Signaling	1,4	0,0417	-1	HTRA2,LIMK1,LMNA,TIPARP
TGF-β Signaling	1,4	0,0417	-1	MAPK12,SERPINE1,SOS2,TGIF1
Salvage Pathways of Pyrimidine Ribonucleotides	1,38	0,0412	-2	CMPK2,LIMK1,NME4,PAK1
Melanocyte Development and Pigmentation Signaling	1,37	0,0408	1	ADCY7,PRKAR2B,RPS6KA5,SOS2
GNRH Signaling	1,35	0,0314	-0,816	ADCY7,MAPK12,PAK1,PAK4,PRKAR2B,SOS2
3-phosphoinositide Degradation	1,35	0,0314	-2	DUSP5,DUSP6,PHOSPHO1,PPP1CC,PPP1R3C,PTPRN
PPARα/RXRα Activation	1,33	0,0309	-1,342	ADCY7,BCL3,GPD2,HELZ2,PRKAR2B,SOS2
D-myo-inositol-5-phosphate Metabolism	1,31	0,0306	-2	DUSP5,DUSP6,PHOSPHO1,PPP1CC,PPP1R3C,PTPRN
Dilated Cardiomyopathy Signaling Pathway	1,29	0,0333	-1,342	ADCY7,CAMK1D,LMNA,MAPK12,PRKAR2B
Serotonin Receptor Signaling	1,28	0,0235	-1,508	ADCY7,FOXO1,GCH1,MAOB,MAPK12,PAK1,PAK4,PLA2G7,PRKAR2B,PTGS1,RHOC
Necroptosis Signaling Pathway	1,24	0,0323	-2,236	MLKL,RIPK3,STAT2,Tomm5,TOMM7
Coronavirus Pathogenesis Pathway	1,24	0,0294	-0,816	MAPK12,MT-RNR1,RIPK3,RPS23,SERPINE1,STAT2
3-phosphoinositide Biosynthesis	1,23	0,0291	-2	DUSP5,DUSP6,PHOSPHO1,PPP1CC,PPP1R3C,PTPRN
Role of Tissue Factor in Cancer	1,22	0,029	-0,816	CFL1,CSF1,F2RL1,LIMK1,MAPK12,RPS6KA5
HIF1α Signaling	1,21	0,0288	-0,816	APEX1,CAMK1D,NOX4,SERPINE1,SLC2A1,SLC2A4
Cholecystokinin/Gastrin-mediated Signaling	1,12	0,0336	-1	CCK,MAPK12,RHOC,SOS2
CXCR4 Signaling	1,12	0,0298	-1,342	ADCY7,MAPK12,PAK1,PAK4,RHOC
Multiple Sclerosis Signaling Pathway	1,1	0,027	0	CLCF1,DUSP6,IRF4,MAPK12,PLP1,TIPARP
Phagosome Formation	1,07	0,0201	-0,535	AP1S1,CFL1,DRD1,F2RL1,ITGA5,LIMK1,MAPK12,PAK1,PAK4,PLA2G7,PTGIR,SCARA5,SOS2,SUCNR1
Gαs Signaling	1,05	0,0317	0	ADCY7,DRD1,PRKAR2B,PTGIR
EIF2 Signaling	1,05	0,0261	-1	MT-RNR1,NOX4,PPP1CC,RPL8,RPS23,SOS2
G-Protein Coupled Receptor Signaling	1,04	0,0199	-0,535	ADCY7,APEX1,DRD1,DUSP6,F2RL1,FOXO1,MAPK12,PAK1,PAK4,PDE3B,PRKAR2B,PTGIR,SOS2,SUCNR1
Tumor Microenvironment Pathway	1,03	0,0279	-1,342	CSF1,FOXO1,ITGA5,SLC2A1,SLC2A4
Superpathway of Inositol Phosphate Compounds	1,02	0,0256	-2	DUSP5,DUSP6,PHOSPHO1,PPP1CC,PPP1R3C,PTPRN
HGF Signaling	0,992	0,0303	-1	ITGA5,MAPK12,PAK1,SOS2
Acute Phase Response Signaling	0,984	0,027	0	CRABP1,MAPK12,SERPINE1,SOCS1,SOS2
Dopamine-DARPP32 Feedback in cAMP Signaling	0,976	0,0269	0,447	ADCY7,DRD1,PPP1CC,PPP1R3C,PRKAR2B
AMPK Signaling	0,967	0,0248	0	CHRNB1,FOXO1,MAPK12,PRKAR2B,SLC2A1,SLC2A4
Actin Cytoskeleton Signaling	0,955	0,0246	-0,816	CFL1,ITGA5,LIMK1,PAK1,PAK4,SOS2
Role of Osteoclasts in Rheumatoid Arthritis Signaling Pathway	0,916	0,0227	-1,89	COL5A3,CSF1,FOXO1,ITGA5,MAPK12,RHOC,SOS2
Role of Chondrocytes in Rheumatoid Arthritis Signaling Pathwa	0,915	0,0284	-2	ITGA5,MAPK12,MLKL,RIPK3
Pathogen Induced Cytokine Storm Signaling Pathway	0,896	0,0216	-2,121	CLCF1,COL5A3,CXCL10,MAPK12,MLKL,RIPK3,SLC2A1,SLC2A4
Adrenomedullin signaling pathway	0,886	0,0251	0	ADCY7,MAPK12,PRKAR2B,SLC39A7,SOS2
Gustation Pathway	0,867	0,0248	0,447	ADCY7,LIPG,PDE3B,PRKAR2B,SLC2A4
Pulmonary Fibrosis Idiopathic Signaling Pathway	0,825	0,0215	0	COL5A3,FOXO1,MAPK12,NOX4,RPS6KA5,SERPINE1,SOS2
IL-8 Signaling	0,817	0,0238	-1	LIMK1,MAPK12,NOX4,RHOC,VASP
IL-10 Signaling	0,816	0,026	-1	BCL3,DDIT4,IL4R,MAPK12
Epithelial Adherens Junction Signaling	0,788	0,0253	-1	CFL1,LIMK1,PAK1,PAK4
Opioid Signaling Pathway	0,757	0,0214	0	ADCY7,CAMK1D,MAPK12,PRKAR2B,RPS6KA5,SOS2
Breast Cancer Regulation by Stathmin1	0,755	0,0185	0,905	ARHGEF9,CAMK1D,DRD1,F2RL1,PAK1,PPP1CC,PPP1R3C,PRKAR2B,PTGIR,SOS2,SUCNR1
Role of NFAT in Cardiac Hypertrophy	0,738	0,0223	-1	ADCY7,CAMK1D,MAPK12,PRKAR2B,SOS2
Thrombin Signaling	0,732	0,0222	-0,447	ADCY7,ARHGEF9,CAMK1D,MAPK12,RHOC
Neurovascular Coupling Signaling Pathway	0,696	0,0216	-0,447	PLA2G7,PRKAR2B,PTGIR,PTGS1,SLC39A7
Orexin Signaling Pathway	0,666	0,021	-0,447	ADCY7,FOXO1,MAPK12,PRKAR2B,SLC2A4
Macrophage Classical Activation Signaling Pathway	0,605	0,0212	-1	CLCF1,CXCL10,SOCS1,STAT2
Synaptogenesis Signaling Pathway	0,605	0,019	0	ADCY7,CFL1,LIMK1,PAK1,PRKAR2B,SOS2
Production of Nitric Oxide and Reactive Oxygen Species in Ma	0,595	0,0209	-1	MAPK12,PPP1CC,PPP1R3C,RHOC
Endothelin-1 Signaling	0,58	0,0206	0	ADCY7,MAPK12,PLA2G7,PTGS1
Adrenergic Receptor Signaling Pathway (Enhanced)	0,552	0,02	1	ADCY7,CLCF1,MAOB,PRKAR2B
ID1 Signaling Pathway	0,547	0,0199	-1	BCL3,CHRNB1,MAPK12,RHOC
ILK Signaling	0,547	0,0199	-1	CFL1,MAPK12,RHOC,RPS6KA5
Colorectal Cancer Metastasis Signaling	0,525	0,0185	-0,447	ADCY7,MAPK12,PRKAR2B,RHOC,SOS2
Cardiac Hypertrophy Signaling (Enhanced)	0,518	0,0166	-0,707	ADCY7,APEX1,CLCF1,IL4R,ITGA5,MAPK12,PDE3B,PRKAR2B,RPS6KA5
Activin Inhibin Signaling Pathway	0,479	0,0184	-2	COL5A3,LIMK1,MAPK12,SERPINE1
Sertoli Cell-Sertoli Cell Junction Signaling	0,387	0,0165	-2	MAPK12,PAK1,PAK4,TIMP1
Wound Healing Signaling Pathway	0,359	0,0159	-1	CLCF1,COL5A3,MAPK12,SOS2
Cardiac Hypertrophy Signaling	0,334	0,0153	-1	ADCY7,MAPK12,PRKAR2B,RHOC
Oxytocin Signaling Pathway	0,281	0,0142	0	MAPK12,PRKAR2B,SLC39A7,SOS2
CREB Signaling in Neurons	0	0,0132	0	ADCY7,DRD1,F2RL1,POLR2L,PRKAR2B,PTGIR,SOS2,SUCNR1
Glutaminergic Receptor Signaling Pathway (Enhanced)	0	0,0123	0	ADCY7,MAPK12,PLA2G7,PRKAR2B
Myelination Signaling Pathway	0	0,0122	1	PLP1,PRKAR2B,SLC2A1,SOS2
S100 Family Signaling Pathway	0	0,0117	-0,333	BCL3,DRD1,F2RL1,MAPK12,NOX4,PRKAR2B,PTGIR,S100A6,SUCNR1
FAK Signaling	0	0,0115	-1,155	COL5A3,DRD1,F2RL1,IL4R,ITGA5,MAPK12,PAK1,PAK4,PTGIR,SOCS1,SOS2,SUCNR1
IL-4 Signaling	0	0,0104	0	COL5A3,IL4R,IRF4,MAPK12,SOCS1,SOS2
CDC42 Signaling	0	0,0104	-2,449	CFL1,ITGA5,LIMK1,MAPK12,PAK1,PAK4
TEC Kinase Signaling	0	0,0104	-2,449	ITGA5,MAPK12,PAK1,PAK4,RHOC,STAT2
Systemic Lupus Erythematosus in B Cell Signaling Pathway	0	0,00828	-1,633	CLCF1,FOXO1,IFIT2,IFIT3,SOS2,STAT2
T Cell Receptor Signaling	0	0,00649	1	DUSP5,DUSP6,MAPK12,SOS2
B Cell Receptor Signaling	0	0,0063	-1	CFL1,FOXO1,MAPK12,SOS2
Phospholipase C Signaling	0	0,00446	0	ADCY7,ARHGEF9,ITGA5,RHOC,SOS2

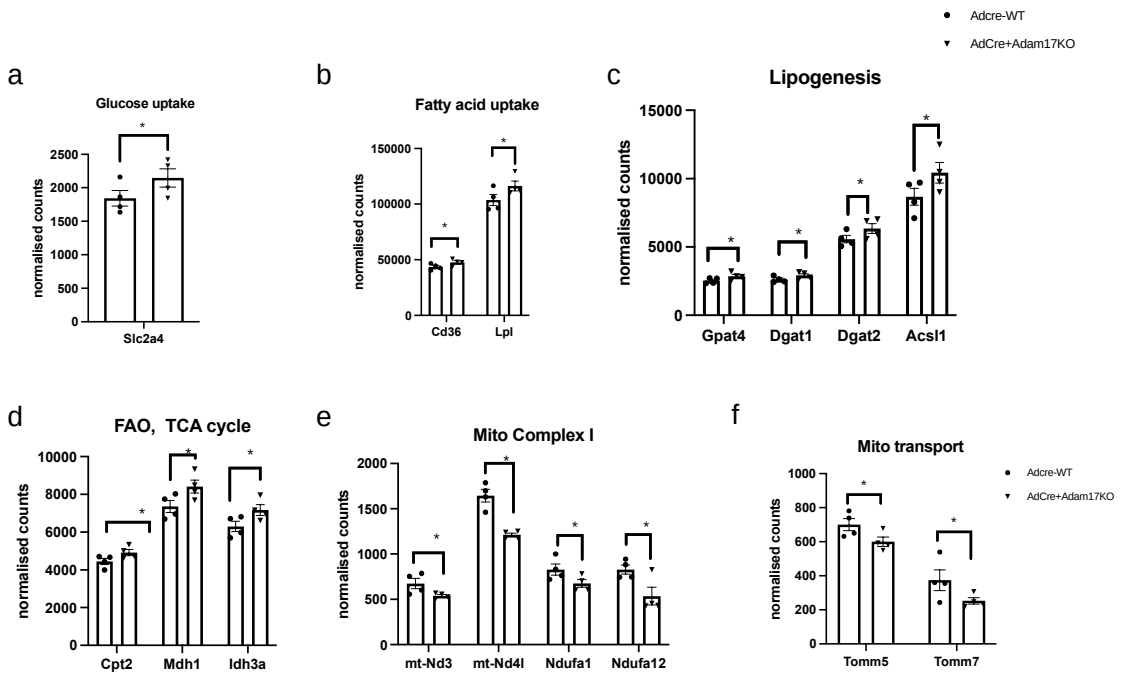

Figure 3: Differentially expressed genes in white adipocytes from mice with conditional deletion of ADAM17 in the adipocytes and control mice.

RNA sequencing was performed on total RNA isolated from inguinal white adipocytes, in vitro differentiated from SVF cells isolated from to Adip^{Cre-}WT and Adip^{Cre+}Adam17KO male mice (n=4 per genotype). Data shown are mean ± SEM of normalized counts of depicted genes. Statistics is a student's t-test, p-value is (*) < 0.05.

Untargeted proteomics on total cell lysates data also revealed the 515 proteins were differentially expression between Adip^{Cre+}Adam17KO compared to Adip^{Cre-}WT white adipocytes, with 170 being upregulated and 346 being downregulated. Like the results acquired by transcriptomics analysis, untargeted proteomics revealed that mitochondrial complex I and other components of the oxidative phosphorylation were downregulated in the Adip^{Cre+}Adam17KO adipocytes compared to control white adipocytes (Table 4 and Fig. 4).

Overall, these unbiased approaches of investigating the effects of ADAM17 deletion in white adipocytes suggested that ADAM17 deletion affected the mitochondrial components (Table 4) and multiple metabolic pathways in the adipocyte.

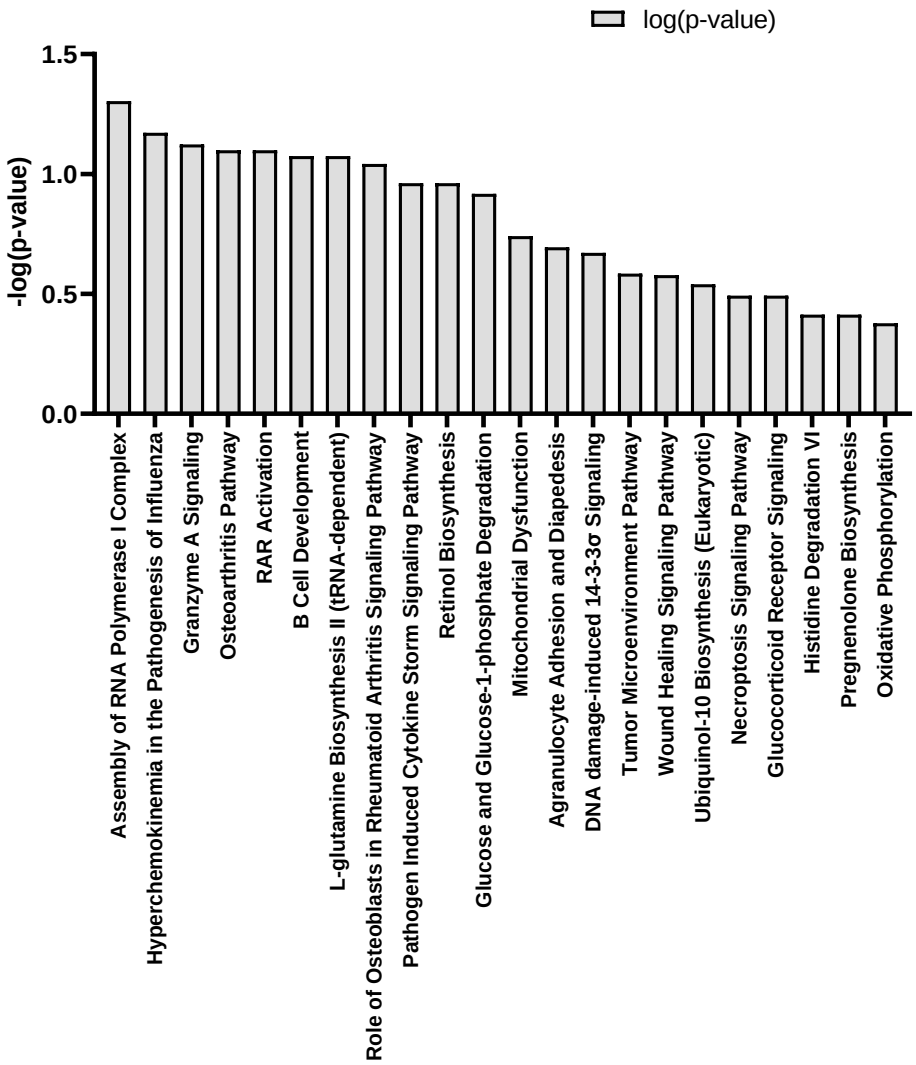

Figure 4: Differentially expressed Metabolic Pathways calculated based on total proteomics quantification of Ad^{Cre+}Adam17KO vs Ad^{Cre-}WT iWAT (SVF derived) adipocytes ranked according to –log (p-value). Total cell lysates were used for the untargeted proteomics. Generated with Ingenuity Pathway analysis software.

Table 4: List of proteins involved in mitochondrial function and biogenesis, as quantified with untargeted proteomics, run on total cell lysates of Adip^{Cre+}Adam17KO vs Adip^{Cre-}WT iWAT (SVF derived) adipocytes.

Protein FDR Confidence Combined	Accession	Description	Gene Symbol	Number of PSMs	Number of Pepti-des	Number of Unique Peptides	Abundance Ratio ADAM17KO vs WT	Abundance Ra-tio P-Value ADAM17KOvs WT	Abundance Ratio Adj P-Value ADAM17KO vs WT
High	Q3UIU2	NADH dehydrogenase [ubiquinone] 1 beta subcomplex subunit 6	Ndufb6	52	4	4	0,78	0,0436	0,4044
High	Q99LY9	NADH dehydrogenase [ubiquinone] iron-sulfur protein 5	Ndufs5	42	6	6	0,76	0,0325	0,3386
High	Q9CZP5	Mitochondrial chaperone BCS1	Bcs1l	71	16	16	0,74	0,0261	0,3034
High	Q9CQH3	NADH dehydrogenase [ubiquinone] 1 beta subcomplex subunit 5, mitochondrial	Ndufb5	46	5	5	0,74	0,0303	0,3245
High	P03893	NADH-ubiquinone oxidoreductase chain 2	mt-Nd2	17	3	3	0,74	0,0379	0,3700
High	Q9D3D9	ATP synthase subunit delta, mitochondrial	Atp5f1d	28	7	6	0,73	0,0126	0,1958
High	Q9CPP6	NADH dehydrogenase [ubiquinone] 1 alpha subcomplex subunit 5	Ndufa5	61	7	7	0,73	0,0226	0,2795
High	Q9D1H6	NADH dehydrogenase [ubiquinone] 1 alpha subcomplex assembly factor 4	Ndufaf4	34	5	5	0,73	0,0365	0,3656
High	Q9CQZ6	NADH dehydrogenase [ubiquinone] 1 beta subcomplex subunit 3	Ndufb3	36	4	4	0,73	0,0119	0,1893
High	Q4FZG9	NADH dehydrogenase [ubiquinone] 1 alpha subcomplex subunit 4-like 2	Ndufa4l2	20	4	4	0,72	0,0126	0,1958
High	Q9CQV1	Mitochondrial import inner membrane translocase subunit TIM16	Pam16	22	5	5	0,72	0,0234	0,2854
High	Q9D173	Mitochondrial import receptor subunit TOM7 homolog	Tomm7	5	1	1	0,72	0,0279	0,3133
High	Q9CQZ5	NADH dehydrogenase [ubiquinone] 1 alpha subcomplex subunit 6	Ndufa6	47	7	7	0,72	0,0243	0,2908
High	Q9Z2Z6	Mitochondrial carnitine/acylcarnitine carrier protein	Slc25a20	126	19	19	0,72	0,0449	0,4107
High	Q9QYA2	Mitochondrial import receptor subunit TOM40 homolog	Tomm40	113	13	13	0,72	0,0451	0,4107
High	Q9QZD8	Mitochondrial dicarboxylate carrier OS=Mus musculus	Slc25a10	181	16	16	0,72	0,0437	0,4044
High	O35683	NADH dehydrogenase [ubiquinone] 1 alpha subcomplex subunit 1	Ndufa1	2	1	1	0,71	0,0403	0,3840
High	A2AIL4	NADH dehydrogenase (ubiquinone) complex I, assembly factor 6	Ndufaf6	**6**	**2**	**2**	0,71	0,0484	0,4283
High	Q59J78	NADH dehydrogenase [ubiquinone] 1 alpha subcomplex assembly factor 2	Ndufaf2	**50**	**11**	**11**	0,71	0,0194	0,2508

High	P03888	NADH-ubiquinone oxidoreductase chain 1	Mtnd1	23	4	4	0,71	0,0269	0,3086
High	Q8CCM6	Mitochondrial import inner membrane translocase subunit Tim21	Timm21	27	7	7	0,71	0,0341	0,3504
High	Q9CQQ7	ATP synthase F(0) complex subunit B1, mitochondrial	Atp5pb	212	19	18	0,70	0,0327	0,3400
High	P56135	ATP synthase subunit f, mitochondrial OS=Mus musculus	Atp5mf	112	3	3	0,70	0,0237	0,2858
High	Q9CR62	Mitochondrial 2-oxoglutarate/malate carrier protein	Slc25a11	130	17	17	0,70	0,0297	0,3224
High	Q9CQ75	NADH dehydrogenase [ubiquinone] 1 alpha subcomplex subunit 2	Ndufa2	27	4	4	0,70	0,0082	0,1449
High	Q9CQ54	NADH dehydrogenase [ubiquinone] 1 subunit C2	Ndufc2	35	6	6	0,70	0,0116	0,1877
High	Q8K3J1	NADH dehydrogenase [ubiquinone] iron-sulfur protein 8, mitochondrial	Ndufs8	81	11	11	0,69	0,0075	0,1364
High	Q791V5	Mitochondrial carrier homolog 2	Mtch2	148	13	13	0,69	0,0270	0,3094
High	P03930	ATP synthase protein 8	Mtatp8	29	3	3	0,69	0,0188	0,2477
High	Q9CPQ8	ATP synthase subunit g, mitochondrial	Atp5mg	36	2	2	0,69	0,0101	0,1693
High	Q06185	ATP synthase subunit e, mitochondrial	Atp5me	34	4	4	0,68	0,0094	0,1607
High	Q9D6M3	Mitochondrial glutamate carrier 1	Slc25a22	69	14	14	0,68	0,0071	0,1314
High	Q9CPU2	NADH dehydrogenase [ubiquinone] 1 beta subcomplex subunit 2, mitochondrial	Ndufb2	10	2	2	0,67	0,0097	0,1639
High	Q9WV96	Mitochondrial import inner membrane translocase subunit Tim10 B	Timm10b	3	2	2	0,67	0,0175	0,2355
High	Q9CRB8	Mitochondrial fission process protein 1	Mtfp1	7	5	5	0,65	0,0074	0,1354
High	Q9Z0V8	Mitochondrial import inner membrane translocase subunit Tim17-A	Timm17a	28	5	5	0,65	0,0038	0,0839
High	P56382	ATP synthase subunit epsilon, mitochondrial	Atp5f1e	19	2	2	0,65	0,0022	0,0550
High	P0DN34	NADH dehydrogenase [ubiquinone] 1 beta subcomplex subunit 1	Ndufb1	19	4	4	0,64	0,0005	0,0156
High	Q9CQV7	Mitochondrial import inner membrane translocase subunit TIM14	Dnajc19	30	7	6	0,64	0,0037	0,0820
High	P62075	Mitochondrial import inner membrane translocase subunit Tim13	Timm13	22	5	5	0,63	0,0023	0,0565
High	Q8VEA4	Mitochondrial intermembrane space import and assembly protein 40	Chchd4	12	2	2	0,63	0,0095	0,1617
High	Q9CQC7	NADH dehydrogenase [ubiquinone] 1 beta subcomplex subunit 4	Ndufb4	35	6	6	0,62	0,0009	0,0266
High	Q9CXD6	Mitochondrial calcium uniporter regulator 1	Mcur1	30	9	8	0,61	0,0002	0,0066
High	B1AXP6	Mitochondrial import receptor subunit TOM5 homolog	Tomm5	19	5	5	0,60	0,0002	0,0056

High	Q9CQN3	Mitochondrial import receptor subunit TOM6 homolog	Tomm6	20	2	2	0,59	0,0008	0,0235
High	Q9DCX2	ATP synthase subunit d, mitochondrial	Atp5pd	107	13	13	0,58	0,0012	0,0338
High	Q78IK2	ATP synthase membrane subunit DAPIT, mitochondrial	Atp5mk	14	1	1	0,58	0,0000	0,0011
High	P12242	Mitochondrial brown fat uncoupling protein 1	Ucp1	39	10	10	0,56	0,0000	0,0003
High	Q9WVA2	Mitochondrial import inner membrane translocase subunit Tim8 A	Timm8a1	2	2	2	0,56	0,0004	0,0134
High	Q9WV98	Mitochondrial import inner membrane translocase subunit Tim9	Timm9	16	6	6	0,54	0,0002	0,0076
High	P97450	ATP synthase-coupling factor 6, mitochondrial OS=Mus musculus	Atp5pf	11	3	3	0,51	0,0001	0,0031

3.2 Differentially expressed membrane proteins in the white adipocytes from Adip^{Cre+}Adam17KO compared to Adip^{Cre-}WT mice.

We examined the data for differentially expressed membrane bound proteins and receptors, which have been previously identified to be targets of ADAM17. Amongst them, we found angiotensin-converting enzyme (Ace), low density lipo-protein receptor (LDLr), very low-density lipoprotein receptor (VLDLr), SORTILIN, just to mention a few (Table 5).

In addition, we also looked for differentially expressed membrane proteins, which have not been previously identified as targets of ADAM17. Amongst them, we found the beta 3 Adrenergic receptor (ADRB3) (Table 5).

Table 5 : List of known ADAM17 protein substrates, which were differentially expressed between Adip^{Cre+}Adam17KO and Adip^{Cre-}WT iWAT (SVF derived) adipocytes.

Description	Gene Symbol	Function	Abundance Ratio KO vs. WT	Abundance Ratio P-Value KO vs. WT	Abundance Ratio Adj P-Value KO vs. WT
Vascular endothelial growth factor A	Vegfa	Growth factor	0,472	0,002	0,042
Angiotensin-converting enzyme	Ace	Enzyme	1,618	0,005	0,107
Sortilin	Sort1	Cellular transport	0,731	0,012	0,192
Beta-3 adrenergic receptor	Adrb3	Adrenergic function	0,688	0,040	0,384
Vascular endothelial growth factor D	Vegfd	Growth factor	1,481	0,073	0,540
Scavenger receptor cysteine-rich type 1 protein M130	Cd163	Signalling receptor	1,536	0,081	0,566
Amyloid-like protein 2	Aplp2	neurite cell growth and migration	0,829	0,189	0,790
Transforming growth factor beta receptor type 3	Tgfbr3	Cell-to-cell communication, cytokine receptor	1,279	0,217	0,826
Neural cell adhesion molecule 1	Ncam1	Cell adhesion molecule	0,847	0,223	0,832
Interleukin-1 receptor type 1	Il1r1	Cell-to-cell communication, cytokine receptor	0,845	0,248	0,853
Very low-density lipoprotein receptor	Vldlr	Cellular transport	0,800	0,274	0,874
CD166 antigen OS=Mus musculus	Alcam	Cell adhesion molecule	0,866	0,301	0,897
CD44 antigen	Cd44	Cell adhesion molecule	1,220	0,312	0,899
Inactive tyrosine-protein kinase 7	Ptk7	Signalling receptor	0,897	0,400	0,945
Neuropilin-1	Nrp1	signalling receptor	1,145	0,573	0,976
Vasorin	Vasn	Glycoprotein	1,127	0,659	0,991
Cation-independent mannose-6-phosphate receptor	Igf2r	Cellular transport	0,969	0,694	0,991
Major prion protein	Prnp	neuronal development and synaptic plasticity	0,995	0,832	0,992
Prolow-density lipoprotein receptor-related protein 1	Lrp1	Cellular transport	0,987	0,907	0,992

3.3 Higher protein levels of ADRB3 in Adip^{Cre+}Adam17KO and Adip^{Cre-}WT control brown and white adipocytes.

ADAM17 has been previously described to cleave ADRB1 (Zhu & Steinberg, 2021). ADRB3 is a homologue of ADRB1 and out of the three isoforms (ADRB1 ADRB2, ADRB3) is mostly expressed in white and brown mouse adipocytes (Park *et al*., 2017). We examined closer the regulation of ADRB3 in mouse adipocytes from Adip^{Cre+}Adam17KO vs Adip^{Cre-}WT mice. By using Western blot analysis against ADRB3 in total protein cell lysates from brown and white adipocytes from Adip^{Cre+}Adam17KO vs Adip^{Cre-}WT mice, we observed that ADRB3 protein levels were higher in Adip^{Cre+}Adam17KO brown and white adipocyte, although white adipocytes showed higher, variation of this effect (Fig. 5a, 5b). After 2 hours incubation with a specific ADRB3 agonist, CL 316,243, ADRB3 protein levels remained high in the Adip^{Cre+}Adam17KO compared to WT control brown adipocytes (Fig. 5a). Despite being higher at baseline ADRB3, protein levels in white Adip^{Cre+}Adam17KO decreased to similar levels to that of the WT control white adipocytes, after CL 316,243 treatment (Fig. 5b). Typically, incubation of white adipocytes with CL 316,243 leads to a decrease of ADRB3 protein levels due to receptor internalization/degradation (Valentine *et al*., 2022). Of note we found no differences in the levels of ADBR2 receptor, also expressed in adipocytes, suggesting a specific effect of ADAM17 on ADRB3.

These findings led us to hypothesize that ADAM17 deletion may be altering the response of brown and white adipocytes to CL 316,243 agonist. One robust readout of response to CL 316,243 is lipolysis (MacPherson *et al*., 2014). Therefore, we quantified the NEFA released to the media from Adip^{Cre+}Adam17KO and Adip^{Cre-}WT, brown and white adipocytes, 2 h after CL 316,243 stimulation. In media containing 2% BSA, used to capture released NEFA, we observed no differences in NEFA levels from Adip^{Cre+}Adam17KO and Adip^{Cre-}WT adipocytes treated 2 h with CL 316,243 (Fig. 5c, 5d).

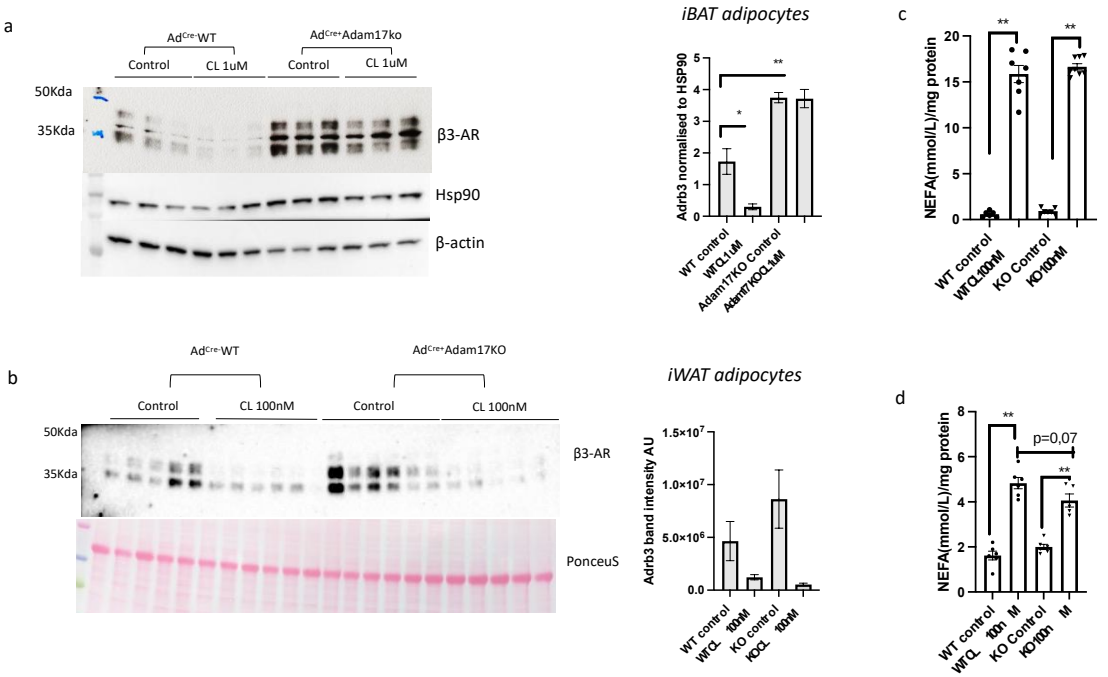

Figure 5: Adrb3 protein levels and lipolysis response in brown and white adipocytes from Adip^{Cre+}Adam17KO and Adip^{Cre-}WT mice treated with CL 316,243 agonist.

Brown and white adipose tissue were collected. Stromal vascular fraction was isolated and differentiated into mature adipocytes. (a-b) Western blot analysis for beta 3 adrenergic receptor (adrb3) in total protein cell lysates from brown and white adipocytes from Adip^{Cre+}Adam17KO vs Adip^{Cre-}WT mice with and without CL 316,243 treatments. Heat shock protein 90 (HSP90) was used as loading control. (a) Ad^{Cre-}WT (control treatment n=3, CL 316,243 treatment n=3) and Adip^{Cre+}Adam17KO (control treatment n=3, CL 316,243 treatment n=3) (b) Adip^{Cre-}WT (control treatment n=5, CL 316,243 treatment n=6) and Adip^{Cre+}Adam17KO (control treatment n=6, CL 316,243 treatment n=5). (c - d) Nefa measurement in supernatant from (c) brown and (d) white adipocytes from Adip^{Cre+}Adam17KO vs Adip^{Cre-}WT mice before and after CL 316,243 treatments. Data are shown as mean± SEM. * is p-value <0.05 calculated by a student's t-test.

3.4 ADAM17 is differentially regulated by cold mimicking and fasting mimicking stimuli.

We examined the regulation of ADAM17 in white adipocytes by cAMP and Beta-adrenergic receptor agonists. We found that ADAM17 mRNA levels decreased by Forskolin but did not respond to CL 316,243 (Adrb3 agonist), Formoterol (Adrb2 agonist) or Dobutamine (Adrb1agonist) (Fig. 6a). In response to CL 316,243, Formoterol and Forskolin Adrb3 mRNA decreased (Fig. 6b). This was

expected since increased levels of cAMP have been previously shown to down-regulate Adrb3 mRNA and protein (Michel *et al*., 2020). We observed that Adrb2 mRNA increased in response to CL 316,243 and Adrb1 was not expressed in white adipocytes and thus dobutamine did not generate any biological effects (Fig. 6c). Therefore, also confirming that the applied dose of the different Beta AR ligands (100 nM) and duration of treatment (4 h) was enough to produce biological effects on the adipocytes.

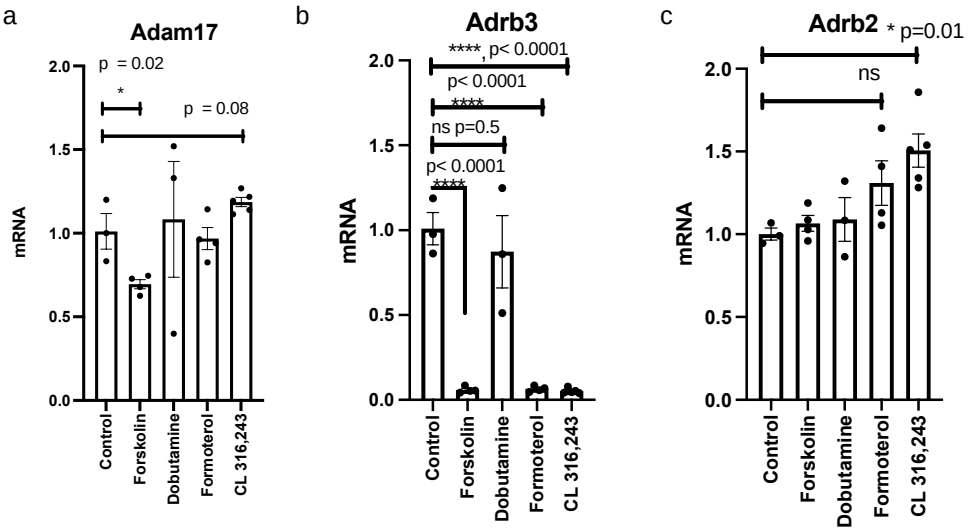

Figure 6: Regulation of ADAM17 by beta-adrenergic receptor agonists and Forskolin.

Q-PCR quantification of mRNA of depicted genes is shown. Primary mouse adipocytes were isolated from wild type C57BL/6 mice. Primary adipocytes were stimulated with Forskolin, CL 316,243 (Adrb3 agonist), Formoterol (Adrb2 agonist) or Dobutamine (Adrb1agonist) for 4 hours (n=3 per treatment group). Data are shown as mean± SEM. * is p-value <0.05 calculated by a student's t-test.

Forskolin increases the intracellular levels of cAMP by activating adenylate cyclase (AC). Although both forskolin and beta-adrenergic receptor agonists lead to increase cAMP levels, ADAM17 mRNA responded differently to those drugs. To understand whether ADAM17 mRNA also responded to lack of nutrients, which will stimulate lipolysis in adipocytes mimicking fasting conditions, we exposed white adipocytes to low glucose media for 6 hours. We saw that ADAM17 mRNA levels were downregulated in low glucose compared to high glucose media conditions (Fig. 7a, 7b). To clarify whether ADAM17 levels in adipocytes are

regulated in a physiological context by lipolysis, which is the downstream result of increased cAMP levels in the adipocytes, we examined the regulation of ADAM17 by fasting. We found that ADAM17 mRNA decreased upon prolonged fasting (24 h) in gonadal fat, subcutaneous fat and liver and returned to prior fasting levels during refeeding, following 24 h fasting (Fig. 7c,7d,7e.). ADAM17 mRNA levels were not affected by fasting or refeeding in the BAT (Fig. 7f). Therefore, ADAM17 is differentially regulated in white adipocytes by adrenergic stimulation and lack of nutrients induced lipolysis.

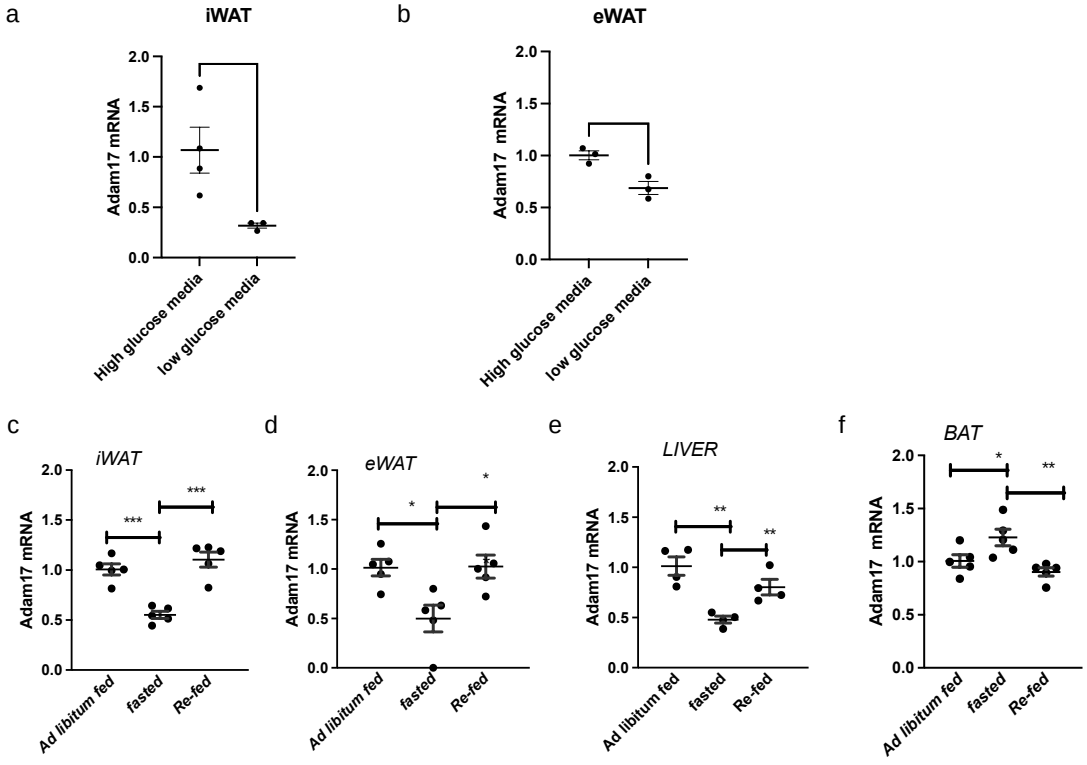

Figure 7: **Adipose tissue ADAM17 is decreased by fasting and increased by refeeding.** Relative RT-qPCR analysis of mRNA levels for ADAM17 in primary mouse adipocytes, normalized for HRPT in (a) iWAT and (b) eWAT Relative mRNA expression of ADAM17 measured in (c) inguinal white adipose tissue (iWAT), (d) epididymal white adipose tissue (eWAT), (e) liver and (f) brown adipose tissue (BAT) in wild type mice after 24 hours of fasting and 4 hours of refeeding. Data are shown as mean± SEM. * is p-value <0.05 calculated by a student's t-test.

3.5 ADAM17 is expressed in a subpopulation of (white) adipocytes in inverse correlation to the Adrb3.

Utilizing existing published studies on single nuclei and single cell RNA seq data we investigated the association of ADAM17 expression levels in adipocytes with other gene markers, adipocyte clusters, adipose tissue depots, diet, and sex. To that end, we used the datasets from publicly available single cell single nuclei RNAseq data. The datasets we examined where, **a) on white fat depots** from mice and humans. We examined the datasets from Sarvari and colleagues (Sárvári *et al*., 2021), on single nuclei data from the eWAT of male mice on chow fed diet . Data set from Emont and friends (Emont *et al*., 2022), where single cell and single nuclei RNA seq data have been generated for visceral fat (eWAT in mice) and subcutaneous fat (iWAT in mice) from mice and humans, lean and obese were also analyzed. b) **On brown adipose tissue**: For brown adipose tissue we examined the datasets from Sun and colleagues (Sun *et al*., 2020), where single nuclei data from human brown adipose tissue and single nuclei data from mouse brown adipocytes are available, at the room temperature and after cold exposure.

Overall, the single nuclei and single cell data revealed that ADAM17 is expressed in adipose tissue of both mice and humans (Fig. 8), more in males than females' white adipose tissues (Fig. 8a, 8b) and well expressed in epididymal and inguinal fat of mice (Fig. 8c) and subcutaneous adipose tissue, but not omental fat tissue in humans (Fig. 8d). We observed that ADAM17 was present in adipocytes in similar levels compared to other cell types in both mice and humans. In addition, only 30-40% of all cell types, including adipocytes were positive for ADAM17 and the adipocytes were the second population after the immune cells (mainly monocytes and macrophages) with the highest expression levels of ADAM17 in the white fat of mice and humans (Fig. 8e, 8f). We also found that ADAM17 was expressed in brown fat of mice and humans, but to a lesser extent in adipocytes compared to other cell types (Fig. 9a, 9b).

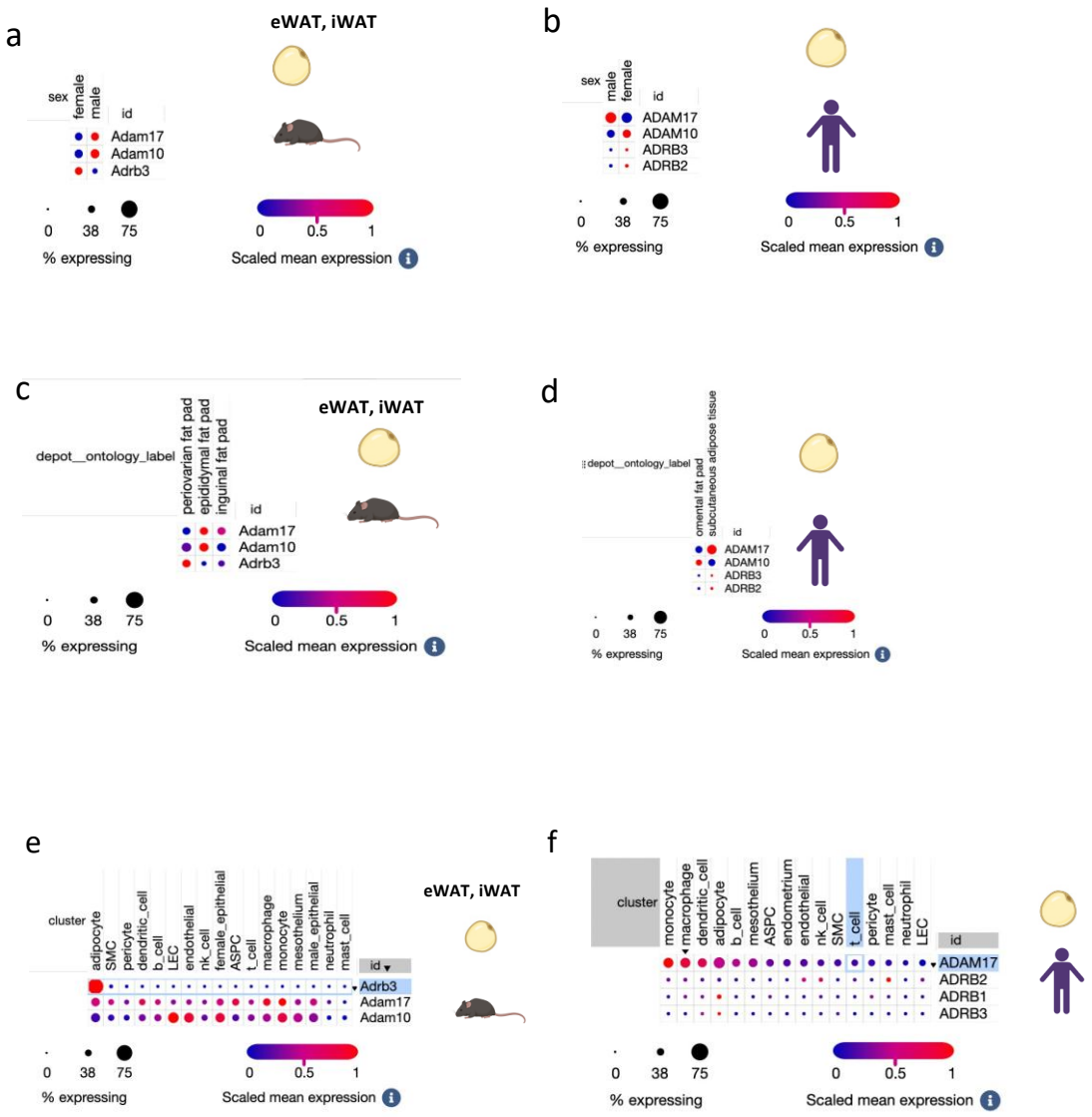

Figure 8: mRNA expression levels and percentage of ADAM17 expressing single nuclei and single cells of white fat depots.

(a) iWAT, eWAT of male and female mice, (b) white fat depots of male and female humans, (c) periovarian, epididymal, inguinal fat depots of male mice, (d) omental and subcutaneous adipose tissue of humans. Also, different cell types of (e) eWAT, iWAT of mice and (f) white fat depots in human. Dataset is derived from (Emont *et al*., 2022) and visualization was done using the Single Cell Portal (singlecell.broadinstitute.org).

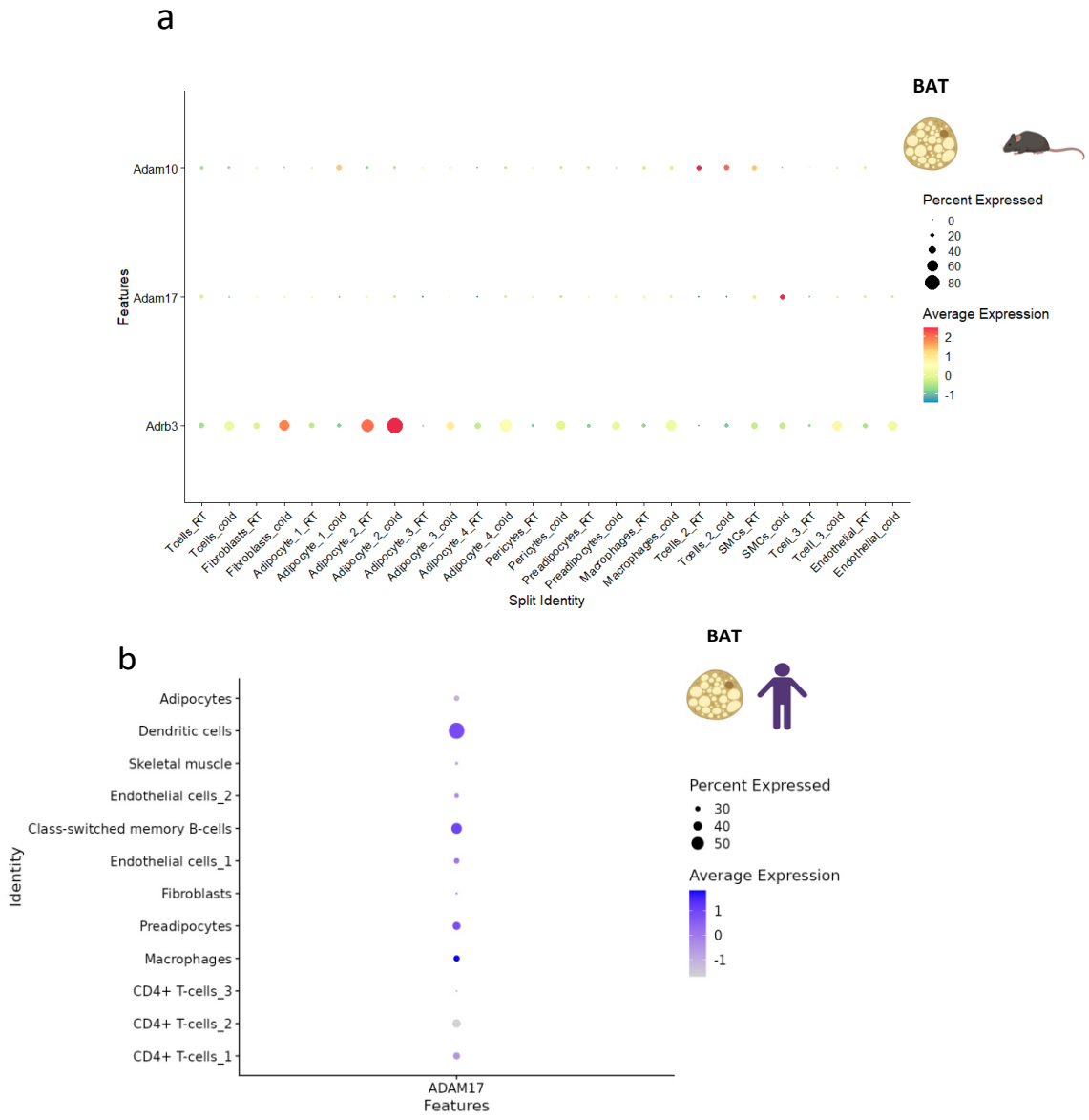

Figure 9: mRNA expression levels and percentage of ADAM17 in single nuclei and single cells of brown adipose tissue.

(a) mouse brown adipose tissue, under cold (8 °C) and RT conditions, (b) human brown adipose tissue. (a) is from our unpublished data, (b) is from (Sun *et al*., 2020).

Recently several adipocyte populations have been defined in white and brown adipose tissue. We examined whether ADAM17 is enriched in a particular subpopulation of white or brown adipocytes in mice and humans. Sárvári and colleagues defined 3 adipocytes subclusters in the mouse eWAT, the lipid-scavenging adipocytes (LSA), the lipogenic adipocytes (LGA) and stressed lipid-scavenging adipocytes (SLSA) (Sárvári *et al*., 2021). We found low expression of ADAM17 in all three adipocyte subtypes, in the dataset by (Sárvári *et al*.,

2021)(Fig. 10a). Emont and colleagues (Emont *et al*., 2022) defined 6 adipocyte subclusters in mouse eWAT and iWAT (mAd1, mAd2, mAd3, mAd4, mAd5, mAd6). We observed that ADAM17 was in the adipocytes subclusters mAd4, mAd5, mAd6, (mAd5>mAd4>mAd6>mAd2>mAd1>mAd3), where also its homologues Adam10 was expressed at similar levels (Fig. 10b). We noticed that ADAM17 but not ADAM10 was highly expressed in mAd2 (Fig. 10b). Of note, Adrb3 expression levels were reversely associated with the expression levels of ADAM17 in those adipocyte subpopulations (Fig. 10b). Emont and colleagues described subpopulations mAd4-mAd6 as HFD associated clusters, as they were particularly enriched in mice fed HFD and were enriched with genes mapping on metabolic pathways, such as HIF-1 signaling, acting cytoskeleton and NF-kB signaling, consistent with the presence of hypoxia, cytoskeleton remodeling and inflammation associated with HFD induced changes in the white adipose tissue. The different mouse adipocytes clusters showed similar distribution in subcutaneous (Inguinal WAT) and gonadal WAT.

The study also included human white adipose tissue and defined 7 adipocytes subclusters (hAd1-hAd7) (Emont *et al*., 2022). We observed that ADAM17 expression in human adipocytes subtypes followed the following expression hAd4 > hAd1 > hAd5 > hAd7 > hAd3 > hAd6 > hAd2 (Fig. 10c). ADAM17 was present in 66% of hAd4 cluster, where its expression levels were the highest compared to the other cluster (Fig.10c). hAd4 and hAd1 where ADAM17 showed highest expression are localized mainly in human subcutaneous adipose tissue, whereas hAd2, hAd6, where ADAM17 was close to absent are localized in the human visceral adipose tissue. Thus, ADAM17 positive cells are most likely present in human subcutaneous adipose tissue. We observed an inverse association between the human ADAM17 and human Adrb1 expression in human adipocytes, whereas there was no clear correlation of ADAM17 expression with Adrb2 and Adrb3 in human adipocytes subtypes (Fig. 10c).

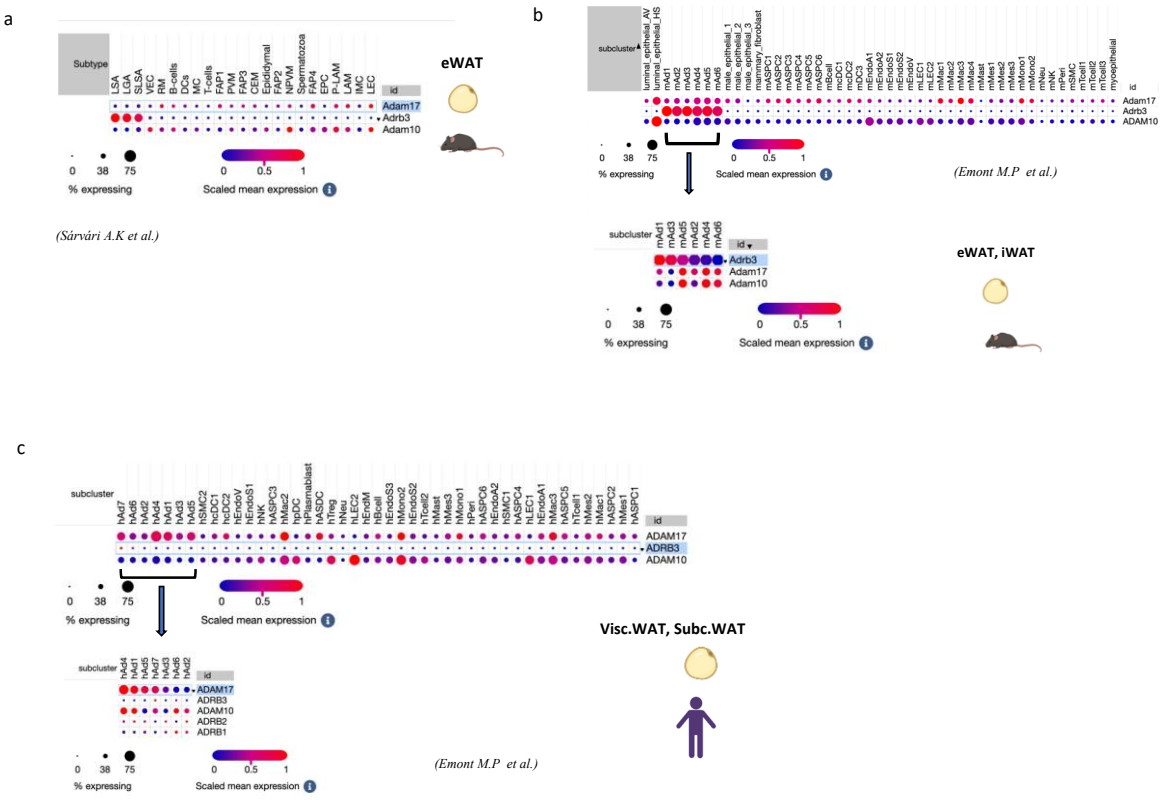

Figure 10: ADAM17 mRNA expression in mouse and human white adipocytes subclusters. Dot plot expression comparison of ADAM17, Adrb3, and Adam10 measured at single cell level in (a) different cells from mouse eWAT. Datasets derived from Sárvári A.K *et al*., (b) different cell types (adipocytes highlighted too as a separate comparison) from mouse eWAT and iWAT, (c) different types (adipocytes highlighted too as a separate comparison) from human visceral WAT and subcutaneous WAT. In (b) and (c) data derived from (Emont *et al*., 2022).

We wondered if there were specific adipogenic progenitors that would express differential levels of ADAM17 and could account for adipocytes with corresponding expression levels of ADAM17 and potentially differential expression and signaling of the Adrb3 receptor. To that end, we sorted mouse primary SVF from inguinal white fat, based on the expression levels of the surface bound ADAM17 after excluding endothelial (marked by Cd31) and immune cells (marked by Cd45), sorting out Cd45-, Cd31-, ADAM17+ SVF cells (Fig. 11a). Both subpopulations differentiated into mature adipocytes and showed different transcriptional signature. We checked for Adrb3 expression levels, and we found that ADAM17 high adipocytes had remarkably lower levels of Adrb3 mRNA, compared to

ADAM17 low adipocytes (Fig. 11b), which is in accordance with the publicly available single cell data (see above). In addition, ADAM17 high adipocytes showed lower levels of Cpt2, Dgat2, Lipe, but higher levels of Cpt1b and Mvd compared to ADAM17 low adipocytes (Fig.11b). In summary ADAM17 is expressed in a subpopulation of white adipocytes and its expression levels inversely correlate with those of Adrb3.

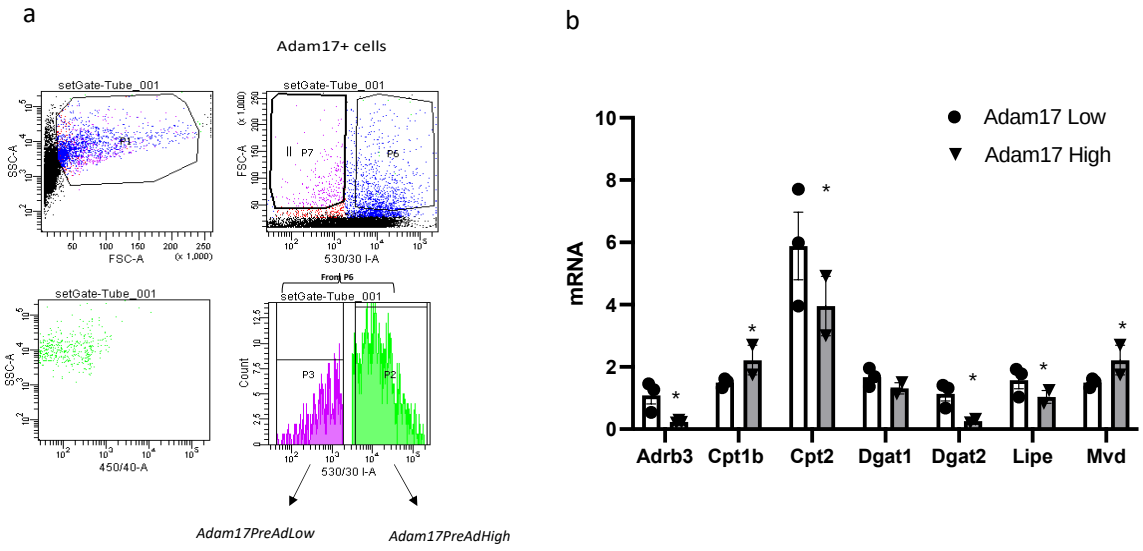

Figure 11: Adipocytes derived from sorted ADAM17 high and low expressing preadipocytes have a different transcriptional signature.

(a) Scatterplot of mouse iWAT stromal vascular fraction (SVF) stained for ADAM17 extracellular domain. P7 represents background staining; P6 represents positive staining, for ADAM17. Out of P6, we selected population P3 as preadipocytes expressing low levels of ADAM17 and P2 as preadipocytes expressing high levels of ADAM17. (b) QPCR quantification of indicated genes in adipocytes differentiated from sorted preadipocytes with low expression of ADAM17 (ADAM17 Low) or high expression of ADAM17 (ADAM17 High). Data are shown as mean± SEM. * is p-value <0.05 calculated by a student's t-test.

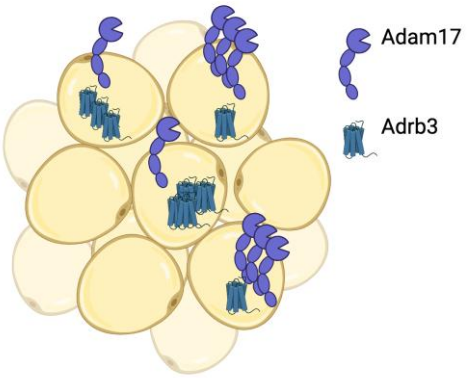

Figure 12: ADAM17 is expressed in a subpopulation of adipocytes and with different levels of expression.

ADAM17 mRNA levels at single cell levels inversely correlate to Adrb3 mRNA levels. ADAM17 is more abundant in white iWAT than iBAT adipose tissue.

3.6 Generation of a mouse model of adipocyte specific deletion of ADAM17 on a clean C57BL6J genetic background

To be able to assess the phenotypic impact of ADAM17 adipocyte deletion on ADRB3 signaling in vivo, we generated a mouse model with conditional adiponectinCre driven deletion of ADAM17 in adipocytes. For that purpose, we used a previously published Cre-LoxP system (Kim *et al*., 2018). Mice with AdiponectinCre expression, on a C57BL6J genetic background were crossed with ADAM17flox/flox expressing mice (with flox sites spanning exon 2 of ADAM17), which have been backcrossed to pure C57BL6J WT mice for 6 generations. After sequencing for genetic background specific SNPs, we have confirmed that AdiponectinCre^{+} x ADAM17flox/flox line we generated was on a pure C57BL6J background (Table 7).

The AdiponectinCre^{+} x ADAM17flox/flox (*Adip^{Cre+}ADAM17KO*) and control group AdiponectinCre^{-} x ADAM17 flox/flox (*Adip^{Cre-}*WT) mice were born at normal Mendelian ratios; a typical litter size was 6-8 mice with 45-50% males and females. All *Adip^{Cre+}ADAM17KO* mice were viable, and we did not observe any abnormal behavioral (motility, barbering) or developmental defects (mouse length, body composition, organ size) compared to *Adip^{Cre-}ADAM17f/f* control mice.

3.7 Effectiveness of ADAM17 deletion in adipose tissues

The Flox system targets the exon2 of ADAM17 (Fig.13a). According to in situ ORF prediction (Fig.13a) and previously published data from the global deletion of exon2 ADAM17 flox targeting (Gelling *et al*., 2008), deletion on exon 2 brings the transcription of the ADAM17 gene out of frame resulting to an absence of a stop codon (Fig. 13b) . Due to the wide expression of ADAM17 in epithelial, mesothelial cells, immune cells, as well as the higher expression levels of ADAM17 levels in the stroma vascular cell fraction compared to ADAM17 expression in mature adipocytes, the quantitative detection of our knock out strategy in adipocytes cannot be easily determined when measuring ADAM17 in the whole mouse mice. Therefore, we isolated the stromovascular fraction from iWAT of Adip^{Cre+}ADAM17KO and Adip^{Cre-}WT mice and we differentiated them *in vitro* to mature adipocytes. This protocol of *in vitro* differentiation of primary cells to mature adipocytes typically results in 80-90% differentiation of precursor cells to mature adipocytes. With this approach, we observed 60% lower mRNA levels of ADAM17 and protein levels in the iWAT of Adip^{Cre+}ADAM17KO mice compared to Adip^{Cre-}WT mice (Figure 14c-f). Interestingly we could see this deletion in the floxed exon 2 of ADAM17, but subsequent exon to exon were still detected to have similar mRNA levels between the two genotypes. Due to the lack of stop codon, it is possible that ADAM17 mRNA is formed but not translated.

a

ATGAGGCGGCGTCTCCTCATCCTGACCACTTTGGTGCCTTTCGTCCTGGCACCCCGACCTCCGGAGGAAGCAGGCTCTGGCTCCCATC
CGCGACTTGAGAAGCTTGATTCTTTGCTCTCAGACTACGACATCCTCTCCTTAGCTAATATTCAGCAGCACTCCATAAGGAAAAGGGATC
TACAGTCTGCGACACACTTAGAAACATTACTAACTTTTTCAGCTTTGAAAAGACATTTTAAATTATACTTGACATCAAGTACCGAACGCTT
TTCACAAAACTTGAGAGTCGTGGTGGTGGACGGGAAAGAAGAAAGCGAGTACAGCGTGAAGTGGCAGAACTTCTTCAGTGGTCACGT
GGTTGGTGAGCCTGACTCTAGGGTTCTAGCCCACATAGGAGATGATGATGTTACAGTGAGAATCAACACAGATGGGGCAGAATATAAC
GTAGAGCCACTTTGGAGGTTTGTCAATGATACTAAAGATAAACGAATGCTGGTGTATAAGTCTGAAGATATCAAGGATTTTTCACGTTTG
CAGTCTCCAAAAGTATGTGGTTATTTAAATGCAGATAGTGAAGAGCTGCTTCCAAAAGGGCTCATAGACAGAGAGCCATCTGAAGAGTT
TGTTCGTCGAGTGAAGAGACGAGCTGAACCTAACCCCTTGAAGAATACTTGTAAATTACTGGTGGTAGCAGATCATCGATTTTATAAATA
CATGGGCCGTGGAGAAGAGAGCACCACTACAAATTACTTAGGCTACATTTCAGGCACTCGGGACAGAGTGACGACCGACTGCTTTTTA
GAGTTTTTGATAGAGCTAATTGACCGAGTTGATGACATATACCGGAACACGTCGTGGGATAATGCAGGGTTTAAAGGGTATGGAGTGCA
GATAGAGCAGATTCGAATTCTCAAGTCTCCACAAGAGGTAAAACCTGGTGAAAGACACTTCAATATGGCAAAAAGTTTCCCAAACGAA
GAGAAGGATGCTTGGGATGTGAAGATGCTATTAGAGCAATTTAGCTTTGATATAGCTGAAGAAGCATCTAAAGTCTGCCTGGCTCATCTT
TTCACGTACCAGGATTTTGATATGGGAACTCTTGGATTAGCTTACGTTGGTTCTCCCAGAGCAAACAGTCATGGAGGGGTTTGTCCAAA
AGCTTATTACAACCCAACTGTGAAGAAAAACATCTATTTAAATAGTGGTCTGACTAGTACTAAAAATTATGGCAAAACTATTCTCACAAAG
GAAGCTGACCTGGTTACAACTCATGAATTGGGACATAATTTTGGAGCAGAACATGACCCTGATGGGCTAGCAGAATGTGCCCCAAATG
AGGACCAAGGAGGAAAGTATGTCATGTATCCCATAGCTGTGAGCGGTGACCACGAGAATAATAAGATGTTTTCAAACTGCAGTAAACAG
TCCATCTACAAGACCATAGAAAGTAAGGCTCAAGAGTGCTTCCAGGAGCGCAGCAACAAGGTGTGTGGCAACTCCAGGGTGGATGAA
GGAGAGGAGTGTGACCCGGGTATTATGTACCTGAACAACGACACCTGCTGCAATAGTGACTGCACACTGAAGCCGGGTGTGCAGTGC
AGTGATAGGAACAGTCCTTGCTGTAAAAACTGTCAGTTTGAGACGGCGCAGAAGAAGTGCCAGGAGGCTATTAATGCTACATGCAAAG
GAGTGTCTTACTGCACAGGGAATAGCAGTGAGTGCCCCCCACCCGGAGATGCTGAAGATGACACTGTGTGCTTGGACCTTGGCAAGT
GCAAGGCTGGGAAATGCATCCCTTTCTGCAAGAGGGAGCAGGAGCTGGAGTCCTGCGCATGCGTTGACACTGACAACTCGTGCAAG
GTGTGCTGCAGGAACCTTTCTGGCCCGTGTGTGCCGTACGTCGATGCAGAGCAAAAGAACTTGTTTTTGAGGAAAGGGAAGCCATGTA
CAGTAGGGTTTTGCGACATGAATGGCAAATGTGAGAAACGAGTACAGGACGTAATTGAGCGATTTTGGGATTTCATTGACCAGCTGAGC
ATCAACACTTTTGGGAAGTTTCTGGCAGATAACATCGTTGGGTCTGTTCTGGTTTTCTCCTTGATATTTTGGATTCCTTTCAGCATTCTTGT
CCACTGTGTGGATAAGAAACTGGACAAGCAGTATGAATCCCTGTCTCTGTTTCATCACAGTAACATTGAGATGCTGAGCAGCATGGACT
CAGCATCTGTTCGCATCATCAAGCCCTTTCCTGCACCCCAGACTCCAGGTCGTCTGCAGGCCCTGCAGCCAGCTGCCATGATGCCGCC
AGTACCTGCAGCTCCAAAACTGGACCACCAGAGGATGGACACCATCCAGGAAGACCCCAGCACAGACTCACATGCAGATGATGACG
GTTTTGAGAAGGACCCCTTCCCCAACAGCAGCACAGCTGCCAAGTCCTTTGAGGATCTCACAGACCACCCAGTCACCAGGAGCGAAA
AGGCGGCCTCATTCAAGCTGCAGCGTCAGAGCCGAGTTGACAGCAAAGAGACAGAGTGCTAG

b

MRRRLLILTTLVPFVLAPRP		MRRRLLILTTLVPFVLAPRP
PEEAGSGSHPRLEKLDSLLS		PEEAGSGSHPRLDILNYT*H
DYDILSLANIQQHSIRKRDL		QVPNAFHKT*ESWWWTGKKK
QSATHLETLLTFSALKRHFK		ASTA*SGRTSSVVTWLVSLT
LYLTSSTERFSQNLRVVVVD		LGF*PT*EMMMLQ*ESTQMG
GKEESEYSVKWQNFFSGHVV		QNIT*SHFGGLSMILKINEC
GEPDSRVLAHIGDDDVTVRI		WCISLKISRIFHVCSLQKYV
NTDGAEYNVEPLWRFVNDTK		VI*MQIVKSCFQKGS*TESH
DKRMLVYKSEDIKDFSRLQS		LKSLFVE*RDELNLTP*RIL
PKVCGYLNADSEELLPKGLI		VNYWW*QIIDFINTWAVEKR
DREPSEEFVRRVKRRAEPNP		APLQIT*ATFQALGTE*RPT
LKNTCKLLVVADHRFYKYMG		AF*SF**S*LTELMTYTGTR
RGEESTTTNYLGYISGTRDR		RGIMQGLKGMECR*SRFEFS
VTTDCFLEFLIELIDRVDDI		SLHKR*NLVKDTSIWQKVSQ
YRNTSWDNAGFKGYGVQIEQ	Exon 2 deletion	TKRRMLGM*RCY*SNLALI*
IRILKSPQEVKPGERHFNMA		LKKHLKSAWLIFSRTRILIW
KSFPNEEKDAWDVKMLLEQF		ELLD*LTLVLPEQTVMEGFV
SFDIAEEASKVCLAHLFTYQ	→	QKLITTQL*RKTSI*IVV*L
DFDMGTLGLAYVGSPRANSH		VLKIMAKLFSQRKLTWLQLM
GGVCPKAYYNPTVKKNIYLN		NWDIILEQNMTLMG*QNVPQ
SGLTSTKNYGKTILTKEADL		MRTKEESMSCIP*L*AVTTR
VTTHELGHNFGAEHDPDGLA		IIRCFQTAVNSPSTRP*KVR
ECAPNEDQGGKYVMYPIAVS		LKSASRSAATRCVATPGWMK
GDHENNKMFSNCSKQSIYKT		ERSVTRVLCT*TTTPAAIVT
IESKAQECFQERSNKVCGNS		AH*SRVCSAVIGTVLAVKTV
RVDEGEECDPGIMYLNNDTC		SLRRRRRSARRLLMLHAKEC
CNSDCTLKPGVQCSDRNSPC		LTAQGIAVSAPHPEMLKMTL
CKNCQFETAQKKCQEAINAT		CAWTLASARLGNASLSARGS
CKGVSYCTGNSSECPPPGDA		RSWSPAHALTLTTRARCAAG
EDDTVCLDLGKCKAGKCIPF		TFLARVCRTSMQSKRTCF*G
CKREQELESCACVDTDNSCK		KGSHVQ*GFAT*MANVRNEY
VCCRNLSGPCVPYVDAEQKN		RT*LSDFGISLTS*ASTLLG
LFLRKGKPCTVGFCDMNGKC		SFWQITSLGLFWFSP*YFGF
EKRVQDVIERFWDFIDQLSI		LSAFLSTVWIRNWTSSMNPC
NTFGKFLADNIVGSVLVFSL		LCFITVTLRC*AAWTQHLFA
IFWIPFSILVHCVDKKLDKQ		SSSPFLHPRLQVVCRPCSQL
YESLSLFHHSNIEMLSSMDS		P*CRQYLQLQNWTTRGWTPS
ASVRIIKPFPAPQTPGRLQA		RKTPAQTHMQMMTVLRRTPS
LQPAAMMPPVPAAPKLDHQR		PTAAQLPSPLRISQTTQSPG
MDTIQEDPSTDSHADDDGFE		AKRRPHSSCSVRAELTAKRQ
KDPFPNSSTAAKSFEDLTDH		SA
PVTRSEKAASFKLQRQSRVD		

Figure 13: Exon2 deletion of ADAM17 results in out-of-frame transcription.

(a) cDNA sequence of mouse ADAM17 with underlined exon2 sequence, (b) left side shows the mouse ADAM17 protein sequence and the right side show the results of in silico exon 2 deletion on the mouse ADAM17 protein sequence. Mouse ADAM17 was acquired by Ensembl.org and in-silico translation was performed with Ape software.

Table 6: **Percentage of genome similarity of the six-time backcrossed Adiponectin-CrexAdam16flox/flox line to the genome of 129P2/OlaHsd-SJL/J mouse line and the genome of C57BL6/J mouse line.**

The comparison is based on the sequences of a panel of 130 SNPs, used to distinguish between the two genetic backgrounds 129P2/OlaHsd-SJL/J and C57BL6/J. Twenty mice AdiponectinCre x ADAM17 flox/flox were send to the Jackson for SNP Genome Scanning Analysis.

Sample	129P2/OlaHsd-SJL/J	C57BL/6J
835935 1	0.78%	99.22%
835935 2	2.34%	97.66%
835935 3	3.13%	96.88%
835935 4	3.13%	96.88%
835935 5	2.73%	97.27%
835935 6	3.91%	96.09%
835935 7	2.34%	97.66%
835935 8	2.73%	97.27%
835935 9	3.91%	96.09%
835935 10	1.56%	98.44%
835935 11	1.95%	98.05%
835935 12	3.13%	96.88%
835935 13	2.34%	97.66%
835935 14	1.95%	98.05%
835935 15	2.34%	97.66%
835935 16	2.34%	97.66%
835935 17	2.73%	97.27%
835935 18	3.13%	96.88%
835935 19	2.34%	97.66%
835935 20	2.73%	97.27%
B6J	0.00%	100.00%
129S	100.00%	0.00%
SJL	100.00%	0.00%
HET	50.00%	50.00%
NTC		

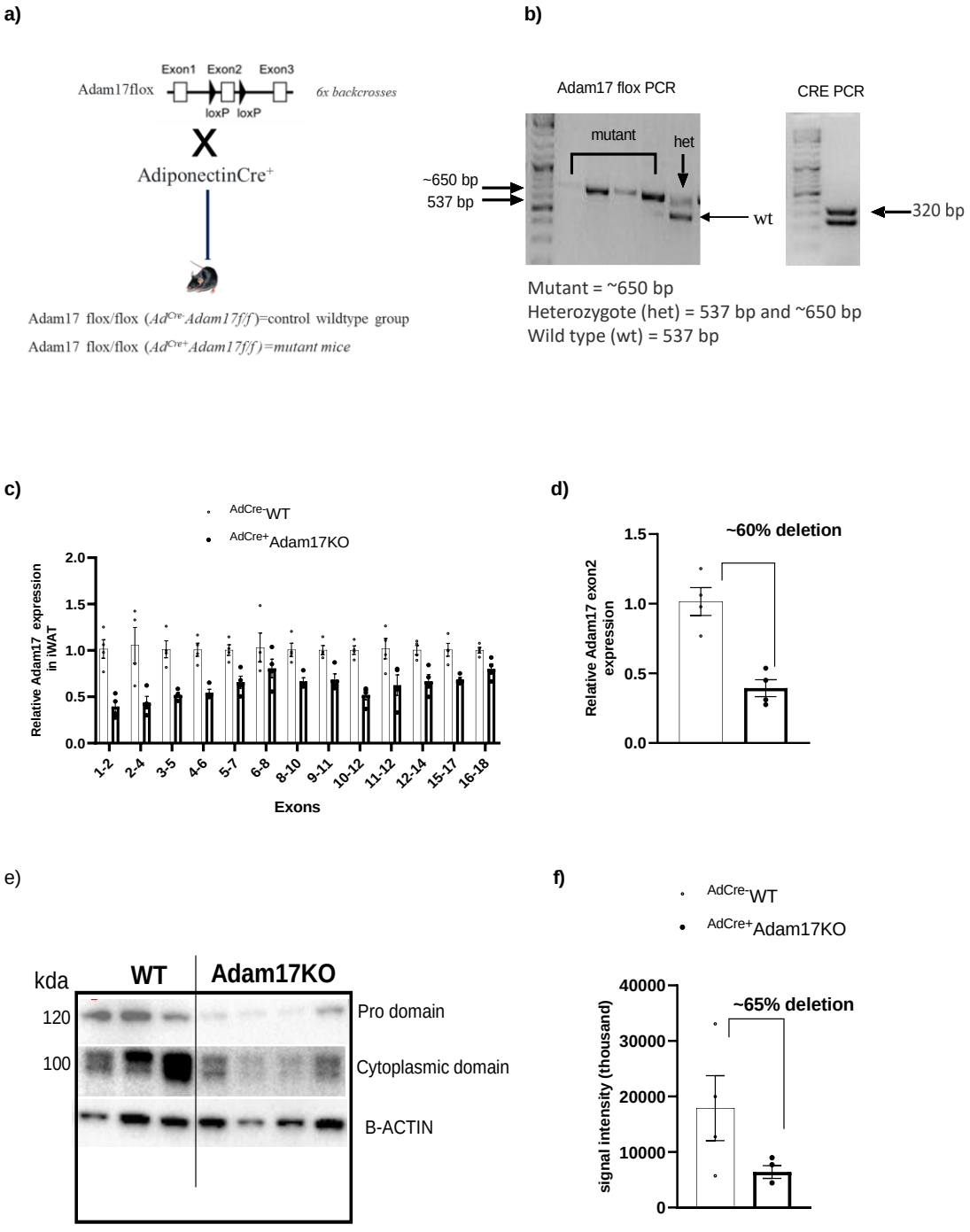

Figure 14: Efficiency of ADAM17 deletion in adipose tissue of Adip^{Cre+}ADAM17KO mouse. (a) Conditional targeting of ADAM17; arrow heads indicate the loxP sites placed surrounding exon 2. Mice carrying the floxed ADAM17 allele were backcrossed 6 generation and after crossed with Adiponectin transgenic mice resulting in the exon2 of ADAM17 deletion in the adipose tissue, (b) PCR analysis of genomic DNA isolated from heterozygous and homozygous ADAM17flox/flox mice, (c) mRNA levels of all exons ADAM17,(d) as wells as only exon 2 and (e) protein levels in the iWAT of Adip^{Cre+}Adam17KO mice compared to Adip^{Cre-}WT mice. Protein levels are shown as western blot (f), which is then quantified and normalized to b-actin. Data are shown as mean± SEM. * is p-value <0.05 calculated by a student's t-test.

3.8 5 day injections with ADRB3 specific agonist, CL 316,243 caused no differences in energy expenditure, but led to lower cholesterol in Adip^{Cre+}ADAM17KO mice compared to Adip^{Cre-}WT control mice.

To investigate the role of ADAM17 on affecting in vivo response to ADRB3 agonists, we acclimated Adip^{Cre+}ADAM17KO mice and Adip^{Cre-}WT at 28 °C for 2 weeks to minimize the baseline sympathetic nervous system activity and after that period, we delivered by intraperitoneal injection (ip) of CL 316,243 (0,5 mg/kg) for 5 consecutive days. CL 316,243 is a selective beta 3 adrenergic receptor agonist. Typically, acute CL 316,243 delivery results in a drop of blood glucose levels, due to increased insulin secretion, which is stimulated by the acute release of NEFA in the blood stream (MacPherson *et al*., 2014). To confirm that the dose of 0,5 mg/kg CL 316,243 was effective we measured blood glucose levels in injected Adip^{Cre+}ADAM17KO mice and Adip^{Cre-}WT controls, which had no access to food after 2h and 4h post a single CL 316,243 ip injection. We observed a 40% drop in blood glucose levels in both genotypes (Fig. 15a-b). Indirect calorimetry data did not reveal any differences between the genotypes, in oxygen consumption (VO2) (Fig. 16a-b), carbon dioxide consumption (VCO2) (Fig. 16d-e), energy expenditure (EE) (Fig. 16 g-h) and Resting energy expenditure (RER) (Fig.16j-k) within the first 24 hour.

We continued once a day ip injection of CL 316,243, for 5 consecutive days and sacrificed the animals 24 hours after the last injection. After long term exposure to CL 316,243 we observed a significant weight loss in the Adip^{Cre-}WT controls, but not in the Adip^{Cre+}ADAM17KO group (Fig. 15c). We observed no significant difference in the fat tissues or non-fat organs between the genotypes (Fig. 15d), just iWAT of Adip^{Cre+}ADAM17KO mice showed a trend towards higher weight. In addition, we observed no difference in fasting blood glucose levels (Fig. 15b). We observed no significant differences between the genotypes in oxygen consumption (VO2) (Fig. 16a), in carbon dioxide consumption (VCO2) (Fig. 16b), in energy expenditure (EE) (Fig. 16c). Interestingly, we observed a trend towards higher RER in the Adip^{Cre+}ADAM17KO mice compared to the Adip^{Cre-}WT controls (Fig. 16j-k), towards the end of the study, indicative of possible lower dependance of the Adip^{Cre+}ADAM17KO mice on lipids oxidation than the Adip^{Cre-}WT controls.

Despite no major differences in EE and body composition, we observed lower HDL cholesterol in Ad^{Cre+}ADAM17KO, compared to the Ad^{Cre-}WT controls, after 5 days of CL 316,243 injections (Fig.15f). There was no difference in serum triglycerides (Fig. 15f) and serum NEFA (Fig. 15f) between the genotypes.

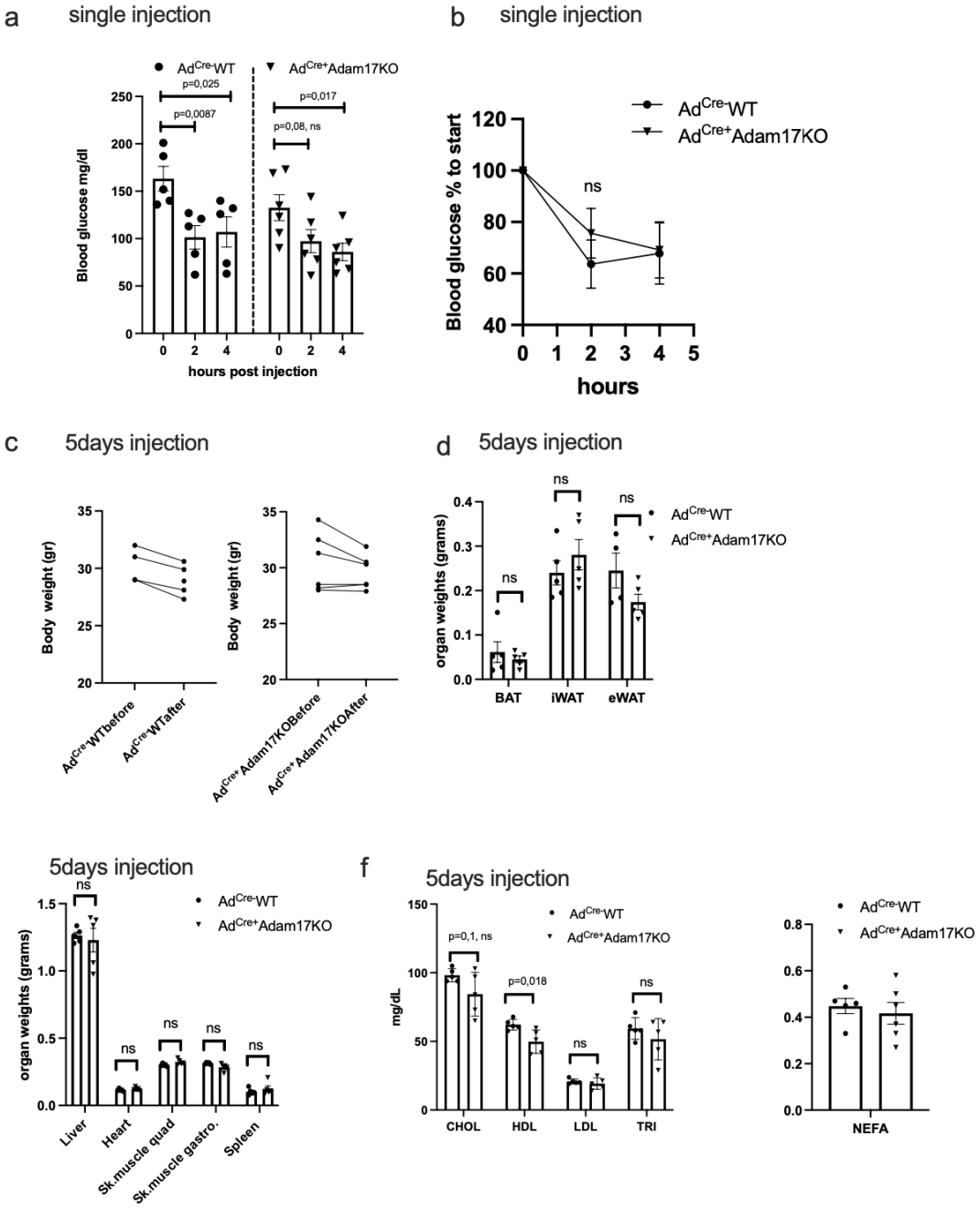

Figure 15: Response of Adip^{Cre+}ADAM17KO and Adip^{Cre-}WT to single- and five-days CL 316,243 (0,5mg/kg) injections.

(a) Blood glucose (mg/dl) measurements taken at different 0, 2, 4 hours after single dose of CL 316, 243 (0,5mg/kg) injections. (b) Blood glucose as percentage to start of single dose of CL 316, 243 (0,5mg/kg) injections. (c) Body weights, (d) fat weight and (e) organ weights after five days of CL 316, 243 (0,5mg/kg) injections between Ad^{Cre+}ADAM17KO and Ad^{Cre-}WT.(f) After 5 days of CL 316, 243 (0,5mg/kg) injections serum total cholesterol, high-density lipoprotein (HDL), low-density lipoprotein (LDL) triglycerides and Non-esterified fatty acids (NEFA) were measured. (Mice were housed at thermoneutrality (28^{o}C-29^{o}C). Data are shown as mean$\pm$ SEM. * is p-value <0.05 calculated by a student's t-test. Mice were 10-12 weeks old, males.

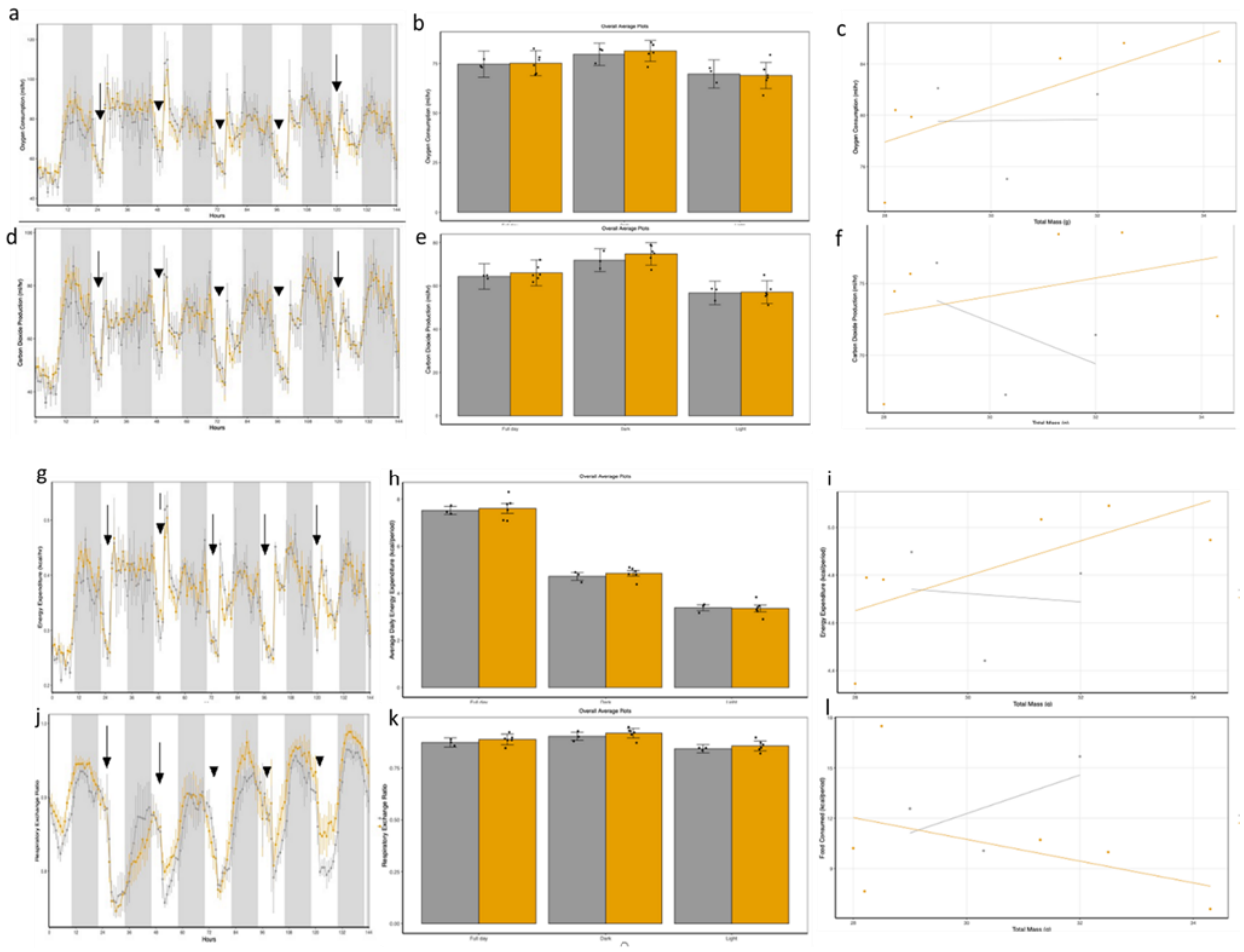

GLM

	Full Day			Light			Dark		
Effect	Mass	Group	Interaction	Mass	Group	Interaction	Mass	Group	Interaction
Food Consumed (kcal/period)	0.5048	0.4212		0.8469	0.8431		0.4818	0.4062	
Water Consumed (ml/period)	0.7393	0.2210		0.8068	0.1461		0.7059	0.5441	
Energy Expenditure (kcal/period)	0.0221 *	0.7497		0.0522	0.8549		0.1432	0.5144	
Oxygen Consumption (ml/hr)	0.0136 *	0.8353		0.0449 *	0.8090		0.0805	0.5426	
Carbon Dioxide Production (ml/hr)	0.1749	0.5063		0.1167	0.9075		0.6234	0.4531	

ANOVA

	Full Day	Light	Dark
Effect	Group	Group	Group
Respiratory Exchange Ratio	0.4204	0.4457	0.4525
Locomotor Activity (beam breaks)	0.2710	0.6263	0.1600
Ambulatory Activity (beam breaks)	0.2275	0.5296	0.1560

Adip^{Cre-}WT
Adip^{Cre+}Adam17KO

Figure 16: Indirect calorimetry on Adip^{Cre+}ADAM17KO and Adip^{Cre-}WT mice injected every day for 5 days with CL 316,243, housed in 28^{o}C.

(a) Oxygen (O_2) consumption (arrows indicated the point of ip injection of CL 316,243), (b) Bar plots of Oxygen (O_2) consumption and (c) Regression analysis of oxygen consumption. (d) Carbon dioxide production (arrows indicated the point of ip injection of CL 316,243), (e) bar plots carbon dioxide production and (c) regression analysis of carbon dioxide production. (g) Energy expenditure (ee) (arrows indicated the point of ip injection of CL 316,243), (h) energy expenditure (ee), and (i) regression analysis of ee. (j) Respiratory exchange rate (rer), and (i, k) food consumption. Table of statistics is shown below. Mice were 10-12 weeks old, males.

3.9 Adip^{Cre+}Adam17KO mice showed impaired adaptation to cold temperature.

Norepinephrine signaling via Adrb3 is crucial in stimulating the thermogenic action of mature brown adipocytes, but also the recruitment of beige adipocytes via trans-differentiation of white adipocytes to beige (Pilkington *et al*., 2021). This remodeling of the adipose tissue is accompanied by increased lipolysis, increased lipid oxidation and mitochondrial respiration (Auger & Kajimura, 2023). To investigate the impact of adipocyte specific ADAM17 deletion in cold induced systemic adaptation we exposed Adip^{Cre+}ADAM17KO and Adip^{Cre-}WT in cold air environment, 8 °C for 2 weeks and collected indirect calorimetry data during that period.

We found that Adip^{Cre+}Adam17KO exhibited lower oxygen consumption (Fig. 17a-b lower carbon dioxide emission (Fig. 17d-e) and lower energy expenditure (Fig. 20g-h), compared to Adip^{Cre-}WT mice. Regression analysis showed this was not dependent on body weight differences between the two genotypes (Fig. 17c, f, i). We found no significant differences in food intake (Fig. 17-table) between the genotypes. Although both genotypes had similar weights at the beginning of the study, after 1-week Adip^{Cre+}Adam17KO group weighted less than Adip^{Cre-}WT control (Fig. 18 a), mainly because Adip^{Cre-}WT mice gained body fat compared to the start, whereas Adip^{Cre+}Adam17KO did not (Fig.18b). However, at the end of the study Adip^{Cre+}Adam17KO showed no significant differences in lean mass (Fig. 18c) or any other organs and specific adipose tissue weights compared to the controls (Fig. 18d-e).

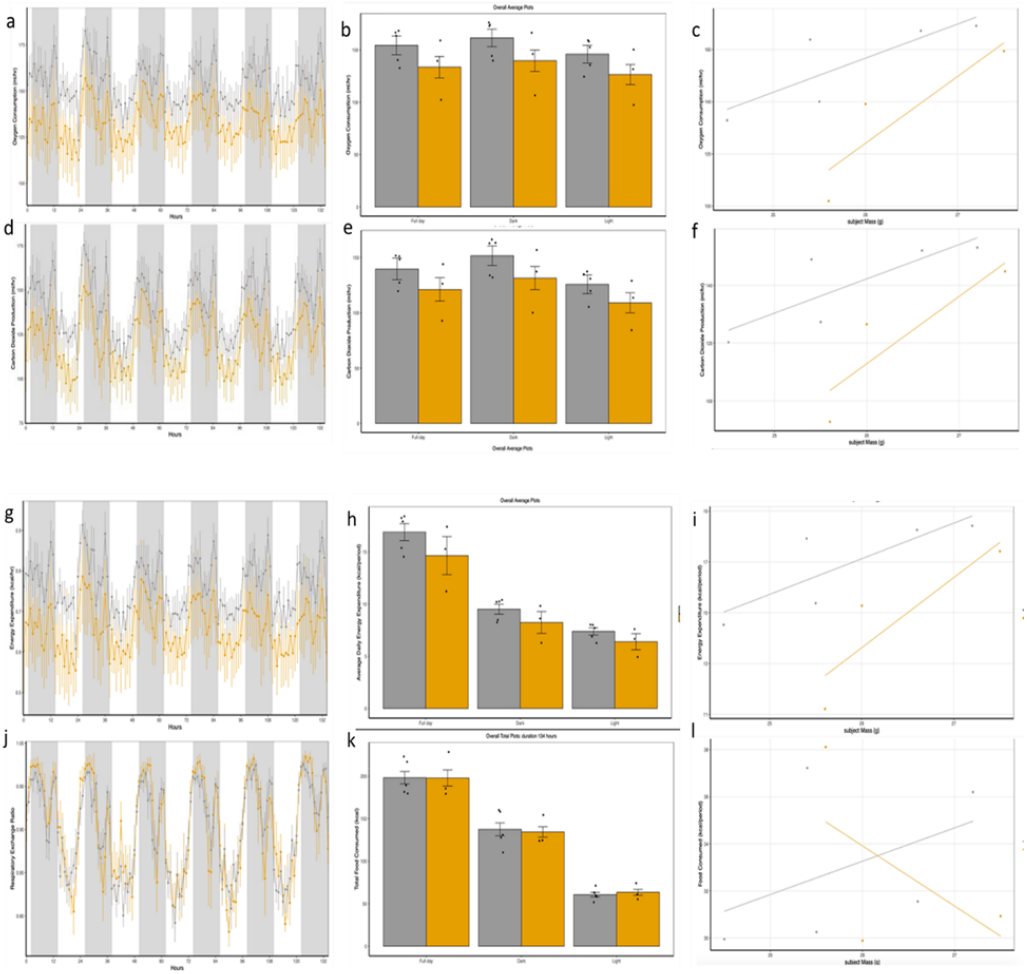

GLM

Effect	Full Day Mass	Full Day Group	Full Day Interaction	Light Mass	Light Group	Light Interaction	Dark Mass	Dark Group	Dark Interaction
Food Consumed (kcal/period)	0.9083	0.9611		0.8309	0.6524		0.8282	0.8116	
Water Consumed (ml/period)	0.5181	0.2093		0.4983	0.2012		0.5368	0.2184	
Energy Expenditure (kcal/period)	0.0274 *	0.0374 *		0.0194 *	0.0278 *		0.0359 *	0.0472 *	
Oxygen Consumption (ml/hr)	0.0272 *	0.0370 *		0.0193 *	0.0278 *		0.0354 *	0.0461 *	
Carbon Dioxide Production (ml/hr)	0.0280 *	0.0385 *		0.0207 *	0.0291 *		0.0380 *	0.0512	

ANOVA

Effect	Full Day Group	Light Group	Dark Group
Respiratory Exchange Ratio	0.6076	0.8644	0.8752
Locomotor Activity (beam breaks)	0.7897	0.7753	0.8127
Ambulatory Activity (beam breaks)	0.7939	0.8091	0.8026

Mass effect: subject.mass.x
Signif. codes: <0.001 ***,<0.01 **,<0.05 *

Figure 17: Indirect calorimetry, 1-week cold exposure on Adip^{Cre+}ADAM17KO and Adip^{Cre-}WT mice.

(a) Oxygen (O_2) consumption, (b) Bar plots of Oxygen (O_2) consumption and (c) Regression analysis of oxygen consumption. (d) Carbon dioxide production (arrows indicated the point of ip injection of CL 316,243), (e) bar plots carbon dioxide production and (c) regression analysis of carbon dioxide production. (g) Energy expenditure (ee) (arrows indicated the point of ip injection of CL 316,243), (h) energy expenditure (ee), and (i) regression analysis of ee. (j) Respiratory exchange

rate (rer), and (i, k) food consumption. Table of statistics is shown below. Mice were Adip^{Cre+}Adam17KO and Adip^{Cre-}WT, 10-12 weeks old, males.

To identify molecular pathways and molecular signatures associated with these differences, we performed untargeted proteomics in the thermogenic fat depots BAT and iWAT of Adip^{Cre+}Adam17KO and Adip^{Cre-}WT, after 1-week cold exposure. We examined major thermogenic pathways and futile cycles. We observed no difference in Ucp1 protein levels in BAT and iWAT, meaning that both tissues had generated thermogenic Ucp1 positive cells to the same extend upon cold exposure. Interestingly, in BAT we observed an upregulation of genes regulating creatine metabolism (CKM, CKMT2), calcium transport (ATP2a1), ATP synthesis (ATP5F1D, ATP6V1G1), glycolysis and glycogen synthesis (PYGM, ENO3, PGAM2, FBP1), whereas not so many proteins were greatly downregulated. In iWAT we also observed most genotype different proteins to be upregulated and amongst them we found several proteins involved in oxidative phosphorylation, specifically complex I (NDUFS5, NDUFS6, NDUFA7, COX6B1, UQCRH), fatty acid synthesis and esterification (ACAA2, ACOT2, CYP27A1), cholesterol transport (Apoa1, Apoa4), TCA cycle (FADH1M,IDH3A, SDHC, ACO2, DLST), glycolysis and gluconeogenesis (FBP1, MPC2,PDK4, PDHA2).

Taken all together these findings suggest that ADAM17 deletion in adipocytes leads to impaired adaptation to cold exposure. However, at the molecular levels in BAT and iWAT, UCP1 protein levels are increased in both genotypes in response to cold exposure, however, it is evident that in BAT of Ad^{Cre+}ADAM17KO mice there is substantial recruitment of ATP utilizing futile pathways, such as the creatine pathway and calcium mobilization from the ER. Consistent with this, there is increased glycolysis to provide ATP to the cells. In iWAT, there is also a molecular signaling of increased glycolysis and potentially fatty acid biosynthesis or recycling. Overall suggesting a potential problem of uncoupled thermogenesis, despite the high presence of UCP1.

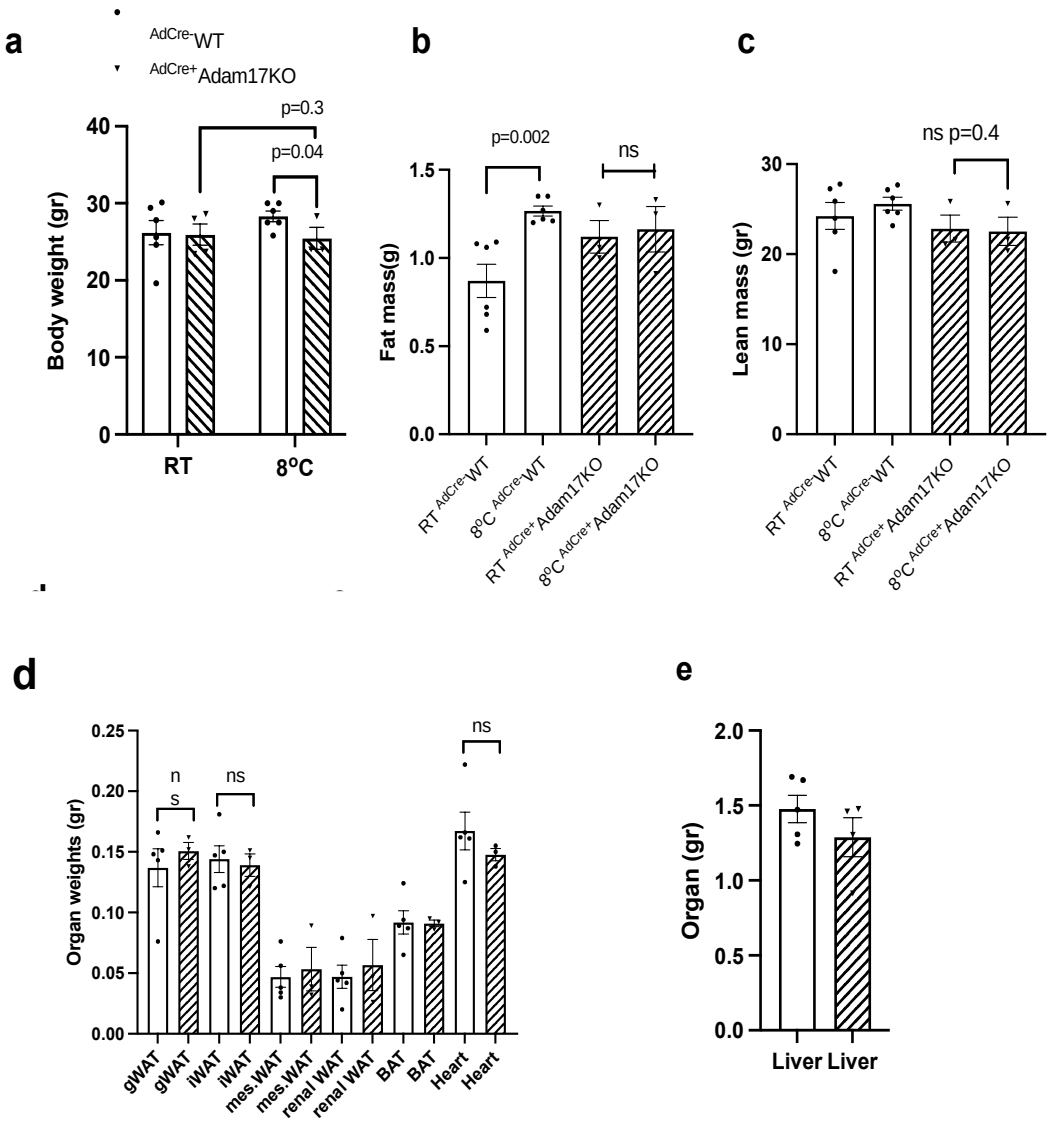

Figure 18: Weight and body composition after 1 week in 8 °C.

(a) Body weight at room temperature (RT) and after 1 week of 8ºC cold exposure. (b) Fat content (c) lean mass and (d,e) depicted organ weights, at RT and after 1 week of 8 ºC cold exposure, of Adip^{Cre+}ADAM17 and Ad^{Cre-}WT, male mice, 10-12 weeks old. Data are shown as mean± SEM. * is p-value <0.05 calculated by a student's t-tes

Table 7: Differentially expressed proteins in BAT of Ad^{Cre+}ADAM17KO compared to Ad^{Cre-}WT, undergone 1-week cold exposure (8 °C). by untargeted proteomics in total tissue lysates.

Protein FDR Confidence Combined	Accession	Description	Gene Symbol	Number of Peptides	Number of Unique Peptides	Abundance Ratio AdCre+Adam17KO vsAdCre-WT	Abundance Ratio P-Value plus minus	Abundance Ratio Adj P-Value plus minus	Molculer function
Medium	Q80W22	Threonine synthase-like 2 OS=Mus musculus OX=10090 GN=Thnsl2 PE=1 SV=1	Thnsl2	1	1	9,36	0,0	0,0	
High	P58774	Tropomyosin beta chain OS=Mus musculus OX=10090 GN=Tpm2 PE=1 SV=1	Tpm2	28	12	7,88	0,0	0,0	Striated Muscle Contraction; Smooth Muscle Contraction
High	E9Q9A9	2'-5'-oligoadenylate synthase 2 OS=Mus musculus OX=10090 GN=Oas2 PE=1 SV=1	Oas2	1	1	7,78	0,0	0,0	mRNA processing
High	P62631	Elongation factor 1-alpha 2 OS=Mus musculus OX=10090 GN=Eef1a2 PE=1 SV=1	Eef1a2	15	5	7,61	0,0	0,0	Translation factors
High	P27573	Myelin protein P0 OS=Mus musculus OX=10090 GN=Mpz PE=1 SV=1	Mpz	4	4	7,36	0,0	0,0	plasma membrane;other membranes;ER/Golgi;other cytoplasmic organelle
High	P13412	Troponin I, fast skeletal muscle OS=Mus musculus OX=10090 GN=Tnni2 PE=2 SV=2	Tnni2	6	6	7,13	0,0	0,0	Striated Muscle Contraction
High	Q5EBG6	Heat shock protein beta-6 OS=Mus musculus OX=10090 GN=Hspb6 PE=1 SV=1	Hspb6	5	5	7,11	0,0	0,0	non-structural extracellular;cytosol;mitochondrion;ER/Golgi;nucleus;other cell component
High	P58771	Tropomyosin alpha-1 chain OS=Mus musculus OX=10090 GN=Tpm1 PE=1 SV=1	Tpm1	27	9	6,71	0,0	0,0	Striated Muscle Contraction; Smooth Muscle Contraction
High	P04247	Myoglobin OS=Mus musculus OX=10090 GN=Mb PE=1 SV=3	Mb	11	11	6,57	0,0	0,0	Intracellular oxygen transport
High	O89103	Complement component C1q receptor OS=Mus musculus OX=10090 GN=Cd93 PE=1 SV=1	Cd93	2	2	6,32	0,0	0,0	Neutrophil degranulation
High	Q9WV35	C->U-editing enzyme APOBEC-2 OS=Mus musculus OX=10090 GN=Apobec2 PE=1 SV=1	Apobec2	8	8	6,17	0,0	0,0	Formation of the Editosome
High	P32848	Parvalbumin alpha OS=Mus musculus OX=10090 GN=Pvalb PE=1 SV=3	Pvalb	13	13	6,06	0,0	0,0	
High	O88532	Zinc finger RNA-binding protein OS=Mus musculus OX=10090 GN=Zfr PE=1 SV=2	Zfr	1	1	6,02	0,0	0,0	nucleic acid binding activity;other molecular function
High	Q9WUB3	Glycogen phosphorylase, muscle form OS=Mus musculus OX=10090 GN=Pygm PE=1 SV=3	Pygm	52	39	5,98	0,0	0,0	**Glycogen breakdown (glycogenolysis)**
High	Q9QZ47	Troponin T, fast skeletal muscle OS=Mus musculus OX=10090 GN=Tnnt3 PE=1 SV=3	Tnnt3	10	7	5,82	0,0	0,0	Striated Muscle Contraction
High	O09165	Calsequestrin-1 OS=Mus musculus OX=10090 GN=Casq1 PE=1 SV=3	Casq1	11	11	5,63	0,0	0,0	Stimuli-sensing channels; Ion homeostasis
High	P07310	Creatine kinase M-type OS=Mus musculus OX=10090 GN=Ckm PE=1 SV=1	Ckm	24	23	5,44	0,0	0,0	**Creatine metabolism**
Medium	F2Z461	E3 ISG15--protein ligase Herc6 OS=Mus musculus OX=10090 GN=Herc6 PE=2 SV=1	Herc6	1	1	5,42	0,0	0,0	Antigen processing: Ubiquitination & Proteasome degradation
High	P20801	Troponin C, skeletal muscle OS=Mus musculus OX=10090 GN=Tnnc2 PE=1 SV=2	Tnnc2	7	7	5,14	0,0	0,0	Striated Muscle Contraction
High	P05977	Myosin light chain 1/3, skeletal muscle isoform OS=Mus musculus OX=10090 GN=Myl1 PE=1 SV=2	Myl1	20	17	4,94	0,0	0,0	Striated Muscle Contraction
High	P21550	Beta-enolase OS=Mus musculus OX=10090 GN=Eno3 PE=1 SV=3	Eno3	23	16	4,88	0,0	0,0	**Gluconeogenesis; Glycolysis**
High	Q9JKS4	LIM domain-binding protein 3 OS=Mus musculus OX=10090 GN=Ldb3 PE=1 SV=1	Ldb3	20	20	4,73	0,0	0,0	cytoskeletal activity;other molecular function
High	P97457	Myosin regulatory light chain 2, skeletal muscle isoform OS=Mus musculus OX=10090 GN=Mylpf PE=1 SV=3	Myl11	16	16	4,34	0,0	0,0	Smooth Muscle Contraction
High	Q8R429	Sarcoplasmic/endoplasmic reticulum calcium ATPase 1 OS=Mus musculus OX=10090 GN=Atp2a1 PE=1 SV=1	Atp2a1	45	31	4,12	0,0	0,0	Ion homeostasis; Ion transport by P-type ATPases; Reduction of cytosolic Ca++ levels
High	Q5SX40	Myosin-1 OS=Mus musculus OX=10090 GN=Myh1 PE=1 SV=1	Myh1	148	29	4,11	0,0	0,0	cytoskeletal activity;other molecular function
High	Q91Z83	Myosin-7 OS=Mus musculus OX=10090 GN=Myh7 PE=2 SV=1	Myh7	129	36	3,90	0,0	0,0	cytoskeletal activity;other molecular function
High	Q00898	Alpha-1-antitrypsin 1-5 OS=Mus musculus OX=10090 GN=Serpina1e PE=1 SV=1	Serpina1e	15	6	3,78	0,0	0,0	non-structural extracellular;ER/Golgi;other cell component
High	P97447	Four and a half LIM domains protein 1 OS=Mus musculus OX=10090 GN=Fhl1 PE=1 SV=3	Fhl1	17	17	3,70	0,0	0,0	plasma membrane;other membranes;cytosol;nucleus;other cell component
High	O70250	Phosphoglycerate mutase 2 OS=Mus musculus OX=10090 GN=Pgam2 PE=1 SV=3	Pgam2	13	10	3,62	0,0	0,0	**Gluconeogenesis; Glycolysis**
High	P04370	Myelin basic protein OS=Mus musculus OX=10090 GN=Mbp PE=1 SV=2	Mbp	5	5	3,59	0,0	0,0	plasma membrane;other membranes;nucleus;other cell component
High	P21107	Tropomyosin alpha-3 chain OS=Mus musculus OX=10090 GN=Tpm3 PE=1 SV=3	Tpm3	23	10	3,46	0,0	0,0	Striated Muscle Contraction; RHOV GTPase cycle; Smooth Muscle Contraction
High	Q6P8J7	Creatine kinase S-type, mitochondrial OS=Mus musculus OX=10090 GN=Ckmt2 PE=1 SV=1	Ckmt2	18	18	3,41	0,0	0,0	**Creatine metabolism**
High	Q5SX39	Myosin-4 OS=Mus musculus OX=10090 GN=Myh4 PE=2 SV=1	Myh4	160	40	3,17	0,0	0,0	cytoskeletal activity;nucleic acid binding activity;other molecular function
High	Q9CXZ1	NADH dehydrogenase [ubiquinone] iron-sulfur protein 4, mitochondrial OS=Mus musculus OX=10090 GN=Ndufs4 PE=1 SV=3	Ndufs4	8	8	2,75	0,0	0,0	**Complex I biogenesis**
High	Q9JK37	Myozenin-1 OS=Mus musculus OX=10090 GN=Myoz1 PE=1 SV=1	Myoz1	13	13	2,75	0,0	0,0	cytoskeleton;nucleus;other cell component
High	P68134	Actin, alpha skeletal muscle OS=Mus musculus OX=10090 GN=Acta1 PE=1 SV=1	Acta1	27	2	2,60	0,0	0,0	Striated Muscle Contraction
High	Q9D110	Coiled-coil-helix-coiled-coil-helix domain-containing protein 2 OS=Mus musculus OX=10090 GN=Chchd2 PE=2 SV=1	Chchd2	2	2	2,57	0,0	0,0	nucleic acid binding activity;other molecular function
High	Q62147	Sarcospan OS=Mus musculus OX=10090 GN=Sspn PE=1 SV=1	Sspn	1	1	2,53	0,0	0,0	plasma membrane;other membranes;ER/Golgi
High	Q9JI91	Alpha-actinin-2 OS=Mus musculus OX=10090 GN=Actn2 PE=1 SV=2	Actn2	54	37	2,48	0,0	0,0	RAF/MAP kinase cascade; Striated Muscle Contraction; Unblocking of NMDA receptors, glutamate binding and activation
High	P47857	ATP-dependent 6-phosphofructokinase, muscle type OS=Mus musculus OX=10090 GN=Pfkm PE=1 SV=3	Pfkm	26	22	2,40	0,0	0,0	**Glycolysis**
Medium	Q80U59	Uncharacterized protein KIAA0232 OS=Mus musculus OX=10090 GN=Kiaa0232 PE=1 SV=2	Kiaa0232	1	1	2,16	0,0	0,0	
High	P11087	Collagen alpha-1(I) chain OS=Mus musculus OX=10090 GN=Col1a1 PE=1 SV=4	Col1a1	8	8	2,16	0,0	0,0	extracellular structural activity;other molecular function
High	Q9D3D9	ATP synthase subunit delta, mitochondrial OS=Mus musculus OX=10090 GN=Atp5f1d PE=1 SV=1	Atp5f1d	3	3	2,15	0,0	0,0	Formation of ATP by chemiosmotic coupling; Cristae formation
High	Q9CR51	V-type proton ATPase subunit G 1 OS=Mus musculus OX=10090 GN=Atp6v1g1 PE=1 SV=3	Atp6v1g1	3	3	2,15	0,0	0,0	Insulin receptor recycling; Amino acids regulate mTORC1; ROS and RNS production in phagocytes; Transferrin endocytosis and recycling; Ion channel transport
High	P26883	Peptidyl-prolyl cis-trans isomerase FKBP1A OS=Mus musculus OX=10090 GN=Fkbp1a PE=1 SV=2	Fkbp1a	2	2	2,14	0,0	0,0	TGF-beta receptor signaling activates SMADs; mTORC1-mediated signalling; Calcineurin activates NFAT
High	Q9JJW6	Aly/REF export factor 2 OS=Mus musculus OX=10090 GN=Alyref2 PE=1 SV=1	Alyref2	2	2	2,14	0,0	0,0	mRNA processing
High	Q05816	Fatty acid-binding protein 5 OS=Mus musculus OX=10090 GN=Fabp5 PE=1 SV=3	Fabp5	9	9	2,12	0,0	0,0	**Neutrophil degranulation; Triglyceride catabolism; Signaling by Retinoic Acid**
High	Q7TQ48	Sarcalumenin OS=Mus musculus OX=10090 GN=Srl PE=1 SV=1	Slr	26	26	2,11	0,0	0,0	
High	Q64433	10 kDa heat shock protein, mitochondrial OS=Mus musculus OX=10090 GN=Hspe1 PE=1 SV=2	Hspe1	6	6	2,09	0,0	0,0	RHOG GTPase cycle
High	P97315	Cysteine and glycine-rich protein 1 OS=Mus musculus OX=10090 GN=Csrp1 PE=1 SV=3	Csrp1	6	6	2,07	0,0	0,0	
High	Q99LT0	Protein dpy-30 homolog OS=Mus musculus OX=10090 GN=Dpy30 PE=1 SV=1	Dpy30	3	3	2,07	0,0	0,0	
High	Q9QXD6	Fructose-1,6-bisphosphatase 1 OS=Mus musculus OX=10090 GN=Fbp1 PE=1 SV=3	Fbp1	5	5	2,05	0,0	0,0	**Glycolysis and gluconeogenesis**
Medium	Q8BR93	Putative nuclease HARBI1 OS=Mus musculus OX=10090 GN=Harbi1 PE=2 SV=1	Harbi1	1	1	0,24	0,0	0,0	plasma membrane;other membranes;cytosol;cytoskeleton;nucleus
Medium	Q52KR3	Protein prune homolog 2 OS=Mus musculus OX=10090 GN=Prune2 PE=1 SV=2	Prune2	1	1	0,36	0,0	0,0	cytosol;ER/Golgi;nucleus;other cell component
Medium	Q499E5	Storkhead-box protein 2 OS=Mus musculus OX=10090 GN=Stox2 PE=2 SV=2	Stox2	1	1	0,48	0,0	0,0	nucleus;other cell component

Table 8: Differentially expressed proteins in iWAT of Adip^{Cre+}ADAM17KO compared to Adip^{Cre-}WT, undergone 1-week cold exposure (8 °C). Quantified by untargeted proteomics in total tissue lysates.

Protein FDR Confidence Combined	Accession	Description	Gene Symbol	Number of Peptides	Number of Unique Peptides	Abundance AdCre+Adam17KOvsAdCre-WT	Abundance Ratio P-Value plus minus	Abundance Ratio Adj P-Value plus minus	Molecular Function
High	Q9CW03	Structural maintenance of chromosomes protein 3 OS=Mus musculus OX=10090 GN=Smc3 PE=1 SV=2	Smc3	1	1	100,00	0,0000	0,0000	SUMOylation of DNA damage response and repair proteins; Separation of Sister Chromatids
High	Q80TB8	Synaptic vesicle membrane protein VAT-1 homolog-like OS=Mus musculus OX=10090 GN=Vat1l PE=1 SV=2	Vat1l	2	2	100,00	0,0000	0,0000	
High	Q9Z1R3	Apolipoprotein M OS=Mus musculus OX=10090 GN=Apom PE=1 SV=1	Apom	1	1	100,00	0,0000	0,0000	Retinoid metabolism and transport
High	Q9DB73	NADH-cytochrome b5 reductase 1 OS=Mus musculus OX=10090 GN=Cyb5r1 PE=1 SV=1	Cyb5r1	2	2	100,00	0,0000	0,0000	Platelet degranulation ; Erythrocytes take up carbon dioxide and release oxygen
High	Q9ET22	Dipeptidyl peptidase 2 OS=Mus musculus OX=10090 GN=Dpp7 PE=1 SV=2	Dpp7	1	1	100,00	0,0000	0,0000	Neutrophil degranulation
High	Q99JT2	Serine/threonine-protein kinase 26 OS=Mus musculus OX=10090 GN=Stk26 PE=1 SV=1	Stk26	1	1	100,00	0,0000	0,0000	Apoptotic cleavage of cellular proteins
High	Q4FZG7	Putative mitochondrial import inner membrane translocase subunit Tim8 A-B OS=Mus musculus OX=10090 GN=Timm8a2 PE=3 SV=1	Timm8a2	1	1	100,00	0,0000	0,0000	
High	Q9DBG1	Sterol 26-hydroxylase, mitochondrial OS=Mus musculus OX=10090 GN=Cyp27a1 PE=1 SV=1	Cyp27a1	1	1	100,00	0,0000	0,0000	**Synthesis of bile acids and bile salts via 27-hydroxycholesterol; Endogenous sterols**
High	Q3V1L4	Cytosolic purine 5'-nucleotidase OS=Mus musculus OX=10090 GN=Nt5c2 PE=1 SV=2	Nt5c2	1	1	100,00	0,0000	0,0000	Purine metabolism
High	Q921M3	Splicing factor 3B subunit 3 OS=Mus musculus OX=10090 GN=Sf3b3 PE=1 SV=1	Sf3b3	1	1	100,00	0,0000	0,0000	mRNA Splicing - Major Pathway; mRNA Splicing - Minor Pathway
Medium	Q791T5	Mitochondrial carrier homolog 1 OS=Mus musculus OX=10090 GN=Mtch1 PE=1 SV=1	Mtch1	1	1	100,00	0,0000	0,0000	
Medium	Q3TQB2	FAD-dependent oxidoreductase domain-containing protein 1 OS=Mus musculus OX=10090 GN=Foxred1 PE=1 SV=1	Foxred1	1	1	100,00	0,0000	0,0000	
High	Q6NXH9	Keratin, type II cytoskeletal 73 OS=Mus musculus OX=10090 GN=Krt73 PE=1 SV=1	Krt73	7	1	8,56	0,0000	0,0000	Formation of the cornified envelope
High	Q9QZJ6	Microfibrillar-associated protein 5 OS=Mus musculus OX=10090 GN=Mfap5 PE=1 SV=1	Mfap5	1	1	3,31	0,0000	0,0000	Molecules associated with elastic fibres
High	Q8R0F8	Acylpyruvase FAHD1, mitochondrial OS=Mus musculus OX=10090 GN=Fahd1 PE=1 SV=2	Fahd1	2	2	2,76	0,0000	0,0000	**Citric acid cycle (TCA cycle)**
Medium	B2RVY9	Transmembrane protein 182 OS=Mus musculus OX=10090 GN=Tmem182 PE=1 SV=1	Tmem182	1	1	2,68	0,0000	0,0000	
High	P09813	Apolipoprotein A-II OS=Mus musculus OX=10090 GN=Apoa2 PE=1 SV=2	Apoa2	2	2	2,36	0,0000	0,0000	**Chylomicron assembly; Chylomicron remodeling**
High	Q924X2	Carnitine O-palmitoyltransferase 1, muscle isoform OS=Mus musculus OX=10090 GN=Cpt1b PE=1 SV=1	Cpt1b	14	14	2,07	0,0000	0,0000	**Carnitine metabolism; Signaling by Retinoic Acid**
Medium	Q8BHC0	Lymphatic vessel endothelial hyaluronic acid receptor 1 OS=Mus musculus OX=10090 GN=Lyve1 PE=1 SV=1	Lyve1	1	1	1,95	0,0000	0,0003	Hyaluronan uptake and degradation
High	Q00898	Alpha-1-antitrypsin 1-5 OS=Mus musculus OX=10090 GN=Serpina1e PE=1 SV=1	Serpina1e	15	7	1,94	0,0000	0,0000	
High	Q60590	Alpha-1-acid glycoprotein 1 OS=Mus musculus OX=10090 GN=Orm1 PE=1 SV=1	Orm1	3	1	1,92	0,0000	0,0000	Neutrophil degranulation; Platelet degranulation
High	Q9DCT8	Cysteine-rich protein 2 OS=Mus musculus OX=10090 GN=Crip2 PE=1 SV=1	Crip2	1	1	1,89	0,0000	0,0000	
High	O08677	Kininogen-1 OS=Mus musculus OX=10090 GN=Kng1 PE=1 SV=1	Kng1	20	20	1,85	0,0000	0,0001	ACE inhibitor pathway
High	Q8K482	EMILIN-2 OS=Mus musculus OX=10090 GN=Emilin2 PE=1 SV=1	Emilin2	2	2	1,84	0,0000	0,0001	Molecules associated with elastic fibres
High	O70571	[Pyruvate dehydrogenase (acetyl-transferring)] kinase isozyme 4, mitochondrial OS=Mus musculus OX=10090 GN=Pdk4 PE=1 SV=1	Pdk4	3	3	1,79	0,0001	0,0014	**Regulation of pyruvate dehydrogenase (PDH) complex; Signaling by Retinoic Acid**
Medium	Q9EPU0	Regulator of nonsense transcripts 1 OS=Mus musculus OX=10090 GN=Upf1 PE=1 SV=2	Upf1	1	1	1,74	0,0007	0,0059	Nonsense Mediated Decay (NMD) independent of the Exon Junction Complex (EJC)
High	P55002	Microfibrillar-associated protein 2 OS=Mus musculus OX=10090 GN=Mfap2 PE=2 SV=1	Mfap2	1	1	1,72	0,0001	0,0007	Molecules associated with elastic fibres
High	Q8R404	MICOS complex subunit MIC13 OS=Mus musculus OX=10090 GN=Micos13 PE=1 SV=1	Micos13	3	3	1,70	0,0000	0,0000	
High	P00416	Cytochrome c oxidase subunit 3 OS=Mus musculus OX=10090 GN=mt-Co3 PE=1 SV=2	mt-Co3	1	1	1,70	0,0001	0,0011	Cytoprotection by HMOX1; TP53 Regulates Metabolic Genes; Respiratory electron transport
Medium	Q8JZV7	N-acetylglucosamine-6-phosphate deacetylase OS=Mus musculus OX=10090 GN=Amdhd2 PE=1 SV=1	Amdhd2	1	1	1,70	0,0001	0,0010	Synthesis of UDP-N-acetyl-glucosamine
High	Q9DB15	39S ribosomal protein L12, mitochondrial OS=Mus musculus OX=10090 GN=Mrpl12 PE=1 SV=2	Mrpl12	2	2	1,68	0,0000	0,0000	**Mitochondrial translation elongation; Mitochondrial translation termination**
High	Q61781	Keratin, type I cytoskeletal 14 OS=Mus musculus OX=10090 GN=Krt14 PE=1 SV=2	Krt14	23	6	1,66	0,0022	0,0183	Formation of the cornified envelope; Type I hemidesmosome assembly
High	Q9CPX8	Cytochrome b-c1 complex subunit 10 OS=Mus musculus OX=10090 GN=Uqcr11 PE=1 SV=1	Uqcr11	1	1	1,62	0,0000	0,0003	**Respiratory electron transport**
High	Q00623	Apolipoprotein A-I OS=Mus musculus OX=10090 GN=Apoa1 PE=1 SV=2	Apoa1	13	13	1,61	0,0005	0,0050	**Statin pathway; PPAR signaling pathway**
High	P12787	Cytochrome c oxidase subunit 5A, mitochondrial OS=Mus musculus OX=10090 GN=Cox5a PE=1 SV=2	Cox5a	4	4	1,61	0,0005	0,0050	**Respiratory electron transport; Cytoprotection by HMOX1; TP53 Regulates Metabolic Genes**
High	Q61599	Rho GDP-dissociation inhibitor 2 OS=Mus musculus OX=10090 GN=Arhgdib PE=1 SV=3	Arhgdib	3	3	1,60	0,0006	0,0051	RHOA GTPase cycle; CDC42 GTPase cycle; RAC1 GTPase cycle; RHOG GTPase cycle; RHOH GTPase cycle; F
High	Q07456	Protein AMBP OS=Mus musculus OX=10090 GN=Ambp PE=1 SV=2	Ambp	2	2	1,59	0,0021	0,0180	Scavenging of heme from plasma
Medium	Q6QD59	Vesicle transport protein SEC20 OS=Mus musculus OX=10090 GN=Bnip1 PE=1 SV=1	Bnip1	1	1	1,59	0,0007	0,0067	COPI-dependent Golgi-to-ER retrograde traffic
High	Q8VD62	UPF0696 protein C11orf68 homolog OS=Mus musculus OX=10090 GN=Bles03 PE=1 SV=2	Bles03	1	1	1,58	0,0000	0,0002	
High	Q99LY9	NADH dehydrogenase [ubiquinone] iron-sulfur protein 5 OS=Mus musculus OX=10090 GN=Ndufs5 PE=1 SV=3	Ndufs5	3	3	1,57	0,0000	0,0002	**Complex I biogenesis**
High	P56391	Cytochrome c oxidase subunit 6B1 OS=Mus musculus OX=10090 GN=Cox6b1 PE=1 SV=2	Cox6b1	5	5	1,57	0,0012	0,0102	**Electron transport chain**
High	Q9JK38	Glucosamine 6-phosphate N-acetyltransferase OS=Mus musculus OX=10090 GN=Gnpnat1 PE=1 SV=1	Gnpnat1	2	2	1,55	0,0060	0,0460	**Synthesis of UDP-N-acetyl-glucosamine**
High	Q60936	Atypical kinase COQ8A, mitochondrial OS=Mus musculus OX=10090 GN=Coq8a PE=1 SV=2	Coq8a	6	6	1,55	0,0040	0,0316	
High	O35490	Betaine--homocysteine S-methyltransferase 1 OS=Mus musculus OX=10090 GN=Bhmt PE=1 SV=1	Bhmt	5	5	1,54	0,0000	0,0004	**Sulfur amino acid metabolism; Choline catabolism**
High	Q64433	10 kDa heat shock protein, mitochondrial OS=Mus musculus OX=10090 GN=Hspe1 PE=1 SV=2	Hspe1	3	3	1,52	0,0009	**0,0084**	RHOG GTPase cycle
High	Q9D855	Cytochrome b-c1 complex subunit 7 OS=Mus musculus OX=10090 GN=Uqcrb PE=1 SV=3	Uqcrb	5	5	1,51	0,0029	0,0236	Respiratory electron transport
High	Q91X72	Hemopexin OS=Mus musculus OX=10090 GN=Hpx PE=1 SV=2	Hpx	21	21	1,50	0,0035	0,0280	Scavenging of heme from plasma
High	Q9D2R6	Cytochrome c oxidase assembly factor 3 homolog, mitochondrial OS=Mus musculus OX=10090 GN=Coa3 PE=1 SV=1	Coa3	1	1	1,49	0,0030	0,0242	
High	Q9D8T7	SRA stem-loop-interacting RNA-binding protein, mitochondrial OS=Mus musculus OX=10090 GN=Slirp PE=1 SV=2	Slirp	2	2	1,49	0,0019	0,0161	
High	P29699	Alpha-2-HS-glycoprotein OS=Mus musculus OX=10090 GN=Ahsg PE=1 SV=1	Ahsg	9	9	1,49	0,0040	0,0321	Neutrophil degranulation
High	Q80UM7	Mannosyl-oligosaccharide glucosidase OS=Mus musculus OX=10090 GN=Mogs PE=1 SV=1	Mogs	1	1	1,49	0,0083	0,0607	
High	Q9ESB3	Histidine-rich glycoprotein OS=Mus musculus OX=10090 GN=Hrg PE=1 SV=2	Hrg	14	14	1,48	0,0046	0,0364	Dissolution of Fibrin Clot; Platelet degranulation
High	Q9QXD6	Fructose-1,6-bisphosphatase 1 OS=Mus musculus OX=10090 GN=Fbp1 PE=1 SV=3	Fbp1	2	2	1,47	0,0096	0,0693	**Glycolysis and gluconeogenesis**
High	Q8VCM7	Fibrinogen gamma chain OS=Mus musculus OX=10090 GN=Fgg PE=1 SV=1	Fgg	18	18	1,46	0,0059	0,0450	
High	P99028	Cytochrome b-c1 complex subunit 6, mitochondrial OS=Mus musculus OX=10090 GN=Uqcrh PE=1 SV=2	Uqcrh	4	4	1,46	0,0010	0,0089	**Electron transport chain**
High	O55028	[3-methyl-2-oxobutanoate dehydrogenase [lipoamide]] kinase, mitochondrial OS=Mus musculus OX=10090 GN=Bckdk PE=1 SV=1	Bckdk	2	2	1,46	0,0096	0,0693	Branched-chain amino acid catabolism
High	A6BLY7	Keratin, type I cytoskeletal 28 OS=Mus musculus OX=10090 GN=Krt28 PE=1 SV=1	Krt28	5	1	1,45	0,0070	0,0524	Formation of the cornified envelope
High	Q9R0H5	Keratin, type II cytoskeletal 71 OS=Mus musculus OX=10090 GN=Krt71 PE=1 SV=1	Krt71	11	5	1,45	0,0061	0,0463	Formation of the cornified envelope
High	Q61207	Prosaposin OS=Mus musculus OX=10090 GN=Psap PE=1 SV=2	Psap	7	7	1,45	0,0005	0,0046	Glycosphingolipid metabolism; Platelet degranulation ; G alpha (i) signalling events
High	P01898	H-2 class I histocompatibility antigen, Q10 alpha chain OS=Mus musculus OX=10090 GN=H2-Q10 PE=1 SV=3	H2-Q10	8	5	1,45	0,0005	0,0050	
High	O35215	D-dopachrome decarboxylase OS=Mus musculus OX=10090 GN=Ddt PE=1 SV=3	Ddt	2	2	1,45	0,0065	0,0491	
High	Q9CZB0	Succinate dehydrogenase cytochrome b560 subunit, mitochondrial OS=Mus musculus OX=10090 GN=Sdhc PE=1 SV=1	Sdhc	3	3	1,44	0,0087	0,0631	**Electron transport chain; TCA cycle**
High	Q9R0P9	Ubiquitin carboxyl-terminal hydrolase isozyme L1 OS=Mus musculus OX=10090 GN=Uchl1 PE=1 SV=1	Uchl1	5	5	1,44	0,0007	0,0063	UCH proteinases
High	P43025	Tetranectin OS=Mus musculus OX=10090 GN=Clec3b PE=1 SV=2	Clec3b	3	3	1,43	0,0221	0,1367	Platelet degranulation
High	P46412	Glutathione peroxidase 3 OS=Mus musculus OX=10090 GN=Gpx3 PE=1 SV=2	Gpx3	6	6	1,43	0,0099	0,0709	Detoxification of Reactive Oxygen Species
High	Q61414	Keratin, type I cytoskeletal 15 OS=Mus musculus OX=10090 GN=Krt15 PE=1 SV=2	Krt15	11	3	1,43	0,0084	0,0612	Formation of the cornified envelope
High	Q99LP6	GrpE protein homolog 1, mitochondrial OS=Mus musculus OX=10090 GN=Grpel1 PE=1 SV=1	Grpel1	7	7	1,43	0,0008	0,0075	
High	Q64521	Glycerol-3-phosphate dehydrogenase, mitochondrial OS=Mus musculus OX=10090 GN=Gpd2 PE=1 SV=2	Gpd2	34	34	1,43	0,0102	0,0727	Synthesis of PA; Triglyceride catabolism
Medium	Q8BZ33	Tensin-4 OS=Mus musculus OX=10090 GN=Tns4 PE=2 SV=2	Tns4	1	1	1,43	0,0016	0,0140	MET interacts with TNS proteins
High	P21614	Vitamin D-binding protein OS=Mus musculus OX=10090 GN=Gc PE=1 SV=2	Gc	17	17	1,42	0,0108	0,0752	Vitamin D (calciferol) metabolism
High	P20918	Plasminogen OS=Mus musculus OX=10090 GN=Plg PE=1 SV=3	Plg	27	27	1,42	0,0113	0,0780	Platelet degranulation ; Signaling by PDGF; LDL remodeling; Dissolution of Fibrin Clot; Activation of M
High	Q62422	Osteoclast-stimulating factor 1 OS=Mus musculus OX=10090 GN=Ostf1 PE=1 SV=2	Ostf1	1	1	1,42	0,0151	0,0991	Neutrophil degranulation
High	P52503	NADH dehydrogenase [ubiquinone] iron-sulfur protein 6, mitochondrial OS=Mus musculus OX=10090 GN=Ndufs6 PE=1 SV=2	Ndufs6	1	1	1,42	0,0148	0,0979	**Complex I biogenesis**
High	P19783	Cytochrome c oxidase subunit 4 isoform 1, mitochondrial OS=Mus musculus OX=10090 GN=Cox4i1 PE=1 SV=2	Cox4i1	7	7	1,42	0,0122	0,0833	**Respiratory electron transport; Cytoprotection by HMOX1; TP53 Regulates Metabolic Genes**
High	Q99JY0	Trifunctional enzyme subunit beta, mitochondrial OS=Mus musculus OX=10090 GN=Hadhb PE=1 SV=1	Hadhb	18	18	1,41	0,0136	0,0909	**Beta oxidation of decanoyl-CoA to octanoyl-CoA-CoA**
High	Q9JLT4	Thioredoxin reductase 2, mitochondrial OS=Mus musculus OX=10090 GN=Txnrd2 PE=1 SV=4	Txnrd2	8	7	1,41	0,0013	0,0113	Detoxification of Reactive Oxygen Species
Medium	P04627	Serine/threonine-protein kinase A-Raf OS=Mus musculus OX=10090 GN=Araf PE=1 SV=2	Araf	1	1	1,41	0,0361	0,2029	**MAP2K and MAPK activation; Negative regulation of MAPK pathway; RAF activation**
High	Q9Z1P6	NADH dehydrogenase [ubiquinone] 1 alpha subcomplex subunit 7 OS=Mus musculus OX=10090 GN=Ndufa7 PE=1 SV=3	Ndufa7	5	5	1,40	0,0016	0,0136	**Complex I biogenesis**
High	Q9WUM5	Succinate--CoA ligase [ADP/GDP-forming] subunit alpha, mitochondrial OS=Mus musculus OX=10090 GN=Suclg1 PE=1 SV=4	Suclg1	8	8	1,40	0,0155	0,1011	**Citric acid cycle (TCA cycle)**
High	Q99KI0	Aconitate hydratase, mitochondrial OS=Mus musculus OX=10090 GN=Aco2 PE=1 SV=1	Aco2	36	36	1,40	0,0161	0,1048	**Citric acid cycle (TCA cycle)**
High	Q9DBB9	Carboxypeptidase N subunit 2 OS=Mus musculus OX=10090 GN=Cpn2 PE=1 SV=2	Cpn2	4	4	1,40	0,0219	0,1361	Regulation of Complement cascade
High	Q921I1	Serotransferrin OS=Mus musculus OX=10090 GN=Tf PE=1 SV=1	Tf	40	38	1,39	0,0169	0,1092	Cargo recognition for clathrin-mediated endocytosis
High	Q61555	Fibrillin-2 OS=Mus musculus OX=10090 GN=Fbn2 PE=1 SV=2	Fbn2	5	2	1,39	0,0020	0,0167	Degradation of the extracellular matrix; Molecules associated with elastic fibres
High	Q8VE38	Oxidoreductase NAD-binding domain-containing protein 1 OS=Mus musculus OX=10090 GN=Oxnad1 PE=1 SV=2	Oxnad1	1	1	1,39	0,0368	0,2049	
High	Q8BWT1	3-ketoacyl-CoA thiolase, mitochondrial OS=Mus musculus OX=10090 GN=Acaa2 PE=1 SV=3	Acaa2	21	21	1,39	0,0183	0,1168	**Fatty acid biosynthesis**
High	Q3URD3	Sarcolemmal membrane-associated protein OS=Mus musculus OX=10090 GN=Slmap PE=1 SV=2	Slmap	1	1	1,39	0,0192	0,1220	
High	Q8VED5	Keratin, type II cytoskeletal 79 OS=Mus musculus OX=10090 GN=Krt79 PE=1 SV=2	Krt79	7	1	1,38	0,0195	0,1236	
Medium	P50608	Fibromodulin OS=Mus musculus OX=10090 GN=Fmod PE=2 SV=1	Fmod	1	1	1,38	0,0448	0,2414	
High	Q9D023	Mitochondrial pyruvate carrier 2 OS=Mus musculus OX=10090 GN=Mpc2 PE=1 SV=1	Mpc2	4	4	1,38	0,0200	0,1261	**Glycolysis and gluconeogenesis**
High	Q3ULW8	Protein mono-ADP-ribosyltransferase PARP3 OS=Mus musculus OX=10090 GN=Parp3 PE=2 SV=1	Parp3	3	3	1,38	0,0473	0,2504	
High	O89023	Tripeptidyl-peptidase 1 OS=Mus musculus OX=10090 GN=Tpp1 PE=1 SV=2	Tpp1	3	3	1,38	0,0023	0,0188	
High	Q91WP6	Serine protease inhibitor A3N OS=Mus musculus OX=10090 GN=Serpina3n PE=1 SV=1	Serpina3n	6	4	1,37	0,0028	0,0228	
High	O88668	Protein CREG1 OS=Mus musculus OX=10090 GN=Creg1 PE=1 SV=1	Creg1	1	1	1,37	0,0149	0,0980	
High	P03953	Complement factor D OS=Mus musculus OX=10090 GN=Cfd PE=1 SV=1	Cfd	3	3	1,37	0,0239	0,1471	**Adipogenesis genes**
Medium	Q9CPZ8	COX assembly mitochondrial protein homolog OS=Mus musculus OX=10090 GN=Cmc1 PE=1 SV=1	Cmc1	1	1	1,37	0,0327	0,1862	
High	Q91X52	L-xylulose reductase OS=Mus musculus OX=10090 GN=Dcxr PE=1 SV=2	Dcxr	2	1	1,37	0,0142	0,0949	Formation of xylulose-5-phosphate
High	Q06890	Clusterin OS=Mus musculus OX=10090 GN=Clu PE=1 SV=1	Clu	10	10	1,37	0,0239	0,1471	Platelet degranulation ; Regulation of Complement cascade; Antimicrobial peptides; Terminal pathway
High	Q99MQ4	Asporin OS=Mus musculus OX=10090 GN=Aspn PE=1 SV=1	Aspn	12	12	1,37	0,0249	0,1518	
High	Q9WUU7	Cathepsin Z OS=Mus musculus OX=10090 GN=Ctsz PE=1 SV=1	Ctsz	6	6	1,37	0,0031	0,0251	COPII-mediated vesicle transport; Metabolism of Angiotensinogen to Angiotensins; Cargo concentratic
High	P59279	Ras-related protein Rab-2B OS=Mus musculus OX=10090 GN=Rab2b PE=1 SV=1	Rab2b	6	1	1,37	0,0111	0,0772	RAB geranylgeranylation
Medium	Q8CIM3	D-2-hydroxyglutarate dehydrogenase, mitochondrial OS=Mus musculus OX=10090 GN=D2hgdh PE=1 SV=3	D2hgdh	1	1	1,36	0,0250	0,1518	Interconversion of 2-oxoglutarate and 2-hydroxyglutarate
Medium	Q64008	Ras-related protein Rab-34 OS=Mus musculus OX=10090 GN=Rab34 PE=1 SV=2	Rab34	1	1	1,36	0,0033	0,0264	RAB geranylgeranylation
High	P06728	Apolipoprotein A-IV OS=Mus musculus OX=10090 GN=Apoa4 PE=1 SV=3	Apoa4	18	18	1,36	0,0261	0,1570	Retinoid metabolism and transport; Chylomicron assembly; Chylomicron remodeling
High	Q9CQ91	NADH dehydrogenase [ubiquinone] 1 alpha subcomplex subunit 3 OS=Mus musculus OX=10090 GN=Ndufa3 PE=1 SV=1	Ndufa3	2	2	1,36	0,0271	0,1605	**Complex I biogenesis**
High	P00397	Cytochrome c oxidase subunit 1 OS=Mus musculus OX=10090 GN=Mtco1 PE=1 SV=2	Mtco1	3	3	1,36	0,0272	0,1607	**Cytoprotection by HMOX1; TP53 Regulates Metabolic Genes; Respiratory electron transport**
Medium	Q6V595	Kelch-like protein 6 OS=Mus musculus OX=10090 GN=Klhl6 PE=2 SV=2	Klhl6	1	1	1,36	0,0269	0,1599	
High	Q99JX4	Eukaryotic translation initiation factor 3 subunit M OS=Mus musculus OX=10090 GN=Eif3m PE=1 SV=1	Eif3m	2	2	1,36	0,0038	0,0306	Formation of a pool of free 40S subunits; GTP hydrolysis and joining of the 60S ribosomal subunit
High	P28665	Murinoglobulin-1 OS=Mus musculus OX=10090 GN=Mug1 PE=1 SV=3	Mug1	38	38	1,36	0,0281	0,1649	
High	Q9D958	Signal peptidase complex subunit 1 OS=Mus musculus OX=10090 GN=Spcs1 PE=2 SV=3	Spcs1	1	1	1,35	0,0036	0,0287	Synthesis, secretion, and deacylation of Ghrelin
High	Q62264	Thyroid hormone-inducible hepatic protein OS=Mus musculus OX=10090 GN=Thrsp PE=1 SV=1	Thrsp	5	5	1,35	0,0308	0,1777	**Carnitine metabolism**
High	Q9CPP6	NADH dehydrogenase [ubiquinone] 1 alpha subcomplex subunit 5 OS=Mus musculus OX=10090 GN=Ndufa5 PE=1 SV=3	Ndufa5	5	5	1,35	0,0326	0,1862	Oxidative phosphorylation; Electron transport chain
High	P19536	Cytochrome c oxidase subunit 5B, mitochondrial OS=Mus musculus OX=10090 GN=Cox5b PE=1 SV=1	Cox5b	2	2	1,35	0,0327	0,1862	
High	Q8R0W0	Epiplakin OS=Mus musculus OX=10090 GN=Eppk1 PE=1 SV=2	Eppk1	2	1	1,35	0,0067	0,0499	EGFR1 signaling pathway
High	P49290	Eosinophil peroxidase OS=Mus musculus OX=10090 GN=Epx PE=1 SV=2	Epx	7	7	1,35	0,0146	0,0970	Neutrophil degranulation
High	Q9DC69	NADH dehydrogenase [ubiquinone] 1 alpha subcomplex subunit 9, mitochondrial OS=Mus musculus OX=10090 GN=Ndufa9 PE=1 SV=2	Ndufa9	15	15	1,34	0,0351	0,1985	**Complex I biogenesis**
High	A1L317	Keratin, type I cytoskeletal 24 OS=Mus musculus OX=10090 GN=Krt24 PE=2 SV=2	Krt24	2	1	1,34	0,0394	0,2163	
High	P10639	Thioredoxin OS=Mus musculus OX=10090 GN=Txn PE=1 SV=3	Txn	2	2	1,34	0,0357	0,2014	Detoxification of Reactive Oxygen Species; Oxidative Stress Induced Senescence; Protein repair; The NLI
High	Q9CRB9	MICOS complex subunit Mic19 OS=Mus musculus OX=10090 GN=Chchd3 PE=1 SV=1	Chchd3	6	6	1,34	0,0385	0,2126	
High	P97315	Cysteine and glycine-rich protein 1 OS=Mus musculus OX=10090 GN=Csrp1 PE=1 SV=3	Csrp1	3	3	1,33	0,0368	0,2049	
High	Q9D6R2	Isocitrate dehydrogenase [NAD] subunit alpha, mitochondrial OS=Mus musculus OX=10090 GN=Idh3a PE=1 SV=1	Idh3a	15	15	1,33	0,0395	0,2166	**Citric acid cycle (TCA cycle)**
Medium	P97929	Breast cancer type 2 susceptibility protein homolog OS=Mus musculus OX=10090 GN=Brca2 PE=1 SV=2	Brca2	1	1	1,33	0,0058	0,0450	
High	Q61554	Fibrillin-1 OS=Mus musculus OX=10090 GN=Fbn1 PE=1 SV=2	Fbn1	90	87	1,33	0,0411	0,2241	
High	Q9DCJ5	NADH dehydrogenase [ubiquinone] 1 alpha subcomplex subunit 8 OS=Mus musculus OX=10090 GN=Ndufa8 PE=1 SV=3	Ndufa8	5	5	1,33	0,0434	0,2361	**Complex I biogenesis**
High	Q08189	Protein-glutamine gamma-glutamyltransferase E OS=Mus musculus OX=10090 GN=Tgm3 PE=1 SV=2	Tgm3	1	1	1,33	0,0083	0,0607	
High	Q9QZZ6	Dermatopontin OS=Mus musculus OX=10090 GN=Dpt PE=1 SV=1	Dpt	5	5	1,33	0,0450	0,2421	
High	P70404	Isocitrate dehydrogenase [NAD] subunit gamma 1, mitochondrial OS=Mus musculus OX=10090 GN=Idh3g PE=1 SV=1	Idh3g	10	10	1,32	0,0448	0,2414	**Citric acid cycle (TCA cycle)**
High	P35487	Pyruvate dehydrogenase E1 component subunit alpha, testis-specific form, mitochondrial OS=Mus musculus OX=10090 GN=Pdha2 PE=1 SV=1	Pdha2	1	1	1,32	0,0458	0,2459	**Glycolysis and gluconeogenesis; Acetylcholine synthesis; TCA cycle**
High	P43276	Histone H1.5 OS=Mus musculus OX=10090 GN=H1-5 PE=1 SV=2	H1-5	2	2	1,32	0,0073	0,0546	Formation of Senescence-Associated Heterochromatin Foci (SAHF); Apoptosis induced DNA fragmentat
High	P09671	Superoxide dismutase [Mn], mitochondrial OS=Mus musculus OX=10090 GN=Sod2 PE=1 SV=3	Sod2	9	9	1,32	0,0469	0,2501	**Detoxification of Reactive Oxygen Species; Transcriptional activation of mitochondrial biogenesis**
High	Q9D2G2	Dihydrolipoyllysine-residue succinyltransferase component of 2-oxoglutarate dehydrogenase complex, mitochondrial OS=Mus musculus OX=10090 GN=Dlst PE=1 SV=1	Dlst	10	10	1,32	0,0475	0,2513	**Glyoxylate metabolism and glycine degradation; Lysine catabolism; Citric acid cycle (TCA cycle)**
High	P03893	NADH-ubiquinone oxidoreductase chain 2 OS=Mus musculus OX=10090 GN=Mtnd2 PE=1 SV=2	mt-Nd2	2	2	1,32	0,0085	0,0619	**Complex I biogenesis**
High	O35658	Complement component 1 Q subcomponent-binding protein, mitochondrial OS=Mus musculus OX=10090 GN=C1qbp PE=1 SV=1	C1qbp	2	2	1,32	0,0251	0,1518	RHOA GTPase cycle; RHOC GTPase cycle; Intrinsic Pathway of Fibrin Clot Formation
High	Q8K4F5	Protein ABHD11 OS=Mus musculus OX=10090 GN=Abhd11 PE=1 SV=1	Abhd11	1	1	1,31	0,0146	0,0970	
High	Q02105	Complement C1q subcomponent subunit C OS=Mus musculus OX=10090 GN=C1qc PE=1 SV=2	C1qc	1	1	1,31	0,0487	0,2557	Regulation of Complement cascade; Initial triggering of complement; Classical antibody-mediated com
High	Q9WV54	Acid ceramidase OS=Mus musculus OX=10090 GN=Asah1 PE=1 SV=1	Asah1	9	9	1,31	0,0094	0,0678	Neutrophil degranulation; Glycosphingolipid metabolism
High	Q99LD8	N(G),N(G)-dimethylarginine dimethylaminohydrolase 2 OS=Mus musculus OX=10090 GN=Ddah2 PE=1 SV=1	Ddah2	3	3	1,31	0,0289	0,1679	**eNOS activation**
High	P02762	Major urinary protein 6 OS=Mus musculus OX=10090 GN=Mup6 PE=1 SV=2	Mup6	10	2	1,30	0,0471	0,2501	
High	Q60960	Importin subunit alpha-5 OS=Mus musculus OX=10090 GN=Kpna1 PE=1 SV=2	Kpna1	2	2	1,30	0,0105	0,0733	Interferon alpha/beta signaling; Assembly of the ORC complex at the origin of replication; Apoptosis in
High	Q9D8B4	NADH dehydrogenase [ubiquinone] 1 alpha subcomplex subunit 11 OS=Mus musculus OX=10090 GN=Ndufa11 PE=1 SV=2	Ndufa11	3	3	1,30	0,0107	0,0744	**Complex I biogenesis**
High	Q924L1	LETM1 domain-containing protein 1 OS=Mus musculus OX=10090 GN=Letmd1 PE=1 SV=1	Letmd1	9	9	1,30	0,0304	0,1760	
High	Q9QYR9	Acyl-coenzyme A thioesterase 2, mitochondrial OS=Mus musculus OX=10090 GN=Acot2 PE=1 SV=2	Acot2	11	11	1,30	0,0372	0,2069	**Peroxisomal protein import; Mitochondrial Fatty Acid Beta-Oxidation**
High	Q62433	Protein NDRG1 OS=Mus musculus OX=10090 GN=Ndrg1 PE=1 SV=1	Ndrg1	3	3	1,30	0,0459	0,2463	
High	Q61391	Neprilysin OS=Mus musculus OX=10090 GN=Mme PE=1 SV=3	Mme	2	2	0,01	0,0000	0,0000	Neutrophil degranulation; Metabolism of Angiotensinogen to Angiotensins
Medium	Q9D6N1	Carbonic anhydrase 13 OS=Mus musculus OX=10090 GN=Ca13 PE=1 SV=1	Ca13	1	1	0,01	0,0000	0,0000	Reversible hydration of carbon dioxide
Medium	Q61550	Double-strand-break repair protein rad21 homolog OS=Mus musculus OX=10090 GN=Rad21 PE=1 SV=3	Rad21	1	1	0,01	0,0000	0,0000	Separation of Sister Chromatids; Resolution of Sister Chromatid Cohesion; SUMOylation of DNA damag
High	Q9WV35	C->U-editing enzyme APOBEC-2 OS=Mus musculus OX=10090 GN=Apobec2 PE=1 SV=1	Apobec2	4	4	0,20	0,0000	0,0000	Formation of the Editosome
High	P20801	Troponin C, skeletal muscle OS=Mus musculus OX=10090 GN=Tnnc2 PE=1 SV=2	Tnnc2	7	7	0,21	0,0000	0,0000	Striated Muscle Contraction
High	Q9WUD1	STIP1 homology and U box-containing protein 1 OS=Mus musculus OX=10090 GN=Stub1 PE=1 SV=1	Stub1	1	1	0,35	0,0000	0,0000	Antigen processing: Ubiquitination & Proteasome degradation; Regulation of TNFR1 signaling; Downre
High	Q80ZS3	28S ribosomal protein S26, mitochondrial OS=Mus musculus OX=10090 GN=Mrps26 PE=1 SV=1	Mrps26	1	1	0,36	0,0000	0,0000	Mitochondrial translation elongation; Mitochondrial translation termination
High	Q5SX39	Myosin-4 OS=Mus musculus OX=10090 GN=Myh4 PE=2 SV=1	Myh4	128	32	0,36	0,0000	0,0000	other biological processes
High	Q8K021	Secretory carrier-associated membrane protein 1 OS=Mus musculus OX=10090 GN=Scamp1 PE=1 SV=1	Scamp1	1	1	0,38	0,0000	0,0000	Neutrophil degranulation
High	Q9WUK2	Eukaryotic translation initiation factor 4H OS=Mus musculus OX=10090 GN=Eif4h PE=1 SV=3	Eif4h	1	1	0,41	0,0000	0,0000	Translation factors; mRNA processing
High	E9Q9A9	2'-5'-oligoadenylate synthase 2 OS=Mus musculus OX=10090 GN=Oas2 PE=1 SV=1	Oas2	1	1	0,41	0,0000	0,0000	mRNA processing
High	P05784	Keratin, type I cytoskeletal 18 OS=Mus musculus OX=10090 GN=Krt18 PE=1 SV=5	Krt18	5	2	0,42	0,0000	0,0000	EGFR1 signaling pathway
High	Q8C196	Carbamoyl-phosphate synthase [ammonia], mitochondrial OS=Mus musculus OX=10090 GN=Cps1 PE=1 SV=2	Cps1	28	27	0,43	0,0000	0,0000	Urea cycle
High	O70622	Reticulon-2 OS=Mus musculus OX=10090 GN=Rtn2 PE=1 SV=1	Rtn2	2	2	0,43	0,0000	0,0000	
High	P32848	Parvalbumin alpha OS=Mus musculus OX=10090 GN=Pvalb PE=1 SV=3	Pvalb	8	8	0,45	0,0000	0,0000	
Medium	Q3UMB9	WASH complex subunit 4 OS=Mus musculus OX=10090 GN=Washc4 PE=1 SV=2	Washc4	1	1	0,46	0,0000	0,0000	
High	A2ASS6	Titin OS=Mus musculus OX=10090 GN=Ttn PE=1 SV=1	Ttn	730	730	0,47	0,0000	0,0000	
Medium	Q70IV5	Synemin OS=Mus musculus OX=10090 GN=Synm PE=1 SV=2	Synm	1	1	0,47	0,0000	0,0001	
High	Q9WUB3	Glycogen phosphorylase, muscle form OS=Mus musculus OX=10090 GN=Pygm PE=1 SV=3	Pygm	45	34	0,48	0,0000	0,0000	Glycogen breakdown (glycogenolysis)
High	Q9Z223	Molybdopterin synthase catalytic subunit OS=Mus musculus OX=10090 GN=Mocs2 PE=1 SV=3	Mocs2	1	1	0,49	0,0000	0,0001	
High	P70402	Myosin-binding protein H OS=Mus musculus OX=10090 GN=Mybph PE=2 SV=2	Mybph	8	8	0,49	0,0000	0,0000	G13 signaling pathway

3.10 Adip^{Cre+}ADAM17 mice demonstrated increased Body weight gain upon 45% HFD.

To examine the impact of adipocyte ADAM17 deletion on energy homeostasis, upon exposure to obesogenic diet, we fed Adip^{Cre+}ADAM17 and Adip^{Cre-}WT, a 45% fat HFD for 12 weeks.

By the end of the study Adip^{Cre+}ADAM17KO male mice gained more weight than Adip^{Cre-}WT, starting from 8 weeks on HFD (Fig. 19a). Of note, developmental differences could not have accounted for this difference, since the mice were fed a HFD, starting from 14 weeks of age and up to that age, we observed no body weight differences related to the genotypes (Fig. 19a). Interestingly, upon HFD, Adip^{Cre+}ADAM17KO showed bigger inguinal and mesenteric fats, whereas epi-dydimal fat was smaller (Fig. 19b), suggesting potentially a differential role of ADAM17, across fat depots.

We examine the glucose tolerance profile of the Adip^{Cre+}ADAM17KO mice and found similar rate of glucose blood clearance in response to a glucose ip injection (intraperitoneal glucose tolerance test- ipgtt) (Fig. 19c), as well as similar increase of plasma insulin in response to the ipgtt (Fig. 19d). In addition, there was no difference in gluconeogenesis in response to a pyruvate tolerance test (PTT) (Fig. 19e). We also measured serum parameters and found that Adip^{Cre+}ADAM17KO mice showed higher serum total cholesterol and HDL (Fig. 19f), whereas LDL (Fig. 19f) and triglycerides (Fig, 19f) were not different between the genotypes.

On chow diet, we found no differences on glucose tolerance in 8 weeks, 15 weeks, and 50 weeks old male mice (Fig. 20a-c). In addition, there were no body weight differences between the genotypes in any of those ages (data not shown). Moreover, we observed no difference in glucose induced secretion of insulin or C-peptide, during an IPGTT (Fig. 20d-e). During an ITT test, we found that the hypoglycemic response to insulin injection was higher in the Adip^{Cre+}ADAM17KO compared to Adip^{Cre-}WT mice (Fig. 20f). This advance in the post hypoglycemic recovery of blood glucose suggests an enhanced hepatic glucose production (HGP). Finally, we also challenged the mice with an oral glucose tolerance test

(OGTT) and found no difference between genotypes in terms of blood glucose clearance (Fig. 20g), Plasma insulin (Fig. 20h) and C-peptide (Fig. 20i) in response to the OGTT.

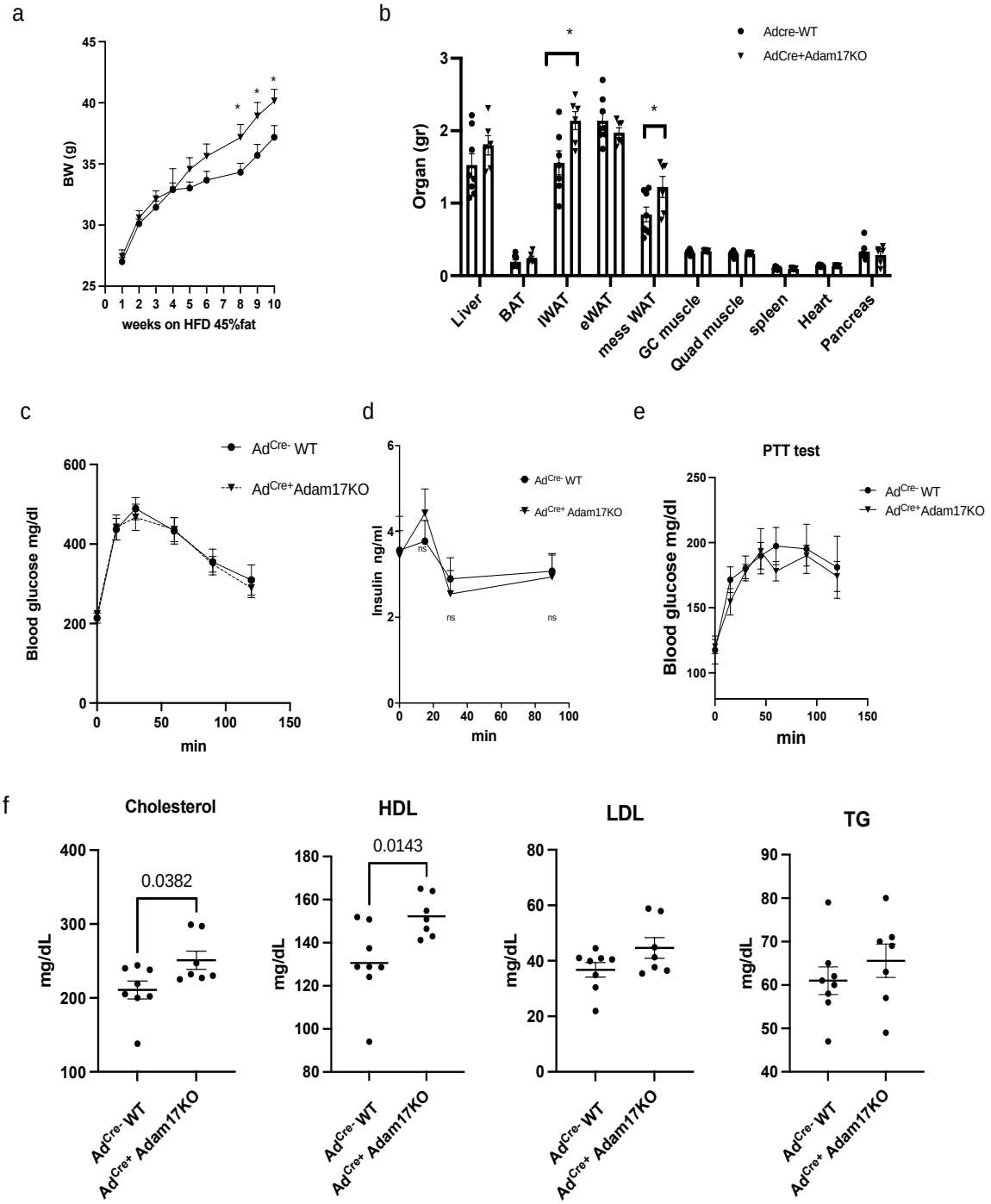

Figure 19: Adip^{Cre+}ADAM17KO mice gain more weight on HFD and show hypercholesterolemia.

Adip^{Cre+}ADAM17KO and Adip^{Cre-}WT male mice were fed 45% fat HFD for 12 weeks. (a) BW measurement during HFD feeding, (b) Tissue weights at the end of HFD feeding, (c, d) IPGTT and insulin levels during the IPGTT measured whiles mice were on HFD, (e) PTT during HFD feeding and (f) serum parameters (cholesterol, LDL and TG) at the end of the HFD feeding. Data are shown as mean± SEM. * is p-value <0.05 calculated by a student's t-test.

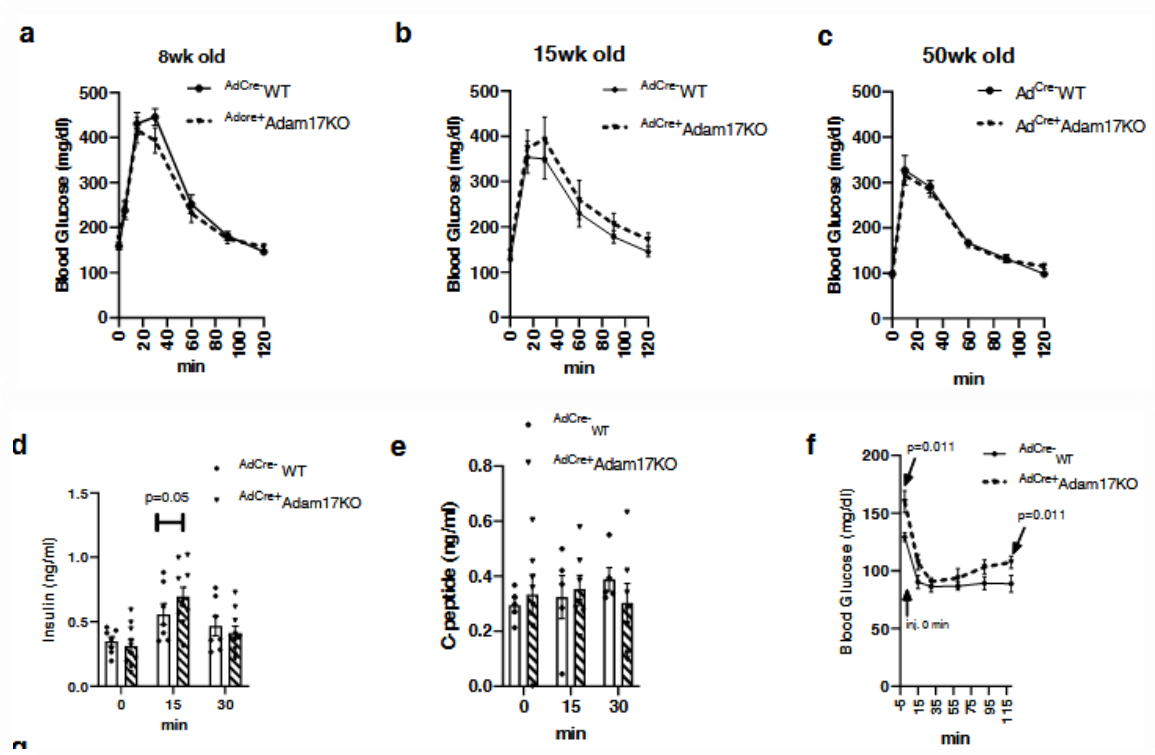

Figure 20: Glucose homeostasis is not altered by adipocyte ADAM17 deletion, upon chow diet.

(a) IPGTT on male mice following 8 weeks of chow, (b) IPGTT on 15 weeks old male mice, (c) IPGTT on 50 weeks old male mice, (d)glucose induced insulin secretion and (e) c-peptide during the IPGTT, (f)ITT performed in adult male mice 8-.12 weeks old. (g)OGTT performed in adult male mice 8-12 weeks old, (h) glucose induced insulin and (i) c-peptide during OGTT. Data are shown as mean± SEM. * is p-value < 0.05 calculated by a student's t-test.

3.11 Adip^{Cre+}ADAM17 KO mice rely on glycolytic pathways rather than lipolytic ones during prolonged fasting.

Driven by the enhanced hepatic glucose production (HGP) during ITT in the Adip^{Cre+}Adam1KO mice compared to Adip^{Cre-}WT mice, we questioned the ability of the Adip^{Cre+}ADAM17KO mice to regulate blood glucose during fasting, when the blood glucose levels depend on HGP. We observed that blood glucose was similar between Adip^{Cre+}ADAM17KO compared to Adip^{Cre-}WT mice after 2 h, 16 h and 24 h of fasting, although at prolonged fasting time, such as 24 h of fasting Adip^{Cre+}ADAM17KO mice tended to show lower blood glucose levels compared to Adip^{Cre-}WT controls but never became hypoglycemic (Fig. 21a). During a pyruvate tolerance test (PTT) in 16 h fasted mice, we observed higher blood glucose levels in Adip^{Cre+}ADAM17KO mice compared to Adip^{Cre-}WT mice, a result of higher liver glucose excursion (Fig. 21b-c). To understand if the gluconeogenic program was increased in the liver of Adip^{Cre+}ADAM17KO mice compared to Adip^{Cre-}WT mice, we performed a glycerol tolerance test, which revealed lower glucose production in response to glycerol delivery Adip^{Cre+}ADAM17KO mice compared to Adip^{Cre-}WT mice (Fig. 21d-e), suggesting that glycerol, physiologically derived by adipose tissue lipolysis is not a highly utilized substrate by Adip^{Cre+}ADAM17KO mice, during fasting. We found that liver of Adip^{Cre+}ADAM17KO mice had substantially more glycogen after 16hours of fasting compared to Adip^{Cre-}WT mice, where glycogen was almost depleted due to fasting (Fig. 21f). A trend to higher liver glycogen in the Adip^{Cre+}ADAM17KO mice, compared to Adip^{Cre-}WT mice was also found in the fed state (Fig. 21f). Next to higher glycogen, livers of Adip^{Cre+}ADAM17KO mice showed less fasting triglyceride content and higher triglyceride content in the fed state (Fig. 21g), but no difference in circulating NEFA or triglycerides (TG) (Fig. 21i). Other gluconeogenic substrates, such as alanine and lactate did not show major differences between the genotypes upon fasting conditions (Fig. 21j-k).

These findings suggest that Adip^{Cre+}ADAM17KO mouse livers are more anabolic compared to Adip^{Cre-}WT mouse livers storing more glycogen and triglycerides in the fed state. Glycogen is used the main substrate during fasting from the Adip^{Cre+}ADAM17KO mice, whereas liver TGs may be potentially used for liver energy

production, since there is no change in circulating TGs but a decrease in liver TG during fasting.

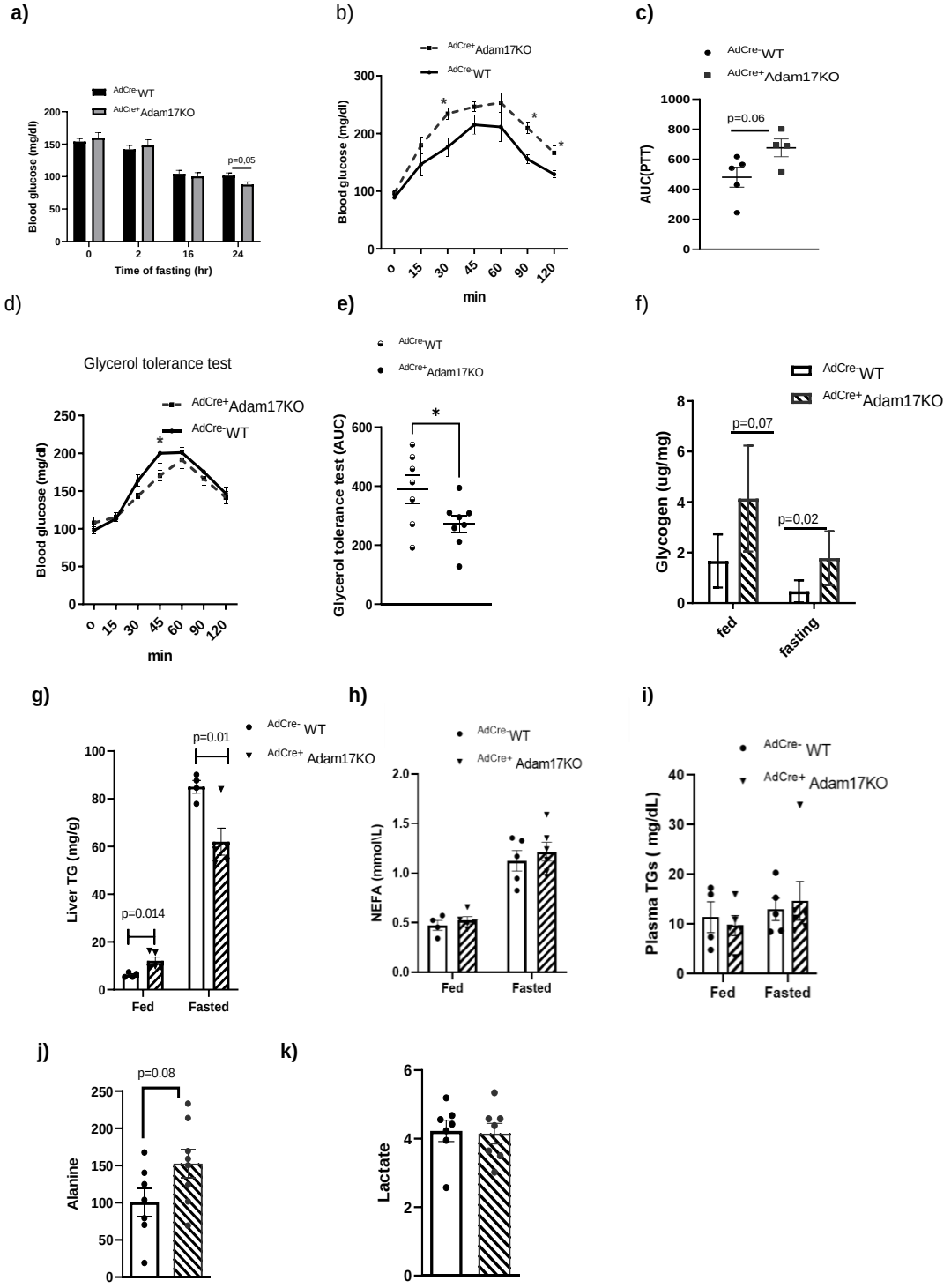

Figure 21: Increase glucose excursion and glycogen in the liver by PTT despite low hepatic TGs.

(a) Blood glucose after 2,16 and 24 hours of fasting in Adip^{Cre+}ADAM17KO and Adip^{Cre-}WT mice.(b) Pyruvate tolerance test (PTT),(c)and it´s area under curve for the PTT (AUC) performed in Adip^{Cre+}ADAM17KO mice and Adip^{Cre-}WT mice following 16 hours of overnight fasting.(d) Glycerol tolerance test (GlyTT),(e) and it´s area under curve for the GlyTT (AUC) performed in Ad^{Cre+}ADAM17KO mice and Ad^{Cre-}WT mice following 16 hours of overnight fasting. (f) Colorimetric measurement of glycogen level in the liver of Adip^{Cre+}ADAM17KO and Adip^{Cre-}WT mice during feeding and after 16 hours of overnight fast. (g) Liver triglyceride ((TGs) (mg/dL) levels measured in Adip^{Cre+}ADAM17KO mice and Adip^{Cre-}WT mice at the fed and after 16 hours of overnight fasting. (h) Plasma NEFA (mmol/L) and (i) Plasma triglycerides (TGs) (mg/dL) of Adip^{Cre-}WT and Adip^{Cre+}ADAM17KO mice fasted overnight (16h food withdrawal 5pm-9am) and fed (4h food withdrawal during the light phase 8am-12pm). (j) Serum fasting Alanine and (k) Serum fasting lactate levels. Data shown are mean + SEM. P-value was calculated via Student´s t-test.

During fasting, several homeostatic mechanisms aim to keep blood glucose levels with an acceptable range depending on the duration of fasting securing glucose supply to the brain. Liver is the main organ providing glucose to the peripheral tissues. Hepatic glucose production during fasting is fueled by glycogen degradation, for the first few hours of fasting. After glycogen stores have been depleted, glucose is produced by gluconeogenic non-carbohydrate sources that can be converted to pyruvate. Those are gluconeogenic amino acids, lactate and from the glycerol, which is released by hepatic and adipose tissue triglycerides degradation. We found no difference in circulating NEFA (Fig. 21 h), no difference in plasma lactate and a trend to increase in circulating alanine after 16h of overnight fasting (Fig. 21j-k). Therefore, we concluded that there was no difference in availability of typical gluconeogenic substrates between the two genotypes. However, in response to exogenous pyruvate, after an overnight fast 16-18 h the Adip^{Cre+}ADAM17KO mice showed increased hepatic glucose excursion. We investigated the mRNA levels and protein levels of key gluconeogenic enzymes that control the fate of pyruvate conversion to glucose, such as pyruvate carboxylase (Pcx), phosphoenolpyruvate carboxykinase 1 (Pepck or Pck1), fructose-1,6-diphosphatase (Fbp1) and glucose-6-phosphatase (G6pase) and found no difference in their mRNA or protein levels in relation to fasting adaptation of both genotypes (Fig. 22a). Moreover, we also found no differences in rate limiting step enzymes (mRNA and protein levels) of alanine aminotransferase (Gpt2) and L-lactate dehydrogenase (Ldha and Ldhb), catalyzing the conversion of alanine and

lactate to pyruvate respectively (Fig 22b). Finally, we observed no difference in the expression levels of genes that control the glycerol conversion to glucose, such as glycerol kinase (Gk), Glycerol-3-phosphate dehydrogenase (Gpd1), Glycerol-3-phosphate dehydrogenase (Gpd2) (Fig. 22c). These findings further support the conclusion that there is no difference in the availability or utilization of gluconeogenic substrates by the liver of Adip^{Cre+}ADAM17KO mice during fasting.

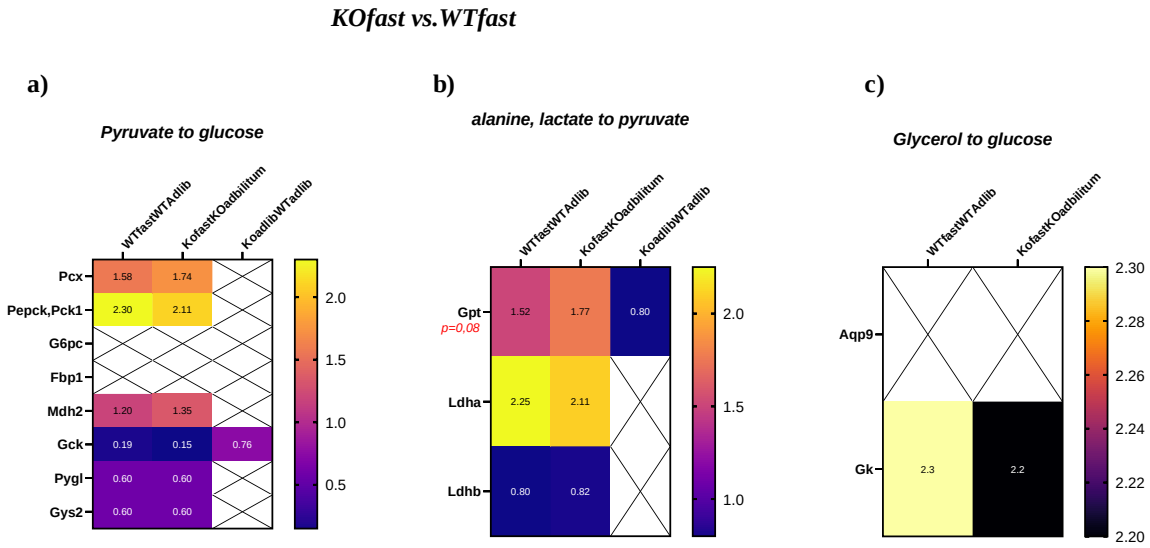

Figure 22: No difference in gene markers of generation of gluconeogenic substrates in the livers of Adip^{Cre+}ADAM17KO mice compared to Adip^{Cre-}WT controls, during fasting.

Heatmap depicting mRNA levels of (a) of some key gluconeogenic enzymes that controls the conversion of pyruvate to glucose, (b) enzymes that catalyses the conversion of alanine and lactate to pyruvate,and (c) also genes that catalyses the conversion of glycerol to glucose found in liver RNA sequencing performed comparing fed and fasted Adip^{Cre+}ADAM17KO mice and Adip^{Cre-}WTmice. Relative expression is shown. Data are mean of 3 mice. Mice were males, 10-12 weeks old, undergone 16 hours, overnight fasting or fed at ad libitum.

3.12 Adip^{Cre+}ADAM17KO mice store more liver glycogen postprandially compared to the Adip^{Cre-}WT mice.

We found almost 2-fold higher glycogen content in the liver of Adip^{Cre+}ADAM17KO mice compared to Adip^{Cre-}WT controls after 16 h fasting. In addition, without any differences in the expression levels of key gluconeogenic genes and proteins and availability of gluconeogenic substrates the Adip^{Cre+}ADAM17KO

mice exhibited higher blood glucose levels during a PTT, suggesting higher hepatic glucose production from the liver of Adip^{Cre+}ADAM17KO compared to Adip^{Cre-}WT controls.

We speculated that Adip^{Cre+}ADAM17KO mice would show higher blood glucose during the PTT because they still have considerable amounts of glycogen in the liver after 16h of fasting compared to Adip^{Cre-}WT mice. Since glycogenolysis and gluconeogenesis can occur in parallel, we speculate that exogenous pyruvate supply during the PTT provided additional source of glucose on top of that generated from glycogenolysis, resulting in higher blood glucose in Adip^{Cre+}ADAM17KO mice compared to Adip^{Cre-}WT controls, during the PTT. To test this hypothesis directly we would need to inject an inhibitor of glycogenolysis during the PTT. If indeed the exogenous pyruvate adds up to the glucose production, which is primarily supported by glycogenolysis in Adip^{Cre+}ADAM17KO mice, we should see no difference in blood glucose during the PTT when both genotypes have received a glycogenolysis inhibitor prior to the PTT. Such inhibitors do exist in the market, and they target the enzyme glycogen phosphorylase, thus impairing glycogen degradation.

Another important question regarding the observed high liver glycogen stores in the Adip^{Cre+}ADAM17KO mice after 16 h fasting is whether they result from increased storage during the postprandial phase or occur because of impaired degradation. To investigate this, we synchronized the mice with 24 h fasting, to cause full depletion of liver glycogen stores, followed by 2 h of refeeding and again 24 h fasting. After that we injected an intraperitoneal glucose (3.5 mg/kg) bolus or saline and sacrificed the mice 4 hours post ip delivery of glucose (Fig. 23a). At 4 h post ip glucose bolus, the Adip^{Cre+}ADAM17KO mice had 3.5-fold greater hepatic glycogen content and higher hepatic glucose content in the liver of Adip^{Cre+}ADAM17KO compared to Adip^{Cre-}WT mice (Fig. 23b-c), whereas there was no difference in hepatic glycogen content between genotypes, that had received saline. These data point to greater glucose uptake and greater glycogen storage in the postprandial state, suggesting greater hepatic insulin sensitivity. Of note we found no difference in the plasma insulin levels in both genotypes 4 h post the ip glucose bolus and the baseline saline control or fed state plasma insulin was also the same between the genotypes (Fig. 23d).

We looked for mRNA and protein levels of key proteins controlling glucose uptake, glycogen storage and insulin signaling at the fed state. At the fed state, we found a significant 1.2-fold higher abundance of GLUT2 protein in the livers of Adip^{Cre+}ADAM17KO compared to the livers of Adip^{Cre-}WT mice. Glycogenesis begins with the phosphorylation of glucose by glucokinase (GCK) in the liver to generate glucose-6-phosphate (Fig. 23e). We found that GCK expression was 1,3-fold higher in the livers of Adip^{Cre+}ADAM17KO mice compared to Adip^{Cre-}WT mice in the fed state (Fig.23f). The next step in glycogenesis is the generation of glucose -1-phosphate from glucose -6-phosphate. This is mediated by phosphoglucomutase in a reaction similar catalyzed by phosphoglycermutase (PGM1). We found no difference in gene expression and protein levels of phosphoglucomutase between the genotypes. Next glucose-1-phopshate turns into uridine 5'-diphopsphate (UDP)-glucose via the action of enzyme UDP-glucose- pyrophosphorylase (UGP2). We found no difference between the genotypes in mRNA and protein levels of UGP2. Glycogen synthase makes the α (1→4) linkages in glycogen. This enzyme cannot initiate chain synthesis using free glucose as an acceptor of a molecule of glucose from UDP-glucose. Instead, it can only elongate already existing chains of glucose and, therefore, requires a primer. A fragment of glycogen can serve as a primer in cells whose glycogen stores are not totally depleted. In the absence of a glycogen fragment, a protein called glycogenin can serve as an acceptor of glucose residues from UDP-glucose. We found no difference between the genotypes in glycogen synthase or glycogenin. Lastly, glycogen is formed into branches, which allows high storage capacity via the action of branching enzymes, mainly glycogen branching enzyme 1 (GBE1). GBE was slightly increased in Adip^{Cre+}ADAM17KO mice 1.18-fold (p-value= 0,059) compared to the Adip^{Cre-}WT mice in the fed state. We found though, phosphorylase b kinase (Phkg2), phosphorylase b kinase regulatory subunit beta (Phkb) and glycogen phosphorylase (Pygl) usually connected with glycogen degradation to be higher in the liver of Adip^{Cre+}ADAM17KO mice compared to the livers of Ad-Cre-WT mice (Fig. 23f). Finally, protein phosphatase 1 regulatory subunit 3c (Ppp1r3c) was significantly downregulated 0.7-fold at the mRNA level in Adip^{Cre+}ADAM17KO mice compared to Adip^{Cre-}WT mice at the fed state. Ppp1r3c acts as a glycogen-targeting subunit for PP1 and regulates its activity. Furthermore, it

activates glycogen synthase, reduces glycogen phosphorylase activity, and limits glycogen breakdown and thus dramatically increases basal and insulin-stimulated glycogen synthesis upon overexpression in a variety of cell types.

Overall, higher levels of glycogen stores at early stages of the postprandial phase clearly argue for promotion of glycogen storage in the Adip^{Cre+}ADAM17KO compared to the Adip^{Cre-}WT mice. Many of the enzymes involved in insulin signaling and glycogen synthesis are regulated at either the protein levels or level of enzymatic activity, which not always positively correlate with each other. Currently we do not have data on the enzymatic activity of those liver enzymes.

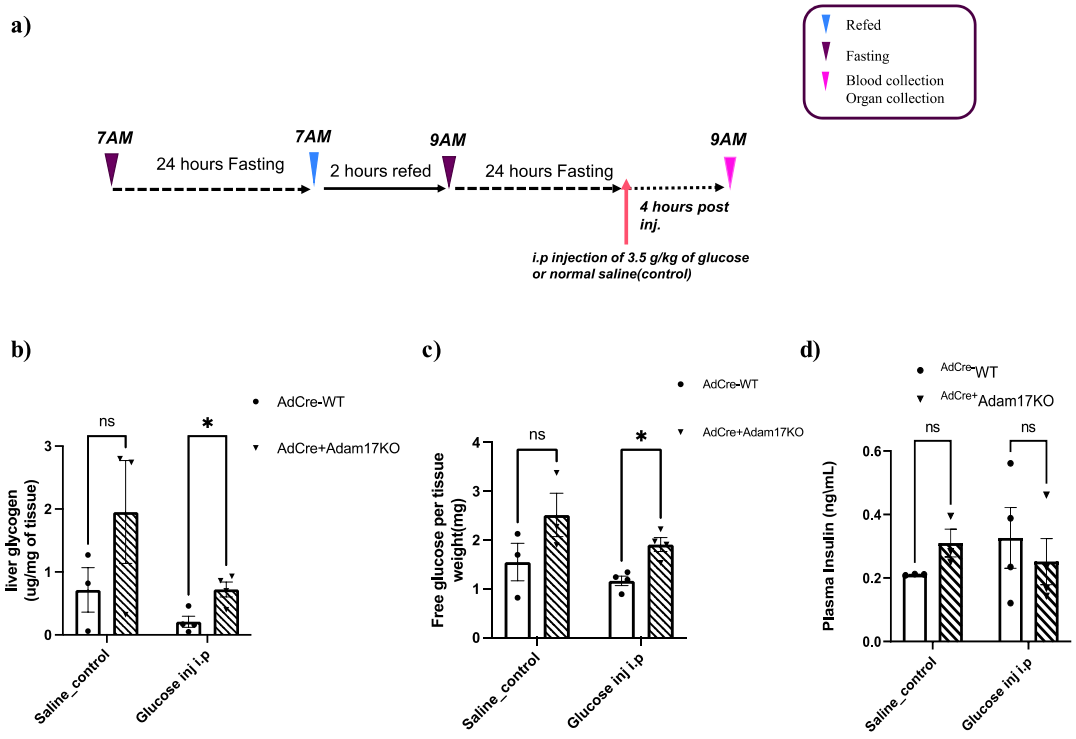

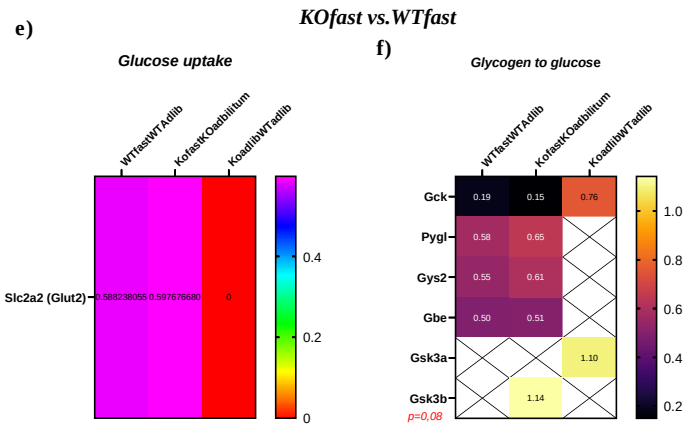

Figure 23: Adip^{Cre+}ADAM17 KO mice store higher amounts of liver glycogen postprandially.

(a) Prolong fasting protocol and glucose bolus delivery to mimic feeding, (b)Liver glycogen levels (ug per mg of tissue) 4 hours post glucose injection (3.5mg/kg) (i.p). (c) Free hepatic glucose produced 4 hours post glucose injection (3.5mg/kg) (i.p). (d) Proteomic analysis shows the protein level of key proteins controlling (e) glucose uptake, (f) glycogen storage at the fed state. Data shown are mean + SEM. P-value was calculated via Student´s t-test. At (e) and (f) Heatmap, depicting mRNA levels is shown.

3.13 Top metabolic pathways altered in liver and adipose tissues of Adip^{Cre+}ADAM17KO mice compared to Adip^{Cre-}WT mice.

To understand the potential link between adipose ADAM17 deletion and liver substrate utilization in baseline and fasting conditions, we performed bulk RNAseq in liver, iWAT and gWAT and untargeted proteomics in liver, iWAT, gWAT and BAT.

At baseline (4 h fast) fed state, bulk RNAseq data showed that adipocyte deletion of ADAM17 led to the upregulation of 115 genes and downregulation of 177 genes in gWAT and upregulation of 299 genes and downregulation of 186 genes in iWAT (Fig. 24a). At the transcriptional level, we observed small overlap between the differentially expressed genes between gWAT and iWAT. Fig. 24b). From the proteomics data, where also BAT was included, we observed 105 proteins upregulated and 374 downregulated in the gWAT, 150 proteins upregulated and 155 downregulated in the iWAT and 180 proteins upregulated and 133 downregulated in the BAT (Fig. 24c). By comparing the type of proteins regulated in the three fat depots, we found again little overlap in differentially expressed proteins between the three fat depots (Fig. 24d). We examined the types of metabolic

pathways altered between the different fat depots between the Adip^{Cre+}ADAM17KO and Adip^{Cre-}WT mice.

In the proteomics datasets comparing Adip^{Cre+}ADAM17KO fed versus Adip^{Cre-}WT mice groups, we found glucocorticoid biosynthesis pathway as one of the top pathways significantly regulated in the liver. Other pathways regulated in the liver are those related to glucose and glucose-1-phosphate degradation pathway, mineralocorticoid biosynthesis and other immune regulatory pathway in the liver (Fig. 25a). Bulk RNA sequencing data performed in gWAT and iWAT at the fed state in Adip^{Cre+}ADAM17KO versus Adip^{Cre-}WT fed groups showed white adipose tissue browning as wells as mevalonate (rate limiting step in cholesterol biosynthesis) and insulin secretion pathway significantly regulated in both fat depots (Fig. 25b-c). In the gWAT, leptin signaling as well as glycerol degradation pathways were also significantly regulated (Fig. 25b-c).

These data suggest that adipocyte specific deletion of ADAM17 exerted fat depot specific effects.

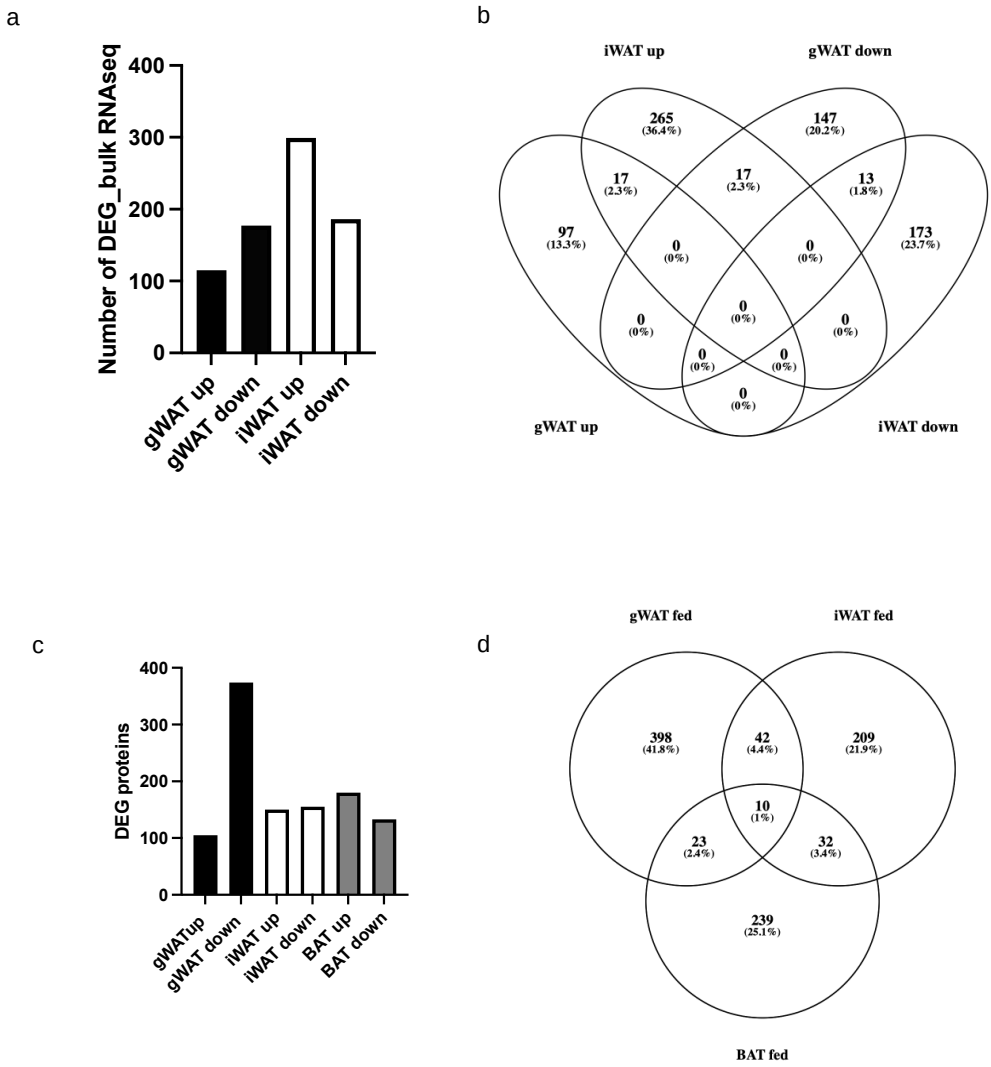

Figure 24: Adipocyte specific deletion of ADAM17 exerted fat depot specific changes in transcriptome and proteome.

(a) Bulk RNAseq data showing differentially expressed genes (DEG) and (b) the overlap between the differentially expressed genes in gWAT and iWAT. (C)Proteomic data showing the DEG and (d) their overlap at the proteins level in the gWAT, iWAT and BAT.

a)

Liver Ad-ADAM17 KO fed vs WT fed

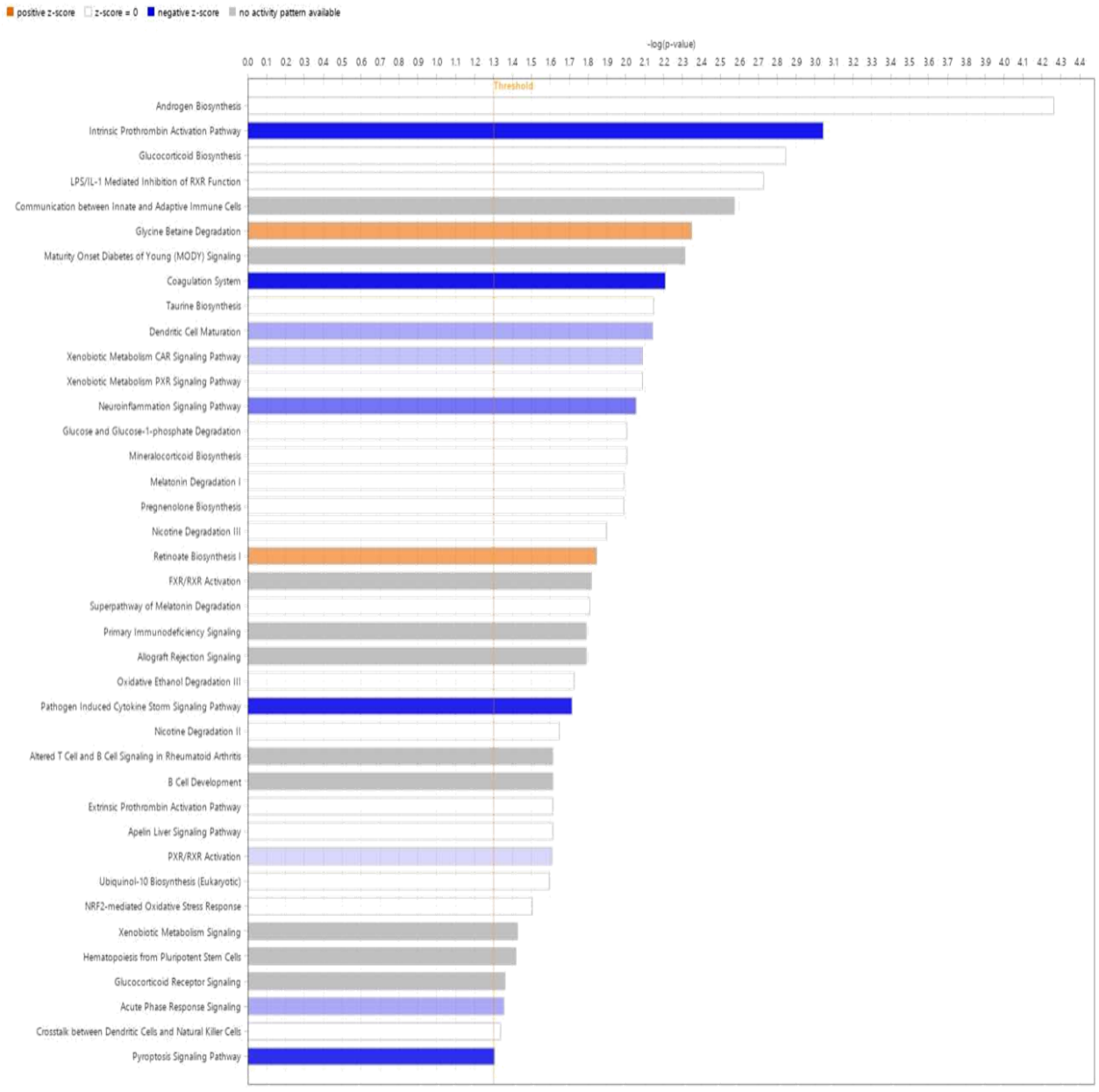

b) gWAT Ad-ADAM17KofedvsWTfed

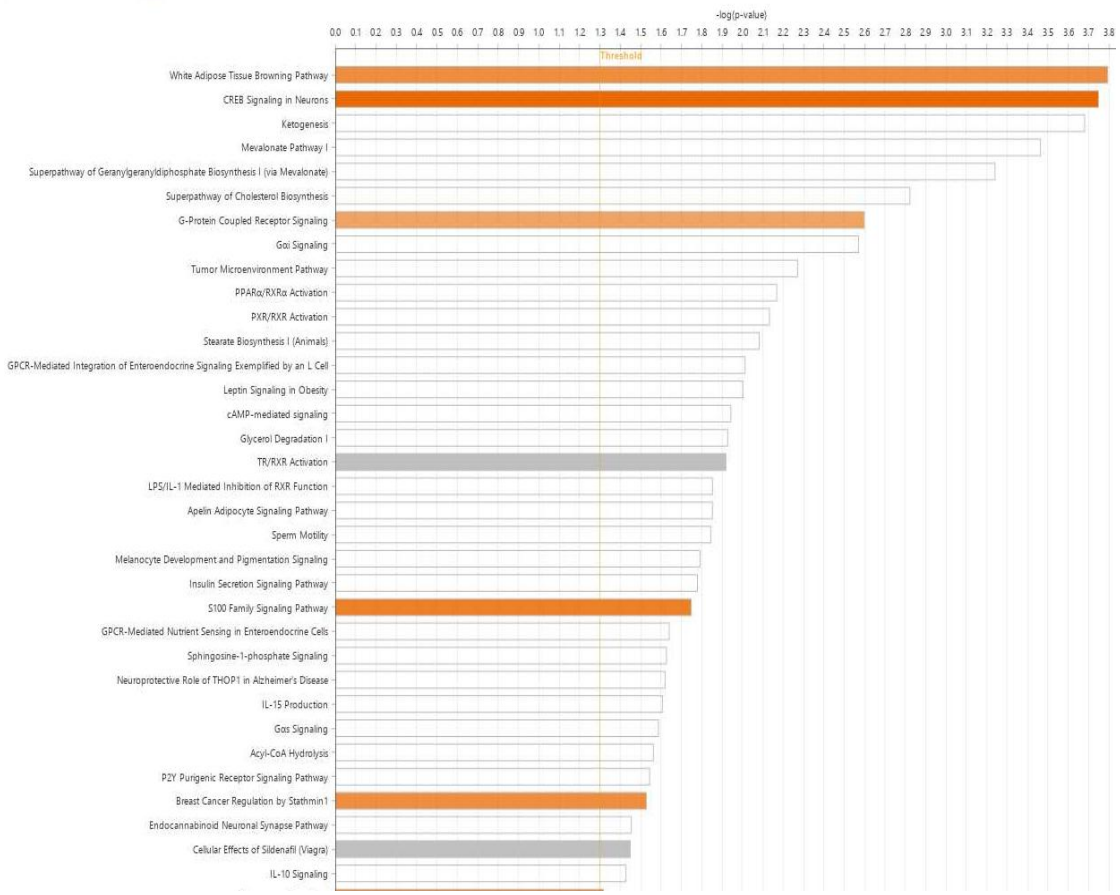

c) iWAT Ad-ADAM17 KO fed

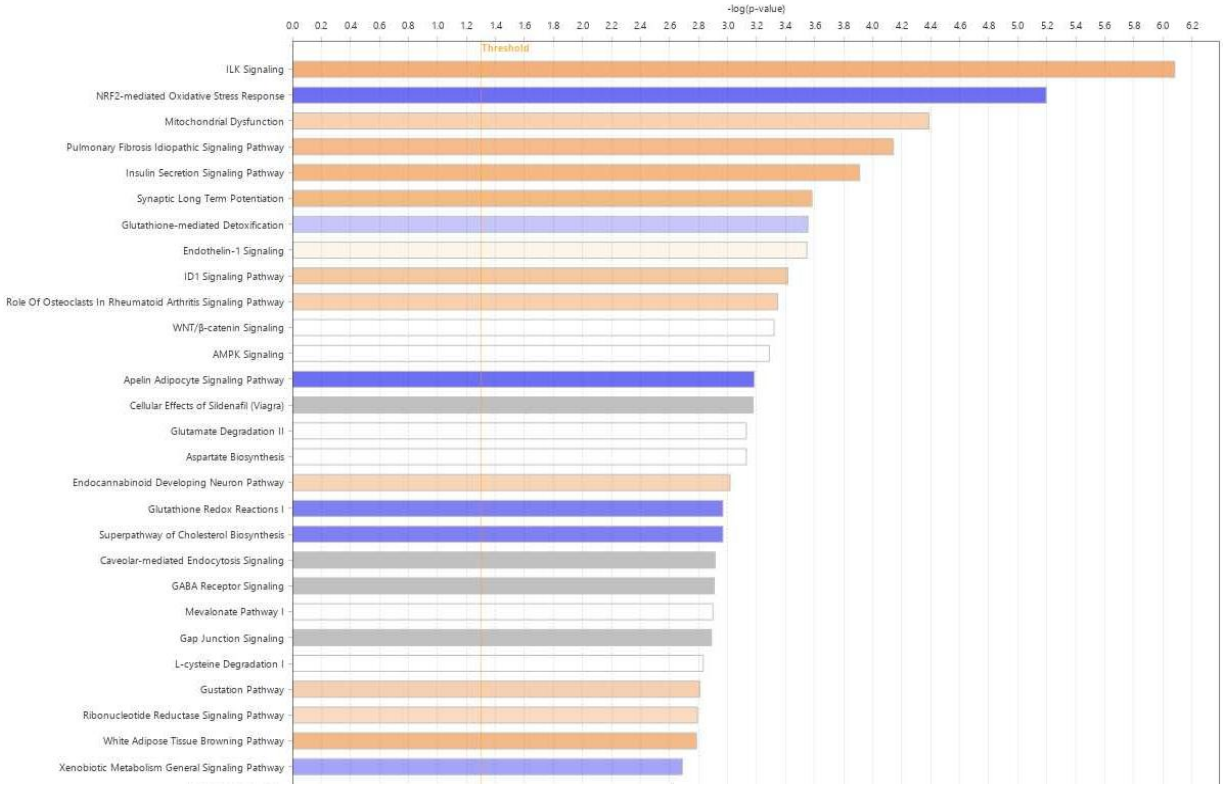

Figure 25: Top metabolic pathways altered in liver and adipose tissues of Ad-$^{Cre+}$ADAM17KO mice compared to Ad^{Cre-}WT mice.

(a) Top pathway in the proteomic data from the liver of Adip^{Cre+}ADAM17KO mice and Ad^{Cre-}WT mice at the fed state (4 hr. fasting). (b, c) Top pathway from the bulk RNA sequencing in the iWAT and gWAT of Adip^{Cre+}ADAM17KO mice and Adip^{Cre-}WT mice at the fed state (baseline 4 hr. fasting).

3.14 Adip^{Cre+}ADAM17KO mice showed increased fasting corticosterone levels.

Due to the observation that glucocorticoid and glucocorticoid receptor pathway are some of the key regulating pathways in Adip^{Cre+}ADAM17KO mice versus Adip^{Cre-}WT mice in the fed state, we were interested in knowing the corticosterone levels in these mice under fed and fasting conditions. Interestingly, fasting serum corticosterone levels were significantly higher in the Adip^{Cre+}ADAM17K mice compared to control mice. No difference was found at fed state serum corticosterone (CORT) levels between the genotypes (Table 10).

CORT levels rise physiologically during prolonged fasting, acting in a tissue specific manner. In the WAT, it stimulates lipolysis and thus providing substrate to the liver for gluconeogenesis to prevent hypoglycemia (Kuo *et al*., 2015). Again, in the liver, increased corticosterone results in enhanced hepatic glycogen storage, partially also explaining the rise in hepatic glycogen storage observed in our Adip^{Cre+}ADAM17KO upon refeeding. Glucagon is another hormone, which is known to activate gluconeogenesis during fasting. In adrenalectomized rats, glucagon induced fasting gluconeogenesis is reduced and this lower gluconeogenetic capacity is restored by injecting mice with glucocorticoids (EXTON & PARK, 1965; Sistare & Haynes, 1985). Because of this reason, we measured glucagon levels in Adip^{Cre+}ADAM17KO and to Adip^{Cre-}WT mice. Fed glucagon levels were not significantly different; with fasting serum glucagon trending to be higher in the Adip^{Cre+}ADAM17KO compared to Adip^{Cre-}WT group (Table 10).

Table 9: Regular chow fed in Ad^{Cre+}ADAM17KO and control mice upon 16h fasted and fed state.

Measurement	AdCre-Adam17f/f	AdCre+Adam17f/f	Pvalue	n	n
Body Weight (g)					
Fasted	24.54 ± 0.54	25.45 ± 0.55	0.32	8	8
Fed	28.12 ± 0.51	26.8 ± 0.68	0.58	8	8
Fat mass (gr) and % BW					
Fasted	0.45 ± 0.07 and 1.85%	0.73 ± 0.15 and 2.93%	0.11 and 0.14	8	8
Fed	1.036 ± 0.11 and 3.71%	1.16 ± 0.16 and 4.31%	0.61 and 0.50	8	8
Lean mass (gr) and % BW					
Fasted	23.11 ± 0.69 and 93.7%	23.6 ± 0.57 and 92.99%	0.54 and 0.64	8	8
Fed	25.58 ± 0.64 and 94.01%	24.76 + 0.59 and 92.31%	0.36 and 0.17	8	8
Plasma glucose (mg/dL)					
Fasted	108 ± 5.63	94 ± 5.62	0.13	5	7
Fed	165 ± 7.53	179 ± 6.36	0.32	4	5
Plasma insulin (ng/ml)					
Fasted	0.126 ± 0.01	0.164 ± 0.04	0.52	5	6
Fed	0.41 ± 0.08	0.30 ± 0.05	0.31	4	5
Plasma glucagon (pmol/L)					
Fasted	2.83 ± 1.39	13.3 ± 5.22	0.13	5	7
Fed	2.89 ± 1.32	0.58 ± 0.73	0.14	4	5
Plasma corticosterone (pg/ml)					
Fasted	521.6 ± 130.2	1033.3 ± 127.5	**0.02**	5	7
Fed	302.7 ± 50.4	223.0 ± 39.2	0.24	4	5

3.15 Similar usage of lipids and carbohydrates upon fasting and refeeding by Adip^{Cre+}ADAM17KO and Ad^{Cre-}WT mice.

During indirect calorimetry, the values of RER during fasting can be used as an estimate of lipids versus carbohydrates utilization. Thus, roughly RER values below 0.7 would suggest high lipid utilization, whereas RER above 1 would suggest high carbohydrates utilization. We examine the RER patterns during prolonged starvation and refeeding and found that Adip^{Cre+}ADAM17KO mice kept slightly RER throughout starvation compared to Adip^{Cre-}WT, although the RER values were quite low in both genotypes (Fig. 26a), meaning that upon prolonged starvation both genotypes highly rely on fat oxidation, whereas the RER increased equally high in both genotypes after refeeding (Fig. 26a). We observed no differences in food intake upon refeeding between the genotypes (Fig. 26b-c).

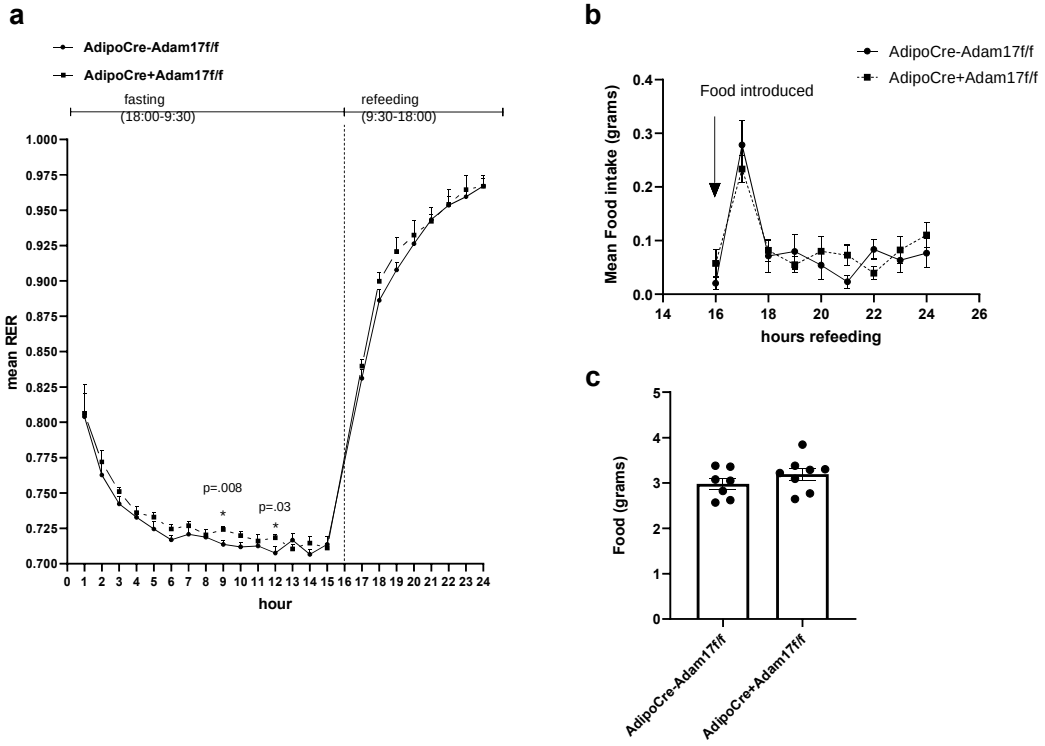

Figure 26: Similar usage of lipids and carbohydrates upon fasting and refeeding by Adip^{Cre+}ADAM17KO and Adip^{Cre-}WT mice.

(a) Indirect calorimetry RER measurements, (b) Food intake measured in metabolic cages during refeeding in indicated time points, (c) Total food intake upon 8 hours refeeding. N=7-8 per genotype. Males, 10-12 weeks old. Data shown are mean + SEM. P-value was calculated via Student´s t-test.

4. Discussion

ADAM17 is known to exert various spatiotemporal effects via the cleavage of its numerous molecular targets. The functions of ADAM17 in adipocytes are not well understood. Here we report that ADAM17 deletion altered the protein levels of ADBR3 receptor in murine white and brown adipocytes, but this had no impact on the lipolysis in response to CL 316,243, ADBR3 specific agonist, nor in white or brown adipocytes. Recently, a homologue of ADRB3 receptor, the ADRB1 receptor, which is not present in murine white adipocytes, but it is highly expressed in the heart has been identified as a target of ADAM17. ADAM17 generates a truncated ADRB1, which despite the fact that it binds to the isoproterenol agonist at the same way as the full version, it generates a different intracellular signaling cascade compared to the full length receptor (Goth *et al*., 2017)(Zhu & Steinberg, 2021),(Park *et al*., 2017),(Hakalahti *et al*., 2010). Therefore, it would be very important to clarify whether ADAM17 can physically interact with ADRB3 and in this way affect its canonical and non-canonical signaling. Although we see higher protein levels of ADRB3 in the ADAM17KO adipocytes, we need to clarify whether these additional copies occupy the plasma membrane or they are accumulated in an intracellular organelle, like the endoplasmic reticulum. Indeed, higher plasma membrane levels of ADRB3 should be resulting in higher lipolytic response to CL 316,243. The fact that we do not observe this, means, either ADRB3 intracellular trafficking is affected or indeed an alternate signaling of ADRB3 is affected without changes in the one controlling lipolysis. MAP kinase signaling is a candidate one. Following up on the characterization of our sorted preadipocytes/adipocytes, with different expression levels of ADAM17 at baseline and upon catecholamine stimulation will also help up if there is a differential intracellular wiring of ADRB3, dependent on the expression levels of ADAM17.

Our mouse phenotyping experiments revealed that the absence of ADAM17 from the adipocytes led to impaired adaptation to cold temperature exposure. We did not observe differences at the protein levels of ADRB3 in vivo (measured by total proteomics), however untargeted proteomics have low resolution for membrane receptors and mainly cover cytosolic proteins. Therefore, a more targeted validation with western blot from total cell lysates and plasma membrane must be done to quantify ADRB3 in BAT and WAT upon cold exposure in Adip^{Cre+}ADAM17KO and Adip^{Cre-}WT mice. Most interesting molecular finding from this study is the fact that UCP1 protein levels are similar between the genotypes upon cold exposure, but alternative futile cycles such as creatine futile cycle and fat re-esterification

and overall ATP synthesis seem to be upregulated in Adip^{Cre+}ADAM17KO compared to Adip^{Cre-}WT mice upon cold exposure. Previous published work have reported those futile pathways as relevant for thermogenesis only in the absence of UCP1 (Rahbani *et al*., 2024), however here we see full increase of expression UCP1 by cold exposure in both genotypes but and still parallel expression of futile cycles. We speculate that despite UCP1 being increased at the transcriptional and protein level by cold, it is not activated. Lipolysis released fatty acids are necessary for activation of UCP1 (Divakaruni *et al*., 2012), also endogenous GTP can act as inhibitor of UCP1 (Jones *et al*., 2023). We need to perform focused in vitro experiments to clarify the activity levels of UCP1 in brown and white Adip^{Cre+}ADAM17KO adipocyte, at baseline and catecholamine stimulation conditions. To that end Seahorse experiments to investigate the catecholamine stimulated uncoupling, total uncoupling capacity of mitochondria and dependency of oxygen consumption on ATP synthesis generated from glycolysis, lipolysis or driven by fatty acid re-esterification should give a complete picture on the futile cycles drive oxygen consumption in Adip^{Cre+}ADAM17KO compared to Adip^{Cre+}WT, brown and white adipocytes. In addition, it is important to quantify total mitochondrial numbers and assess mitochondrial networking in case ADAM17 affect interconnectivity of mitochondrial and ER.

Adip^{Cre+}ADAM17KO gained more body weight upon HFD compared to Adip^{Cre-}WT controls. This is in line of impaired catecholamine signaling, as suggested by our associative datasets to this pathway. Interestingly, the increased fat accumulation was observed in iWAT and mesenteric fat, but not gWAT. Upon HFD conditions iWAT, similar to subcutaneous fat in humans will be the first to develop catecholamine resistance and thus increased lipolysis (Engfeldt & Arner, 1988). gWAT containing less ADRB3 protein levels is remaining more lipolytic in obese individuals. It is interesting that we did not observe any changes in the glucose tolerance, but increased cholesterol levels. In combination to the fact that mesenteric fat mass is increase, we should investigate deeper potential changes in absorption of cholesterol by the intestine as well as liver cholesterol and triglyceride content. Overall, our findings point to differential effects/functions of ADAM17 in different fat depot, which should be followed up in depth. Moreover, CL 316,243 injections did not affect EE in mice, but rather change circulating cholesterol, suggesting a specific connection of ADRB3 stimulation in adipocytes and cholesterol redistribution or absorption Adip^{cre+}ADAM17KO compared to Adip^{Cre-}WT mice. Thus, the link of adipocyte ADAM17 and systemic cholesterol metabolism must be investigated further.

Upon prolonged refeeding, we observed a greater accumulation of glycogen in the liver and possibly greater utilization of this additional glycogen during fasting. We found no difference in fasting glucose between the genotypes, so we could speculate that Adip^{cre+}ADAM17KO rely on glycogen stores to maintain high blood glucose levels upon prolong fasting (16 h-24 h), whereas Adip^{Cre-}WT mobilize gluconeogenic substrates, which they enter the liver to generate glucose via de novo gluconeogenesis, since glycogen store are depleted within the first 12 hours of fasting. We hypothesize that Adip^{cre+}ADAM17KO have a lack of gluconeogenic substrates, possible fatty acids as they also utilize less glycerol compared to the controls for glucose production. To verify this hypothesis, we could inject both genotypes with inhibitors of glycogenolysis, which will force de novo gluconeogenesis.

During the time of this thesis, two studies were published on the phenotypic characterization of the AdiponectinCre ADAM17 deletion upon HFD. The study b AdiponectinCre (Lownik *et al*., 2020) generated AdiponectinCre ADAM17 KO mice and challenged them with HFD 60% fat for 12 weeks. They found no impact of ADAM17 deletion in adipocytes in body weight gain, glucose tolerance or indirect respirometry experiments, concluding that adipocyte ADAM17 plays a limited role in metabolic inflammation generated by HFD. Surprisingly another study by (Amin *et al*., 2023a) reported that AdiponectinCre ADAM17KO when put on HFD 60% for 26 weeks, gained less weight compared to the WT control group, with this difference started being obvious at 12 weeks on HFD. (Amin *et al*., 2023a) discuss that the longer duration of HFD in their study as opposed to the shorter one in the study of (Lownik *et al*., 2020) could be the reason for this difference on the interaction of adipocyte ADAM17 and HFD. Amin A *et al* attribute the obesity protection effect of ADAM17 on higher thermogenesis due to more active BAT; however, no cold exposure had been performed in this paper. In our study, we see that upon HFD 45% fat, Adip^{cre+}ADAM17KO gained more weight compared to the Adip^{Cre-}WT and accumulate more fat in the inguinal and mesenteric fat depots. These results are quite opposite to the ones published. One major issue in the published studies is the lack of backcrosses. We communicated by email on this topic with the last author of the Amin A *et al* study who told that that ADAM17 flox/flox mice purchased by JAX were crossed only once with the AdiponectinCre J mice, as mentioned in the methods section and no backcrossing was performed. It is important here to underline the necessity for backcrosses for the ADAM17 flox/flox line 009567, from JAX, which is the one we are also using. That is because the ADAM17 flox/flox mouse line was purchased from Jackson

Laboratory, mouse strain #:009597, as specified on their website were generated as mutant mice of C57BL/6; 129P2/OlaHsd genetic background, which were bred with mice on B6; SJL genetic background. The mice were maintained on a mix genetic background and upon arrival to the Jackson were bred at least once to C57BL/6J (Stock No. 000664) for at least one generation to establish the colony. The mice were of mixed genetic background when they arrived at our laboratory (HMGU, DMF), which was evident by the fact that half were of black fur (typical for C57BL/6J) and the other half were of white fur which most likely derived from the 129P2/OlaHsd genetic background. All these background strains, C57BL/6, B6; SJL and 129P2/OlaHsd have completely different metabolic phenotypes under chow and HFD. For example mice of 129P2/OlaHsd genetic background develop a highest severity of hepatosteatosis upon HFD, compared to C57BL/6J(Kahle *et al*., 2013). As a result, phenotyping mice of such mixed genetic background would hold high risk of genetic background related metabolic trains and most likely not reproducible as ADAM17 deletion related outcomes. After 6 backcrosses of the Jackson's Laboratory ADAM17flox/flox mice with pure WT C57BL6J mice we were able to obtain consistently mice of black fur color, as opposed to prior generations where mice had either black, gray or white fur color. We have determined the 'cleanness' of the genetic background of the mouse line we have been phenotype in this thesis, by SNP Genome Scanning Analysis with the Jackson (table 7). Next to this fact, we also have used a 45% HFD which has higher content in sucrose, compared to the HFD 60%. Whether the additional sucrose changes completely the phenotype need to be determined.

In conclusion, here we have generated a clean C57bl6J deletion of ADAM17 upon the control of the AdiponectinCre promoter, thus a conditional deletion of ADAM17 in adipocytes. We report that these mice show impaired cold tolerance, increased weight gain upon HFD and increased glycogen accumulation in the liver. At the cellular level ADAM17 deletion associates with changes of several gene and protein markers of oxidative phosphorylation and higher protein, level of ADRB3 in murine brown and white adipocytes. Our study provides an associative link between ADAM17 and Catecholamine-ADRB3 signaling in brown and white adipocytes, with potentially important impact for whole body cold adaptation, systemic cholesterol metabolism and lipid handling by the adipocytes.

References

Amin, A., Badenes, M., Tüshaus, J., de Carvalho, É., Burbridge, E., Faísca, P., Trávníčková, K., Barros, A., Carobbio, S., Domingos, P. M., Vidal-Puig, A., Moita, L. F., Maguire, S., Stříšovský, K., Ortega, F. J., Fernández-Real, J. M., Lichtenthaler, S. F., & Adrain, C. (2023a). Semaphorin 4B is an ADAM17-cleaved adipokine that inhibits adipocyte differentiation and thermogenesis. *Molecular Metabolism*, *73*(April). https://doi.org/10.1016/j.molmet.2023.101731

Amin, A., Badenes, M., Tüshaus, J., de Carvalho, É., Burbridge, E., Faísca, P., Trávníčková, K., Barros, A., Carobbio, S., Domingos, P. M., Vidal-Puig, A., Moita, L. F., Maguire, S., Stříšovský, K., Ortega, F. J., Fernández-Real, J. M., Lichtenthaler, S. F., & Adrain, C. (2023b). Semaphorin 4B is an ADAM17-cleaved adipokine that inhibits adipocyte differentiation and thermogenesis. *Molecular Metabolism*, *73*(April), 101731. https://doi.org/10.1016/j.molmet.2023.101731

Audano, M., Pedretti, S., Caruso, D., Crestani, M., De Fabiani, E., & Mitro, N. (2022). Regulatory mechanisms of the early phase of white adipocyte differentiation: an overview. *Cellular and Molecular Life Sciences*, *79*(3), 1–14. https://doi.org/10.1007/s00018-022-04169-6

Avram, A. S., Avram, M. M., & James, W. D. (2005). Subcutaneous fat in normal and diseased states: 2. Anatomy and physiology of white and brown adipose tissue. *Journal of the American Academy of Dermatology*, *53*(4), 671–683. https://doi.org/10.1016/j.jaad.2005.05.015

Bertholet, A. M., Chouchani, E. T., Kazak, L., Angelin, A., Fedorenko, A., Long, J. Z., Vidoni, S., Garrity, R., Cho, J., Terada, N., Wallace, D. C., Spiegelman, B. M., & Kirichok, Y. (2019). H+ transport is an integral function of the mitochondrial ADP/ATP carrier. *Nature*, *571*(7766), 515–520. https://doi.org/10.1038/s41586-019-1400-3

Black, R. A., Rauch, C. T., Kozlosky, C. J., Peschon, J. J., Slack, J. L., Wolfson, M. F., Castner, B. J., Stocking, K. L., Reddy, P., Srinivasan, S., Nelson, N., Boiani, N., Schooley, K. A., Gerhart, M., Davis, R., Fitzner, J. N., Johnson, R. S., Paxton, R. J., March, C. J., & Cerretti, D. P. (1997). A metalloproteinase disintegrin that releases tumour-necrosis factor-ø from cells. In *Nature* (Vol. 385, Issue 6618, pp. 729–733). https://doi.org/10.1038/385729a0

Blondin, D. P., Nielsen, S., Kuipers, E. N., Severinsen, M. C., Jensen, V. H., Miard, S., Jespersen, N. Z., Kooijman, S., Boon, M. R., Fortin, M., Phoenix, S., Frisch, F., Guérin, B., Turcotte, É. E., Haman, F., Richard, D., Picard, F., Rensen, P. C. N., Scheele, C., & Carpentier, A. C. (2020). Human Brown Adipocyte Thermogenesis Is Driven by β2-AR Stimulation. *Cell Metabolism*, *32*(2), 287-300.e7. https://doi.org/10.1016/j.cmet.2020.07.005

Börgeson, E., Boucher, J., & Hagberg, C. E. (2022). Of mice and men: Pinpointing species differences in adipose tissue biology. *Frontiers in Cell and Developmental Biology*, *10*, 1003118. https://doi.org/10.3389/fcell.2022.1003118

Brownstein, A. J., Veliova, M., Acin-Perez, R., Liesa, M., & Shirihai, O. S. (2022). ATP-consuming futile cycles as energy dissipating mechanisms to counteract obesity. *Reviews in Endocrine & Metabolic Disorders*, *23*(1), 121–131. https://doi.org/10.1007/s11154-021-09690-w

Carobbio, S., Guénantin, A. C., Samuelson, I., Bahri, M., & Vidal-Puig, A. (2019). Brown and beige fat: From molecules to physiology and pathophysiology. *Biochimica et Biophysica Acta - Molecular and Cell Biology of Lipids*, *1864*(1), 37–50. https://doi.org/10.1016/j.bbalip.2018.05.013

Carpentier, A. C., Blondin, D. P., Haman, F., & Richard, D. (2023). Brown Adipose Tissue—A Translational Perspective. *Endocrine Reviews*, *44*(2), 143–192. https://doi.org/10.1210/endrev/bnac015

Cero, C., Lea, H. J., Zhu, K. Y., Shamsi, F., Tseng, Y., & Cypess, A. M. (2021). β3 -Adrenergic receptors regulate human brown/beige adipocyte lipolysis and thermogenesis. *JCI Insight*, *6*(11), 1–20.

Chouchani, E. T., Kazak, L., & Spiegelman, B. M. (2019). New Advances in Adaptive Thermogenesis: UCP1 and Beyond. *Cell Metabolism*, *29*(1), 27–37.

https://doi.org/https://doi.org/10.1016/j.cmet.2018.11.002

Chun, K.-H. (2021). Mouse model of the adipose organ: the heterogeneous anatomical characteristics. *Archives of Pharmacal Research*, *44*(9–10), 857–875. https://doi.org/10.1007/s12272-021-01350-6

Chusyd, D. E., Wang, D., Huffman, D. M., & Nagy, T. R. (2016). Relationships between Rodent White Adipose Fat Pads and Human White Adipose Fat Depots. *Frontiers in Nutrition*, *3*, 10. https://doi.org/10.3389/fnut.2016.00010

Coles, C. A., Maksimovic, J., Wadeson, J., Fahri, F. T., Webster, T., Leyton, C., McDonagh, M. B., & White, J. D. (2018). Knockdown of a disintegrin A metalloprotease 12 (ADAM12) during adipogenesis reduces cell numbers, delays differentiation, and increases lipid accumulation in 3T3-L1 cells. *Molecular Biology of the Cell*, *29*(15), 1839–1855. https://doi.org/10.1091/mbc.E17-07-0471

Diering, Erin C. Dowd, M.D.a, Michael J. Frank, Ph.D.b, Anne Collins, Ph.D.c, James M. Goldd, and Deanna M. Barch, P. D. ., & Daniel E Shumer, Natalie J Nokoff, N. P. S. (2017). Disruption of beta3 adrenergic receptor increases susceptibility to DIO in mouse. *Physiology & Behavior*, *176*(12), 139–148. https://doi.org/10.1530/JOE-16-0199.Disruption

Divakaruni, A. S., Humphrey, D. M., & Brand, M. D. (2012). Fatty acids change the conformation of uncoupling protein 1 (UCP1). *The Journal of Biological Chemistry*, *287*(44), 36845–36853. https://doi.org/10.1074/jbc.M112.381780

Emont, M. P., Jacobs, C., Essene, A. L., Pant, D., Tenen, D., Colleluori, G., Di Vincenzo, A., Jørgensen, A. M., Dashti, H., Stefek, A., McGonagle, E., Strobel, S., Laber, S., Agrawal, S., Westcott, G. P., Kar, A., Veregge, M. L., Gulko, A., Srinivasan, H., … Rosen, E. D. (2022). A single-cell atlas of human and mouse white adipose tissue. *Nature*, *603*(7903), 926–933. https://doi.org/10.1038/s41586-022-04518-2

Engfeldt, P., & Arner, P. (1988). Lipolysis in human adipocytes, effects of cell size, age and of regional differences. *Hormone and Metabolic Research. Supplement Series*, *19*, 26–29.

Evans, B. A., Merlin, J., Bengtsson, T., & Hutchinson, D. S. (2019). Adrenoceptors in white, brown, and brite adipocytes. *British Journal of Pharmacology*, *176*(14), 2416–2432. https://doi.org/10.1111/bph.14631

EXTON, J. H., & PARK, C. R. (1965). Control of Gluconeogenesis in the Perfused Liver of Normal and. *The Journal of Biological Chemistry*, *240*(2), 955–957. https://doi.org/10.1016/S0021-9258(17)45267-7

Fan, H., & Derynck, R. (1999). Ectodomain shedding of TGF-alpha and other transmembrane proteins is induced by receptor tyrosine kinase activation and MAP kinase signaling cascades. *The EMBO Journal*, *18*(24), 6962–6972. https://doi.org/10.1093/emboj/18.24.6962

Fedorenko, A., Lishko, P. V, & Kirichok, Y. (2012). Mechanism of fatty-acid-dependent UCP1 uncoupling in brown fat mitochondria. *Cell*, *151*(2), 400–413. https://doi.org/10.1016/j.cell.2012.09.010

Gelling, R. W., Yan, W., Al-Noori, S., Pardini, A., Morton, G. J., Ogimoto, K., Schwartz, M. W., & Dempsey, P. J. (2008). Deficiency of TNFalpha converting enzyme (TACE/ADAM17) causes a lean, hypermetabolic phenotype in mice. *Endocrinology*, *149*(12), 6053–6064. https://doi.org/10.1210/en.2008-0775

Georgiadi, A., Lopez-Salazar, V., Merahbi, R. El, Karikari, R. A., Ma, X., Mourão, A., Klepac, K., Bühler, L., Alfaro, A. J., Kaczmarek, I., Linford, A., Bosma, M., Shilkova, O., Ritvos, O., Nakamura, N., Hirose, S., Lassi, M., Teperino, R., Machado, J., … Herzig, S. (2021). Orphan GPR116 mediates the insulin sensitizing effects of the hepatokine FNDC4 in adipose tissue. *Nature Communications*, *12*(1), 1–21. https://doi.org/10.1038/s41467-021-22579-1

Goth, C. K., Tuhkanen, H. E., Khan, H., Lackman, J. J., Wang, S., Narimatsu, Y., Hansen, L. H., Overall, C. M., Clausen, H., Schjoldager, K. T., & Petäjä-Repo, U. E. (2017). Site-specific O-glycosylation by polypeptide N-acetylgalactosaminyltransferase 2 (GalNAc-transferase T2) co-regulates β1-adrenergic receptor N-terminal cleavage. *Journal of Biological*

Chemistry, *292*(11), 4714–4726. https://doi.org/10.1074/jbc.M116.730614

Hakalahti, A. E., Vierimaa, M. M., Lilja, M. K., Kumpula, E. P., Tuusa, J. T., & Petäjä-Repo, U. E. (2010). Human β1-adrenergic receptor is subject to constitutive and regulated N-terminal cleavage. *Journal of Biological Chemistry*, *285*(37), 28850–28861. https://doi.org/10.1074/jbc.M110.149989

Hammond, V. A., & Johnston, D. G. (1987). Substrate cycling between triglyceride and fatty acid in human adipocytes. *Metabolism: Clinical and Experimental*, *36*(4), 308–313. https://doi.org/10.1016/0026-0495(87)90199-5

Heaton, J. M. (1972). The distribution of brown adipose tissue in the human. *Journal of Anatomy*, *112*(Pt 1), 35–39. http://www.ncbi.nlm.nih.gov/pubmed/5086212%0Ahttp://www.pubmedcentral.nih.gov/articlerender.fcgi?artid=PMC1271341

Horiuchi, K., Le Gall, S., Schulte, M., Yamaguchi, T., Reiss, K., Murphy, G., Toyama, Y., Hartmann, D., Saftig, P., & Blobel, C. P. (2007). Substrate selectivity of epidermal growth factor-receptor ligand sheddases and their regulation by phorbol esters and calcium influx. *Molecular Biology of the Cell*, *18*(1), 176–188. https://doi.org/10.1091/mbc.e06-01-0014

Hudak, C. S., & Sul, H. S. (2013). Pref-1, a gatekeeper of adipogenesis. *Frontiers in Endocrinology*, *4*, 79. https://doi.org/10.3389/fendo.2013.00079

Hull, D., & Segall, M. M. (1965). The contribution of brown adipose tissue to heat production in the new-born rabbit. *The Journal of Physiology*, *181*(3), 449–457. https://doi.org/10.1113/jphysiol.1965.sp007773

Ikeda, K., & Yamada, T. (2020). UCP1 Dependent and Independent Thermogenesis in Brown and Beige Adipocytes. *Frontiers in Endocrinology*, *11*, 498. https://doi.org/10.3389/fendo.2020.00498

Jalloul, W., Moscalu, M., Moscalu, R., Jalloul, D., Grierosu, I. C., Ionescu, T., Stolniceanu, C. R., Ghizdovat, V., Mocanu, V., Iliescu, R., Pavaleanu, I., & Stefanescu, C. (2023). Off the Beaten Path in Oncology: Active Brown Adipose Tissue by Virtue of Molecular Imaging. *Current Issues in Molecular Biology*, *45*(10), 7891–7914. https://doi.org/10.3390/cimb45100499

Jimenez, M., Léger, B., Canola, K., Lehr, L., Arboit, P., Seydoux, J., Russell, A. P., Giacobino, J. P., Muzzin, P., & Preitner, F. (2002). Beta(1)/beta(2)/beta(3)-adrenoceptor knockout mice are obese and cold-sensitive but have normal lipolytic responses to fasting. *FEBS Letters*, *530*(1–3), 37–40. https://doi.org/10.1016/s0014-5793(02)03387-2

Jones, S. A., Gogoi, P., Ruprecht, J. J., King, M. S., Lee, Y., Zögg, T., Pardon, E., Chand, D., Steimle, S., Copeman, D. M., Cotrim, C. A., Steyaert, J., Crichton, P. G., Moiseenkova-Bell, V., & Kunji, E. R. S. (2023). Structural basis of purine nucleotide inhibition of human uncoupling protein 1. *Science Advances*, *9*(22), eadh4251. https://doi.org/10.1126/sciadv.adh4251

Josson, S., Anderson, C. S., Sung, S.-Y., Johnstone, P. A. S., Kubo, H., Hsieh, C.-L., Arnold, R., Gururajan, M., Yates, C., & Chung, L. W. K. (2011). Inhibition of ADAM9 expression induces epithelial phenotypic alterations and sensitizes human prostate cancer cells to radiation and chemotherapy. *The Prostate*, *71*(3), 232–240. https://doi.org/10.1002/pros.21237

Kahle, M., Horsch, M., Fridrich, B., Seelig, A., Schultheiß, J., Leonhardt, J., Irmler, M., Beckers, J., Rathkolb, B., Wolf, E., Franke, N., Gailus-Durner, V., Fuchs, H., de Angelis, M. H., & Neschen, S. (2013). Phenotypic comparison of common mouse strains developing high-fat diet-induced hepatosteatosis. *Molecular Metabolism*, *2*(4), 435–446. https://doi.org/10.1016/j.molmet.2013.07.009

Kaneko, H., Anzai, T., Horiuchi, K., Morimoto, K., Anzai, A., Nagai, T., Sugano, Y., Maekawa, Y., Itoh, H., Yoshikawa, T., Okada, Y., Ogawa, S., & Fukuda, K. (2011). Tumor necrosis factor-α converting enzyme inactivation ameliorates high-fat diet-induced insulin resistance and altered energy homeostasis. *Circulation Journal : Official Journal of the Japanese Circulation Society*, *75*(10), 2482–2490. https://doi.org/10.1253/circj.cj-11-0182

Kawaguchi, N., Xu, X., Tajima, R., Kronqvist, P., Sundberg, C., Loechel, F., Albrechtsen, R., & Wewer, U. M. (2002). ADAM 12 protease induces adipogenesis in transgenic mice. *The American Journal of Pathology*, *160*(5), 1895–1903. https://doi.org/10.1016/S0002-9440(10)61136-4

Kazak, L., Chouchani, E. T., Jedrychowski, M. P., Erickson, B. K., Shinoda, K., Cohen, P., Vetrivelan, R., Lu, G. Z., Laznik-Bogoslavski, D., Hasenfuss, S. C., Kajimura, S., Gygi, S. P., & Spiegelman, B. M. (2015). A creatine-driven substrate cycle enhances energy expenditure and thermogenesis in beige fat. *Cell*, *163*(3), 643–655. https://doi.org/10.1016/j.cell.2015.09.035

Kim, H., Kim, M., Im, S.-K., & Fang, S. (2018). Mouse Cre-LoxP system: general principles to determine tissue-specific roles of target genes. *Laboratory Animal Research*, *34*(4), 147. https://doi.org/10.5625/lar.2018.34.4.147

Klingenberg, M. (2008). The ADP and ATP transport in mitochondria and its carrier. *Biochimica et Biophysica Acta*, *1778*(10), 1978–2021. https://doi.org/10.1016/j.bbamem.2008.04.011

Kuo, T., McQueen, A., Chen, T.-C., & Wang, J.-C. (2015). *Regulation of Glucose Homeostasis by Glucocorticoids BT - Glucocorticoid Signaling: From Molecules to Mice to Man* (J.-C. Wang & C. Harris (eds.); pp. 99–126). Springer New York. https://doi.org/10.1007/978-1-4939-2895-8_5

Kurisaki, K., Kurisaki, A., Valcourt, U., Terentiev, A. A., Pardali, K., Ten Dijke, P., Heldin, C.-H., Ericsson, J., & Moustakas, A. (2003). Nuclear factor YY1 inhibits transforming growth factor beta- and bone morphogenetic protein-induced cell differentiation. *Molecular and Cellular Biology*, *23*(13), 4494–4510. https://doi.org/10.1128/MCB.23.13.4494-4510.2003

Kveiborg, M., Instrell, R., Rowlands, C., Howell, M., & Parker, P. J. (2011). PKCα and PKCδ regulate ADAM17-mediated ectodomain shedding of heparin binding-EGF through separate pathways. *PloS One*, *6*(2), e17168. https://doi.org/10.1371/journal.pone.0017168

Larter, C. Z., Chitturi, S., Heydet, D., & Farrell, G. C. (2010). A fresh look at NASH pathogenesis. Part 1: the metabolic movers. *Journal of Gastroenterology and Hepatology*, *25*(4), 672–690. https://doi.org/10.1111/j.1440-1746.2010.06253.x

Li, Y., Li, Z., Ngandiri, D. A., Llerins Perez, M., Wolf, A., & Wang, Y. (2022). The Molecular Brakes of Adipose Tissue Lipolysis. *Frontiers in Physiology*, *13*(February), 1–19. https://doi.org/10.3389/fphys.2022.826314

Liu, Q., Long, Q., Zhao, J., Wu, W., Lin, Z., Sun, W., Gu, P., Deng, T., Loomes, K. M., Wu, D., Kong, A. P. S., Zhou, J., Cheng, A. S., & Hui, H. X. (2023). Cold-Induced Reprogramming of Subcutaneous White Adipose Tissue Assessed by Single-Cell and Single-Nucleus RNA Sequencing. *Research (Washington, D.C.)*, *6*, 182. https://doi.org/10.34133/research.0182

Lownik, J. C., Farrar, J. S., Pearce, J. V., Celi, F. S., & Martin, R. K. (2020). Adipocyte ADAM17 plays a limited role in metabolic inflammation. *Adipocyte*, *9*(1), 509–522. https://doi.org/10.1080/21623945.2020.1814544

Lu, P., Takai, K., Weaver, V. M., & Werb, Z. (2011). Extracellular matrix degradation and remodeling in development and disease. *Cold Spring Harbor Perspectives in Biology*, *3*(12). https://doi.org/10.1101/cshperspect.a005058

MacPherson, R. E. K., Castellani, L., Beaudoin, M.-S., & Wright, D. C. (2014). Evidence for fatty acids mediating CL 316,243-induced reductions in blood glucose in mice. *American Journal of Physiology. Endocrinology and Metabolism*, *307*(7), E563-70. https://doi.org/10.1152/ajpendo.00287.2014

Masaki, M., Kurisaki, T., Shirakawa, K., & Sehara-Fujisawa, A. (2005). Role of meltrin α (ADAM12) in obesity induced by high-fat diet. *Endocrinology*, *146*(4), 1752–1763. https://doi.org/10.1210/en.2004-1082

Michel, L. Y. M., Farah, C., & Balligand, J.-L. (2020). The Beta3 Adrenergic Receptor in Healthy and Pathological Cardiovascular Tissues. *Cells*, *9*(12). https://doi.org/10.3390/cells9122584

Mottillo, E. P., Ramseyer, V. D., & Granneman, J. G. (2018). SERCA2b Cycles Its Way to UCP1-Independent Thermogenesis in Beige Fat. *Cell Metabolism*, *27*(1), 7–9.

https://doi.org/10.1016/j.cmet.2017.12.015

Mowers, J., Uhm, M., Reilly, S. M., Simon, J., Leto, D., Chiang, S.-H., Chang, L., & Saltiel, A. R. (2013). Inflammation produces catecholamine resistance in obesity via activation of PDE3B by the protein kinases IKKε and TBK1. *ELife*, *2*, e01119. https://doi.org/10.7554/eLife.01119

Nantel, F., Bonin, H., Emorine, L. J., Zilberfarb, V., Strosberg, A. D., Bouvier, M., & Marullo, S. (1993). The human beta 3-adrenergic receptor is resistant to short term agonist-promoted desensitization. *Molecular Pharmacology*, *43*(4), 548–555.

Palmieri, F. (2004). The mitochondrial transporter family (SLC25): physiological and pathological implications. *Pflugers Archiv : European Journal of Physiology*, *447*(5), 689–709. https://doi.org/10.1007/s00424-003-1099-7

Park, M., Reddy, G. R., Wallukat, G., Xiang, Y. K., & Steinberg, S. F. (2017). β1-adrenergic receptor O-glycosylation regulates N-terminal cleavage and signaling responses in cardiomyocytes. *Scientific Reports*, *7*(1), 1–13. https://doi.org/10.1038/s41598-017-06607-z

Peirce, V., Carobbio, S., & Vidal-Puig, A. (2014). The different shades of fat. *Nature*, *510*(7503), 76–83. https://doi.org/10.1038/nature13477

Peres Valgas da Silva, C., Hernández-Saavedra, D., White, J. D., & Stanford, K. I. (2019). Cold and Exercise: Therapeutic Tools to Activate Brown Adipose Tissue and Combat Obesity. *Biology*, *8*(1). https://doi.org/10.3390/biology8010009

Perez, C., Albert, I., DeFay, K., Zachariades, N., Gooding, L., & Kriegler, M. (1990). A nonsecretable cell surface mutant of tumor necrosis factor (TNF) kills by cell-to-cell contact. *Cell*, *63*(2), 251–258. https://doi.org/10.1016/0092-8674(90)90158-B

Prentki, M., & Madiraju, S. R. M. (2008). Glycerolipid metabolism and signaling in health and disease. *Endocrine Reviews*, *29*(6), 647–676. https://doi.org/10.1210/er.2008-0007

Prenzel, N., Zwick, E., Daub, H., Leserer, M., Abraham, R., Wallasch, C., & Ullrich, A. (1999). EGF receptor transactivation by G-protein-coupled receptors requires metalloproteinase cleavage of proHB-EGF. *Nature*, *402*(6764), 884–888. https://doi.org/10.1038/47260

Prins, M. L. (2008). Cerebral metabolic adaptation and ketone metabolism after brain injury. *Journal of Cerebral Blood Flow and Metabolism*, *28*(1), 1–16. https://doi.org/10.1038/sj.jcbfm.9600543

Rahbani, J. F., Bunk, J., Lagarde, D., Samborska, B., Roesler, A., Xiao, H., Shaw, A., Kaiser, Z., Braun, J. L., Geromella, M. S., Fajardo, V. A., Koza, R. A., & Kazak, L. (2024). Parallel control of cold-triggered adipocyte thermogenesis by UCP1 and CKB. *Cell Metabolism*. https://doi.org/10.1016/j.cmet.2024.01.001

Reddy, P., Slack, J. L., Davis, R., Cerretti, D. P., Kozlosky, C. J., Blanton, R. A., Shows, D., Peschon, J. J., & Black, R. A. (2000). Functional analysis of the domain structure of tumor necrosis factor-α converting enzyme. *Journal of Biological Chemistry*, *275*(19), 14608–14614. https://doi.org/10.1074/jbc.275.19.14608

Reshef, L., Olswang, Y., Cassuto, H., Blum, B., Croniger, C. M., Kalhan, S. C., Tilghman, S. M., & Hanson, R. W. (2003). Glyceroneogenesis and the triglyceride/fatty acid cycle. *The Journal of Biological Chemistry*, *278*(33), 30413–30416. https://doi.org/10.1074/jbc.R300017200

Rosenwald, M., & Wolfrum, C. (2014). The origin and definition of brite versus white and classical brown adipocytes. *Adipocyte*, *3*(1), 4–9. https://doi.org/10.4161/adip.26232

Sárvári, A. K., Van Hauwaert, E. L., Markussen, L. K., Gammelmark, E., Marcher, A.-B., Ebbesen, M. F., Nielsen, R., Brewer, J. R., Madsen, J. G. S., & Mandrup, S. (2021). Plasticity of Epididymal Adipose Tissue in Response to Diet-Induced Obesity at Single-Nucleus Resolution. *Cell Metabolism*, *33*(2), 437-453.e5. https://doi.org/10.1016/j.cmet.2020.12.004

Scharfenberg, F., Helbig, A., Sammel, M., Benzel, J., Schlomann, U., Peters, F., Wichert, R., Bettendorff, M., Schmidt-Arras, D., Rose-John, S., Moali, C., Lichtenthaler, S. F., Pietrzik, C. U., Bartsch, J. W., Tholey, A., & Becker-Pauly, C. (2020). Degradome of soluble ADAM10

and ADAM17 metalloproteases. *Cellular and Molecular Life Sciences*, *77*(2), 331–350. https://doi.org/10.1007/s00018-019-03184-4

Schena, G., & Caplan, M. J. (2019). Everything You Always Wanted to Know about β(3)-AR * (* But Were Afraid to Ask). *Cells*, *8*(4). https://doi.org/10.3390/cells8040357

Schirinzi, V., Poli, C., Berteotti, C., & Leone, A. (2023). Browning of Adipocytes: A Potential Therapeutic Approach to Obesity. *Nutrients*, *15*(9). https://doi.org/10.3390/nu15092229

Seals, D. F., & Courtneidge, S. A. (2003). The ADAMs family of metalloproteases: Multidomain proteins with multiple functions. *Genes and Development*, *17*(1), 7–30. https://doi.org/10.1101/gad.1039703

Shi, Z., Xu, W., Loechel, F., Wewer, U. M., & Murphy, L. J. (2000). ADAM 12, a disintegrin metalloprotease, interacts with insulin-like growth factor-binding protein-3. *The Journal of Biological Chemistry*, *275*(24), 18574–18580. https://doi.org/10.1074/jbc.M002172200

Sistare, F. D., & Haynes, R. C. (1985). Acute stimulation by glucocorticoids of gluconeogenesis from lactate/pyruvate in isolated hepatocytes from normal and adrenalectomized rats. *Journal of Biological Chemistry*, *260*(23), 12754–12760. https://doi.org/10.1016/s0021-9258(17)38941-x

Smith, D. L. J., Yang, Y., Hu, H. H., Zhai, G., & Nagy, T. R. (2013). Measurement of interscapular brown adipose tissue of mice in differentially housed temperatures by chemical-shift-encoded water-fat MRI. *Journal of Magnetic Resonance Imaging : JMRI*, *38*(6), 1425–1433. https://doi.org/10.1002/jmri.24138

Straat, M. E., Hoekx, C. A., van Velden, F. H. P., Pereira Arias-Bouda, L. M., Dumont, L., Blondin, D. P., Boon, M. R., Martinez-Tellez, B., & Rensen, P. C. N. (2023). Stimulation of the beta-2-adrenergic receptor with salbutamol activates human brown adipose tissue. *Cell Reports. Medicine*, *4*(2), 100942. https://doi.org/10.1016/j.xcrm.2023.100942

Sun, W., Dong, H., Balaz, M., Slyper, M., Drokhlyansky, E., Colleluori, G., Giordano, A., Kovanicova, Z., Stefanicka, P., Balazova, L., Ding, L., Husted, A. S., Rudofsky, G., Ukropec, J., Cinti, S., Schwartz, T. W., Regev, A., & Wolfrum, C. (2020). snRNA-seq reveals a subpopulation of adipocytes that regulates thermogenesis. *Nature*, *587*(7832), 98–102. https://doi.org/10.1038/s41586-020-2856-x

Susulic, V. S., Frederich, R. C., Lawitts, J., Tozzo, E., Kahn, B. B., Harper, M. E., Himms-Hagen, J., Flier, J. S., & Lowell, B. B. (1995). Targeted disruption of the beta 3-adrenergic receptor gene. *The Journal of Biological Chemistry*, *270*(49), 29483–29492. https://doi.org/10.1074/jbc.270.49.29483

Tchivileva, I. E., Tan, K. S., Gambarian, M., Nackley, A. G., Medvedev, A. V, Romanov, S., Flood, P. M., Maixner, W., Makarov, S. S., & Diatchenko, L. (2009). Signaling pathways mediating beta3-adrenergic receptor-induced production of interleukin-6 in adipocytes. *Molecular Immunology*, *46*(11–12), 2256–2266. https://doi.org/10.1016/j.molimm.2009.04.008

Townsend, K. L., & Tseng, Y.-H. (2014). Brown fat fuel utilization and thermogenesis. *Trends in Endocrinology and Metabolism: TEM*, *25*(4), 168–177. https://doi.org/10.1016/j.tem.2013.12.004

Valentine, J. M., Ahmadian, M., Keinan, O., Abu-Odeh, M., Zhao, P., Zhou, X., Keller, M. P., Gao, H., Yu, R. T., Liddle, C., Downes, M., Zhang, J., Lusis, A. J., Attie, A. D., Evans, R. M., Rydén, M., & Saltiel, A. R. (2022). β3-Adrenergic receptor downregulation leads to adipocyte catecholamine resistance in obesity. *The Journal of Clinical Investigation*, *132*(2). https://doi.org/10.1172/JCI153357

Wang, Q. A., & Scherer, P. E. (2014). The AdipoChaser mouse: A model tracking adipogenesis in vivo. *Adipocyte*, *3*(2), 146–150. https://doi.org/10.4161/adip.27656

Wolfe, R. R., Klein, S., Carraro, F., & Weber, J. M. (1990). Role of triglyceride-fatty acid cycle in controlling fat metabolism in humans during and after exercise. *The American Journal of Physiology*, *258*(2 Pt 1), E382-9. https://doi.org/10.1152/ajpendo.1990.258.2.E382

Zettl, M., Adrain, C., Strisovsky, K., Lastun, V., & Freeman, M. (2011). Rhomboid Family Pseudoproteases Use the ER Quality Control Machinery to Regulate Intercellular Signaling.

Cell, *145*(1), 79–91. https://doi.org/10.1016/j.cell.2011.02.047

Zhu, J., & Steinberg, S. F. (2021). β1-adrenergic receptor N-terminal cleavage by ADAM17; the mechanism for redox-dependent downregulation of cardiomyocyte β1-adrenergic receptors. *Journal of Molecular and Cellular Cardiology*, *154*, 70–79. https://doi.org/10.1016/j.yjmcc.2021.01.012

Ziqubu, K., Dludla, P. V, Mthembu, S. X. H., Nkambule, B. B., Mabhida, S. E., Jack, B. U., Nyambuya, T. M., & Mazibuko-Mbeje, S. E. (2023). An insight into brown/beige adipose tissue whitening, a metabolic complication of obesity with the multifactorial origin. *Frontiers in Endocrinology*, *14*, 1114767. https://doi.org/10.3389/fendo.2023.1114767

.

Acknowledgements

In the next few pages, I would like to acknowledge and express appreciation to all the people who supported me during my studies, because without their support and help, this work would never have been completed.

Firstly, I would like to thank my PhD supervisor, Dr. Anastasia Georgiadi. Dear Anastasia, over the past years I have learnt a lot from you. You are a dedicated and hardworking scientist and am glad to have paired with you during my PhD interview and for your great supervisorship. Your passion for science is truly inspiring and thank you for all the suggestions, criticism and above all for being always there for me when I needed guidance and help with experiments. You have really inspired me to try harder and grow as a young scientist. Thank you for this great opportunity to do my PhD with you. I will try and implement all the good things I have learnt from you in my career moving forward. Again, thank you for taking your time to read and review my PhD dissertation amidst your busy schedules.

I would also like to thank my other supervisor, Prof. Hoffmann. Dear Susanna, thank you for your support throughout my PhD. Already at my interview, you asked some insightful questions about my MSc project, and I was delighted when you accepted to be part of my TAC members. Looking for apartment in my first years at Munich was very challenging but thank you for the consistent apartment recommendations, I received from you through your secretary, I am forever grateful for your thoughtfulness. Again, thank you for your valuable contribution to my PhD training. We may not have worked closely in the lab, but I felt and still feel your support for me. Thank you for being a great doctor mother. Your doors were always open when I needed help with everything including immigration and visa issues. Thank you very much for inspiring me to be a great scientist and someone willing to help others I work with now and the future. Finally thank you for your great suggestions and recommendation and taking your time to read and review my PhD dissertation amidst your busy schedules.

Dear Prof. Carolin, thank you for great suggestions and input always during our several TAC meetings. Your constant recommendations and suggestions from immunological point of view during my PhD meetings with you and other TAC members has greatly impacted my career path and forever grateful.

Dear Prof. Hubbard, I remember our first meeting in Canada, though briefly, I was excited to have you as part of my TAC committee members. Thank you for all the great ideas and discussions during my several TAC meetings. Considering the time difference between Germany and Canada, you always made tremendous sacrifice to be present at the meetings. Thank you very much.

Next, special thanks go to all members of the ENP group. Dear Rabih, I feel so lucky and grateful to have you part of my PhD experience. I could not have asked for a better lab colleague. I knew I could depend on you and that gave me confidence. You were always there for me, willing to help in the lab or just have a chat, even outside lab. Thank you for your help with the numerous mouse experiments. I know that great things lie ahead of you, and I wish you so much strength and luck.

Dear Sissy, though we met at the last stage of my PhD, I felt like I had known you forever. You were very supportive, and I am grateful to have met and worked with you. Our chats in the lab and briefly on train were very meaningful and you made me laugh a lot. I wish you all the best with you PhD training, and let’s meet often.

Dear Vasiliki, I am truly grateful for your help analysing countless sequencing data for my PhD work, but also for being such a good lab colleague. Though our meeting was briefly, it was also fun working with you. I wish you a bright future and best wishes in your PhD training.

Dear Ankush, you joined our group at the end of my PhD studies. You were enthusiastic, fun and it was nice working with you. Thank you for being a great lab colleague. I wish you the best in your PhD studies and in your future endeavours.

Also, I would like to thank all the master students who have contributed to this PhD working. Dear Lun, Sarah, and Deepika. I really learnt a lot working with you ladies. I was challenged scientifically and learnt to stay focus. I know it was hard at the beginning for you guys, but I like your resilience and ability to learn faster and for the support.

To my IPEK group and new colleagues, I am grateful to be part of this group. Especially I would like to thank Dr. Dorothee Azler and Prof. Donato Santovito for giving me so much support and time to finish my PhD thesis writeup and for creating such a sound and supportive working environments. I am also, grateful to all the other members of the lab Cecilia, Irem, Venetia, Sigrid, Yuting, Yonara, Mahadia, James, Floriana, Elizabeth, and Vasiliki. It has been fun working with you guys for the last few months. I am forever grateful for your constant support and help. I could not have better colleagues and mentors for my postdoc. I know we will have so much fun doing science and working together in the future and am already excited about that. I am truly grateful and thankful.

To my husband Michael Kobina Otabil. Sweetheart, we made it. Thank you for being always by my side and for inspiring me to start my PhD studies. You always put my needs before yours and have cheered me on during stressful days, and all the times I felt like giving up on my PhD studies. I feel stronger having you by my side. You always inspired me to work hard and become a better version of myself and you always supported my dreams. I really appreciate you for creating a safe and peaceful home for us that, I can always rejuvenize after stressful moments. I cannot imagine having gone through my PhD studies without you by my side. My love God bless you and Medaase paa.

Finally, I would like to thank my parents Francis Anane Karikari and Ellen Anane Karikari and all my siblings for sacrificing so much just to see me happy and grow my career. Especially to my parents for being my immune boosters during all the difficult moments in my PhD studies. I felt so stronger, I knew I always had a place to run to. Nyame nhyira mo.

Affidavit

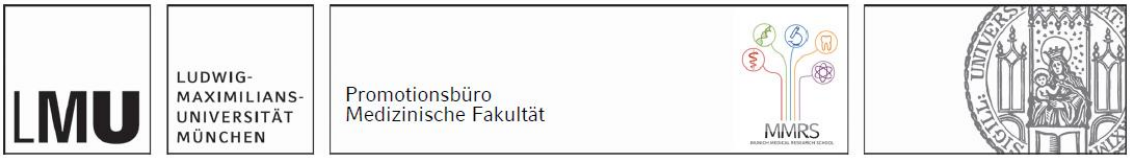

Affidavit

Karikari, Rhoda Anane

Surname, first name

Street

Zip code, town, country

I hereby declare that the submitted thesis entitled:

Investigating the role of adipocyte expressed A disintegrin and metalloprotease 17 (ADAM17) in energy expenditure and metabolic health.

……

is my own work. I have only used the sources indicated and have not made unauthorised use of services of a third party. Where the work of others has been quoted or reproduced, the source is always given.

I further declare that the dissertation presented here has not been submitted in the same or similar form to any other institution for the purpose of obtaining an academic degree.

Olching, 12.03.2025

place, date

Rhoda Anane Karikari

Signature doctoral candidate